

# Biomedical Imaging: Role and Opportunities of Medical Imaging in the “Omics” Era

Guest Editors: Tzu-Chen Yen, Dimitris Visvikis, Tinsu Pan, and Yu-Hua Dean Fang



---



# **Biomedical Imaging: Role and Opportunities of Medical Imaging in the “Omics” Era**

## **Biomedical Imaging: Role and Opportunities of Medical Imaging in the “Omics” Era**

Guest Editors: Tzu-Chen Yen, Dimitris Visvikis, Tinsu Pan,  
and Yu-Hua Dean Fang



Copyright © 2014 Hindawi Publishing Corporation. All rights reserved.

This is a special issue published in "BioMed Research International." All articles are open access articles distributed under the Creative Commons Attribution License, which permits unrestricted use, distribution, and reproduction in any medium, provided the original work is properly cited.

## Contents

---

**Biomedical Imaging: Role and Opportunities of Medical Imaging in the “Omics” Era,**  
Tzu-Chen Yen, Dimitris Visvikis, Tinsu Pan, and Yu-Hua Dean Fang  
Volume 2014, Article ID 930213, 2 pages

**Advances in Miniaturized Instruments for Genomics,** Cihun-Siyong Alex Gong and Kin Fong Lei  
Volume 2014, Article ID 734675, 13 pages

**The Role of Imaging in Radiation Therapy Planning: Past, Present, and Future,** Gisele C. Pereira,  
Melanie Traughber, and Raymond F. Muzic Jr.  
Volume 2014, Article ID 231090, 9 pages

**Development and Evaluation of an Open-Source Software Package “CGITA” for Quantifying Tumor Heterogeneity with Molecular Images,** Yu-Hua Dean Fang, Chien-Yu Lin, Meng-Jung Shih,  
Hung-Ming Wang, Tsung-Ying Ho, Chun-Ta Liao, and Tzu-Chen Yen  
Volume 2014, Article ID 248505, 9 pages

**Pushing CT and MR Imaging to the Molecular Level for Studying the “Omics”: Current Challenges and Advancements,** Hsuan-Ming Huang and Yi-Yu Shih  
Volume 2014, Article ID 365812, 17 pages

**Current Opportunities and Challenges of Magnetic Resonance Spectroscopy, Positron Emission Tomography, and Mass Spectrometry Imaging for Mapping Cancer Metabolism *In Vivo*,**  
Gigin Lin and Yuen-Li Chung  
Volume 2014, Article ID 625095, 13 pages

## Editorial

# Biomedical Imaging: Role and Opportunities of Medical Imaging in the “Omics” Era

Tzu-Chen Yen,<sup>1,2</sup> Dimitris Visvikis,<sup>3</sup> Tinsu Pan,<sup>4</sup> and Yu-Hua Dean Fang<sup>5</sup>

<sup>1</sup> Center for Advanced Molecular Imaging and Translation, Chang Gung Memorial Hospital, Linkou 333, Taiwan

<sup>2</sup> Department of Nuclear Medicine, Chang Gung Memorial Hospital, No. 5, Fu-Hsin Street, Kweishan, Linkou, Taoyuan 333, Taiwan

<sup>3</sup> INSERM, UMR1101 LaTIM, CHRU Brest, 29609 Brest, France

<sup>4</sup> Division of Diagnostic Imaging, Department of Imaging Physics, The University of Texas MD Anderson Cancer Center, Houston, TX 77030, USA

<sup>5</sup> Department of Electrical Engineering, Chang Gung University, Taoyuan 333, Taiwan

Correspondence should be addressed to Tzu-Chen Yen; [yentc1110@gmail.com](mailto:yentc1110@gmail.com)

Received 5 May 2014; Accepted 5 May 2014; Published 4 June 2014

Copyright © 2014 Tzu-Chen Yen et al. This is an open access article distributed under the Creative Commons Attribution License, which permits unrestricted use, distribution, and reproduction in any medium, provided the original work is properly cited.

In recent decades, we have witnessed an explosive growth of diagnostic tools that have changed the face of modern medicine. Among these diagnostic tools, medical imaging is indeed one of the most representative fields that have been growing fast, used extensively, and regarded as an irreplaceable part of clinical routines. With a very different scale, “omics” refers to the study of cellular- or DNA-level molecules including their functions, structures, interactions, and involvement in disease development. Similar to imaging, the “omics” fields such as genomics, proteomics, and metabolomics have also advanced drastically in recent decades. The “omics” data obtained from a patient reveal a much more microscaled world that allows the practitioner to see what is going on in the genomic and proteomic levels. As imaging and omics technologies look at human physiology in quite different scales, physicians and scientists are currently attempting to integrate imaging and omics data for tailored therapies and research purposes. This special issue provides original research and review on the potential role and value of imaging in the context of personalized medicine based on omics information.

Imaging can be used as a tool to directly measure the omics data. As pointed out by the comprehensive review by G. Lin and Y. L. Chung on the use of molecular imaging methods to study metabolomics in this issue, recent technological advancements of parallel imaging and high-field magnets have largely propelled the advancement of metabolomics for

MR spectroscopy to measure the amount and exchange of multiple metabolites. Such imaging technologies can also be applied to *in vivo* imaging for both small animals and humans. Imaging the living organisms allows investigators to observe the metabolism and molecular exchange in both the spatial and temporal domains. In addition to measuring the omics data with imaging, clinical oncology continues to use medical images for treatment planning. G. C. Pereira et al. have given a comprehensive review on the role and importance of imaging in radiation therapies in this special issue. In this review, the critical role of imaging in radiation therapy is reviewed for the application of dose calculation, lesion location, and delineation. The combination of omics information and the image-derived lesion information has a high potential to further enhance the treatment efficacy for oncological applications.

Image quantification and information extraction remain to be a challenge for integrating imaging and omics information. In this special issue, Y.-H. D. Fang et al. described an example in the open-source software development for quantifying the intratumoral heterogeneity. Such quantification based on texture analysis has been reported to be helpful for prognosis in oncological applications. However, currently there is no free software for such quantification in the public domain. Therefore, Y.-H. D. Fang et al. developed and shared a software package to fill this void and demonstrated its usefulness in a small cohort of oral cavity cancer patients.

There are also many practical limitations for medical imaging that is modality-dependent. Ionizing radiation is one major concern for CT and radionuclide imaging such as PET and SPECT. MR does not require ionizing radiation and owns a great potential in molecular imaging, but it has its own limitations in speed, cost, and potential renal toxicity with the use of Gd-based contrast agents. In this special issue, H. M. Huang and Y. Y. Shih gave a review on the recent technical advancement of dose reduction for CT and acceleration for MR. From their review, it could be optimistically expected that such practical limitations will gradually be resolved to make those two modalities more commonly used in the integration of imaging and omics research in the future.

To fully exploit the omics data in personalized medicine, new advancements for instrumentation to extract omics data play a critical role. A review article by C.-S. A. Gong and K. F. Lei in this special issue will discuss the recent advancement of miniaturized devices for genomics, which may further advance the clinical popularity for gene sequencing. One of the striking examples is the use of electrochemical impedance spectroscopy as the electrical detection of DNA hybridization in microfluidic devices. The combination of microfluidic and impedimetric technologies shows an alternative and attractive method for detecting the genomic signal.

In conclusion, the dramatic advancements of the omics knowledge have further propelled the development of personalized medicine. The original and review articles in this special issue show that there will be a significant role of medical images in the future of personalized medicine. It can be optimistically expected that imaging will continue to evolve as part of the omics data as well as serving as a tool for omics measurements. Although integration of imaging and omics data is a challenging task for the imaging community, such efforts will truly benefit personalized medicine by allowing us to see an individual from macro- to microscale levels.

*Tzu-Chen Yen  
Dimitris Visvikis  
Tinsu Pan  
Yu-Hua Dean Fang*

## Review Article

# Advances in Miniaturized Instruments for Genomics

Cihun-Siyong Alex Gong<sup>1</sup> and Kin Fong Lei<sup>2,3</sup>

<sup>1</sup> Department of Electrical Engineering, School of Electrical and Computer Engineering, College of Engineering, Chang Gung University, Taoyuan 333, Taiwan

<sup>2</sup> Portable Energy System Group, Green Technology Research Center, College of Engineering, Chang Gung University, Taoyuan 333, Taiwan

<sup>3</sup> Department of Mechanical Engineering, Chang Gung University, Taoyuan, Taiwan

Correspondence should be addressed to Kin Fong Lei; kflei@mail.cgu.edu.tw

Received 18 December 2013; Revised 21 January 2014; Accepted 30 January 2014; Published 29 May 2014

Academic Editor: Tzu-Chen Yen

Copyright © 2014 C.-S. A. Gong and K. F. Lei. This is an open access article distributed under the Creative Commons Attribution License, which permits unrestricted use, distribution, and reproduction in any medium, provided the original work is properly cited.

In recent years, a lot of demonstrations of the miniaturized instruments were reported for genomic applications. They provided the advantages of miniaturization, automation, sensitivity, and specificity for the development of point-of-care diagnostics. The aim of this paper is to report on recent developments on miniaturized instruments for genomic applications. Based on the mature development of microfabrication, microfluidic systems have been demonstrated for various genomic detections. Since one of the objectives of miniaturized instruments is for the development of point-of-care device, impedimetric detection is found to be a promising technique for this purpose. An in-depth discussion of the impedimetric circuits and systems will be included to provide total consideration of the miniaturized instruments and their potential application towards real-time portable imaging in the “-omics” era. The current excellent demonstrations suggest a solid foundation for the development of practical and widespread point-of-care genomic diagnostic devices.

## 1. Introduction

Genomics has become an important part of our life since its name was established in the latter half of the twentieth century. It was derived from genetics which includes “classic” and “molecular” as a whole. Polymer chain reaction (PCR) technique is a gold standard for clinical genomic diagnosis. Normally, the concentration of genomic sample is too low for generating detectable signal. PCR can amplify a few copies of DNA to millions of copies of a particular DNA sequence. The technique relies on thermal cycling, that is, repeated heating and cooling of the reaction, for DNA melting and enzymatic replication of the DNA. Generally, twenty to forty thermal cycle times are involved and they take several hours to complete. Although this technique is sensitive for genomic detection, it is time consuming and labor intensive, limiting the throughput of the diagnosis.

In order to enhance the efficiency of the biological reaction, reduce the usage of reagent and sample, and eliminate the fault by human handling, miniaturized instruments that

handle small quantity of fluid, for example, microliter or nanoliter, were proposed for the next generation of the diagnostic equipment. Such instruments are also named as microfluidic systems, lab-on-chip (LOC) devices, biochips, or micrototal-analysis systems ( $\mu$ TAS). Because fluid in small amount is manipulated in microscale environment, one of the important properties is to highly enhance the surface-to-volume ratio of the fluid. For some specific applications, high surface-to-volume ratio can benefit the process efficiency. For example, DNA hybridization in rapid diagnostic device normally involves a solid support for the immobilization of the reactants, that is, probe DNA strands. The counterpart of the reactant, that is, target DNA strands, is introduced to the site for binding reaction. The binding efficiency is based on the collision possibility. Because of the reduction in diffusion distance and increase in surface-to-volume ratio in microfluidic environment, the reaction kinetics of DNA strands binding reaction was shown significantly accelerated compared with the conventional microplate technique [1–5]. That results in greatly improving the response time of

the biological reaction and the sensitivity of the biological detection. Microfluidic system is often interpreted to a miniaturized version of bioanalytical laboratory. It can perform the entire analytical protocol, such as sample preparation, reagent application, biological reaction, and detection automatically to eliminate the handling fault. Since microfluidic system is a miniaturized instrument, portability is realizable for the point-of-care diagnostic applications.

The aim of this paper is to report on recent developments on miniaturized instruments for genomic applications. An overview of microfluidic systems and their demonstrations for genomic diagnosis will be discussed. Moreover, impedimetric detection is found to be a promising technique for point-of-care genomic detection because the impedimetric signal can easily be analyzed by miniaturized electrical circuits. In-depth discussion of the consideration and review of impedimetric circuits and systems will also be included in this article.

## **2. Miniaturized Instruments: Microfluidic Systems**

In the past decade, development of the microfluidic technology becomes intensive and many research articles are available [6–11]. The fabrication of microfluidic systems was originally based on the silicon fabrication technology from semiconductor and microelectromechanical systems (MEMS). Silicon microfabrication is well established but silicon material is not optically transparent and is electrically conductive. Hence, it is not appropriate for the biomedical applications. For example, the microfluidic system for cell culture is required to be transparent for continuous optical monitoring of cell morphology. Moreover, microfluidic system for glucose detection is based on electrochemical reaction which needs insulated substrate for measurement. Therefore, silicon may not be an appropriate material when optical and electrochemical detections are adopted in the microfluidic systems. Therefore, glass and polymeric materials were used because they are less expensive, optically transparent, and not electrically conductive. Specific fabrication technologies for microfluidic systems were introduced, such as soft lithography, hot embossing, and substrate bonding techniques. Soft lithography represents a nonphotolithographic strategy based on self-assembly and replica molding for carrying out micro- and nanofabrication [12]. An elastomeric stamp with patterned relief structures on its surface is used to generate patterns and structures with feature sizes ranging from 30 nm to 100  $\mu\text{m}$ . It provides a convenient, effective, and low-cost method for the formation and manufacturing of micro- and nanostructures. Hot embossing technique is for mass production of plastic micro-components [13]. A mold with microstructures is pressed into a thermoplastic polymer film heated beyond its glass transition temperature under vacuum. After cooling down, the microstructures can be transferred from the mold to the polymer film. To fabricate a functional microfluidic system, substrate bonding is an important process and adhesion between substrates is a problem of great practical concern.

Thermal compression, ultrasonic, or gluing by application of either epoxy or methanol may induce global and localized geometric deformation of the substrates or leave an interfacial layer with significant thickness variation. Therefore, special bonding processes for glass and polymeric materials have been developed for fabricating microfluidic systems [14–17]. Localized welding of polymeric materials embedded metal films located between the desired bond surfaces by microwave energy has been developed [15]. The bonding can be achieved with 10 W microwave power in 120 s.

Based on the mature development of the fabrication technology, a broad spectrum of biological analytical applications has been demonstrated using microfluidic systems, such as DNA analysis [1, 18–24], immunoassay [25–31], and cell analysis [32–38]. For example, immunoassay on compact disc (CD) has been demonstrated and fluids in CD were manipulated by the centrifugal forces controlled by the rotational speed of the CD [30]. Illustration and photograph of the CD-based microfluidic system are shown in Figure 1. High throughput screening of analytes could be realized by simultaneous functions in parallel layouts on the CD. Enzyme-linked immunosorbent assay (ELISA) was demonstrated on this CD-based platform. Another example is to construct a microfluidic chip for real-time and noninvasive impedimetric monitoring of cell proliferation and chemosensitivity in three-dimensional (3D) cell culture construct, as shown in Figure 2 [37]. Human oral cancer cells (OEC-M1) were encapsulated in 3D agarose scaffold and cultured in a miniaturized chamber under perfusion of tested substance. This setting provides a more *in vitro* physiologically relevant microenvironment to better mimic the complex *in vivo* microenvironment. These excellent developments showed the capability of microfluidic system for performing complex analytical applications. Commercial possibility is obvious because the microfluidic system can provide a total solution of biological analysis from the sample application to the display of the analysis results. Point-of-care diagnostic applications can be realized based on the advantages of miniaturization, integration, and automation of the microfluidic system.

## **3. Integrated Microfluidic Genomic Systems**

Microfluidic systems have been also applied to the genomic applications. System integrated with microchannels, heaters, temperature sensors, and fluorescence detectors was fabricated for the functions of capturing DNA, mixing solutions, amplifying DNA, and separating and detecting of those products [20]. These complicated operations could be performed on a single glass and silicon substrate. Strand displacement amplification experiment was conducted and showed that the specific target DNA was successfully amplified and detected. Moreover, PCR is a widely used technique in biological applications and was implemented on a microfluidic system, as illustrated in Figure 3 [39]. The PCR was achieved by introducing the reactant droplet into the inlet. Three reaction chambers, respectively, stabled at 90°C, 72°C, and 55°C were

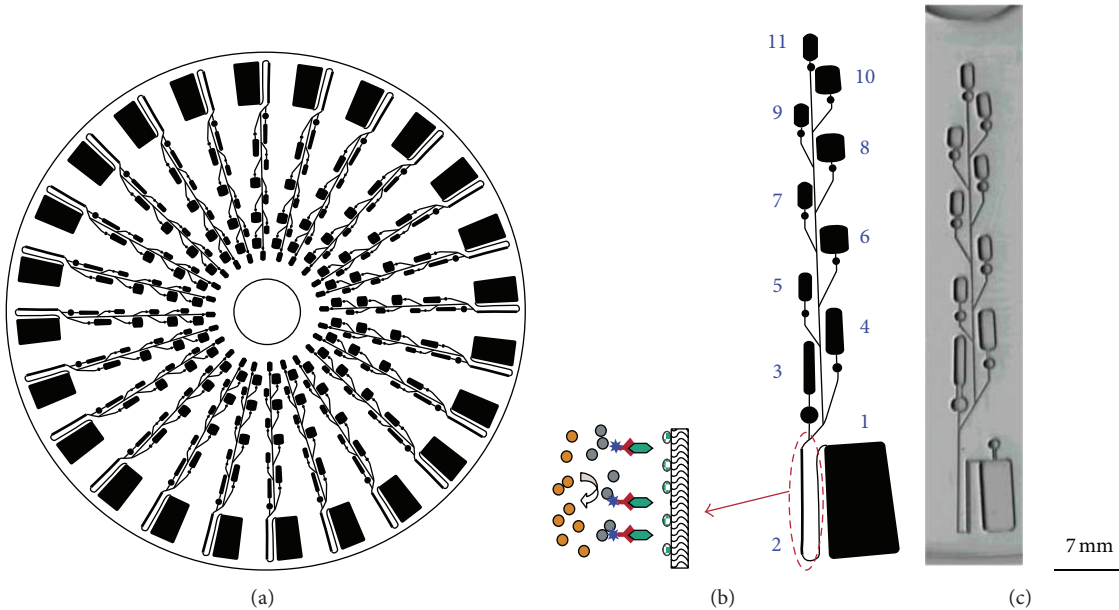


FIGURE 1: Schematics of (a) a CD-ELISA design with 24 sets of assays, (b) a single assay, and (c) photo of a single assay. Copyright 2004. Reprinted from [30] with permission from the American Chemistry Society.

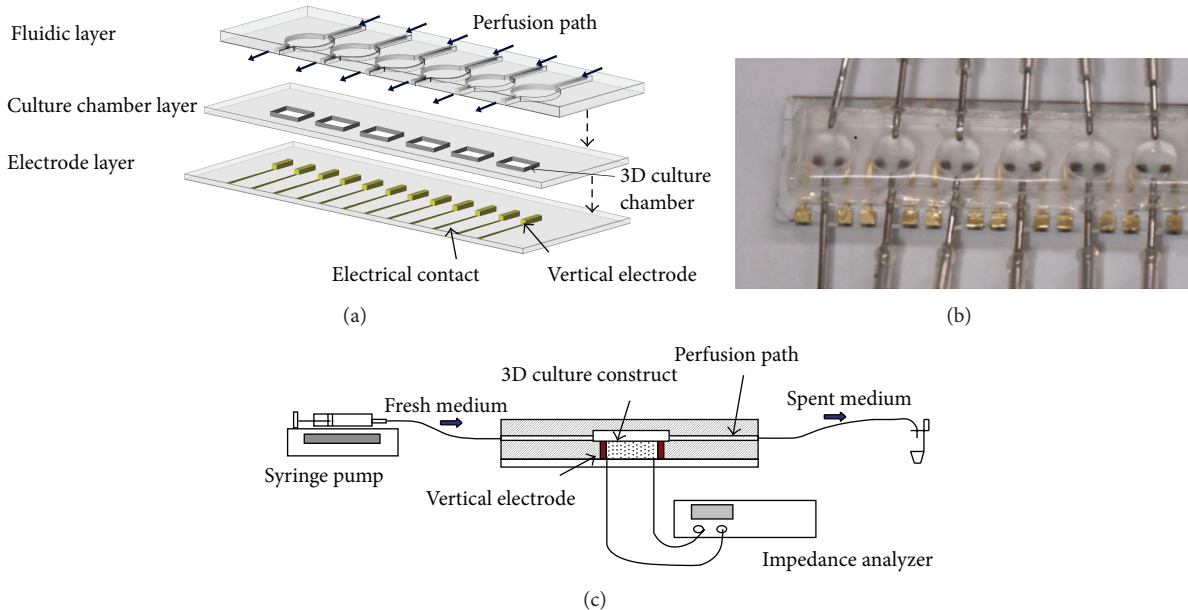


FIGURE 2: (a) Design of the microfluidic chip. (b) Photograph of the microfluidic chip. (c) Illustration of the experimental setup of the perfusion 3D cell culture incorporated with on-site impedance measurement. Copyright 2014. Reprinted from [37] with permission from the Elsevier.

integrated in a chip and droplet was driven back and forth by three piezoelectric micropumps between these three reaction chambers. After 20–30 thermal cycles, the PCR products were pumped into the reservoir to be collected and analyzed by gel electrophoresis. Also, an electrokinetically controlled DNA hybridization microfluidic chip has been demonstrated and can perform all processes from sample dispensing to hybridization detection within 5 minutes [1]. The chip consisted of a PDMS upper substrate and a lower glass substrate

that served as a substrate for the hybridization array, as shown in Figure 4. The design of the chip was an H-type channel structure containing immobilized single-stranded oligonucleotide probes. The electroosmotic pumping could dispense the controlled samples of nanoliter volume directly to the hybridization array and remove nonspecific adsorption. Hybridization, washing, and scanning procedures can be conducted simultaneously. Detection levels as low as 50 pM were recorded using an epifluorescence microscope.

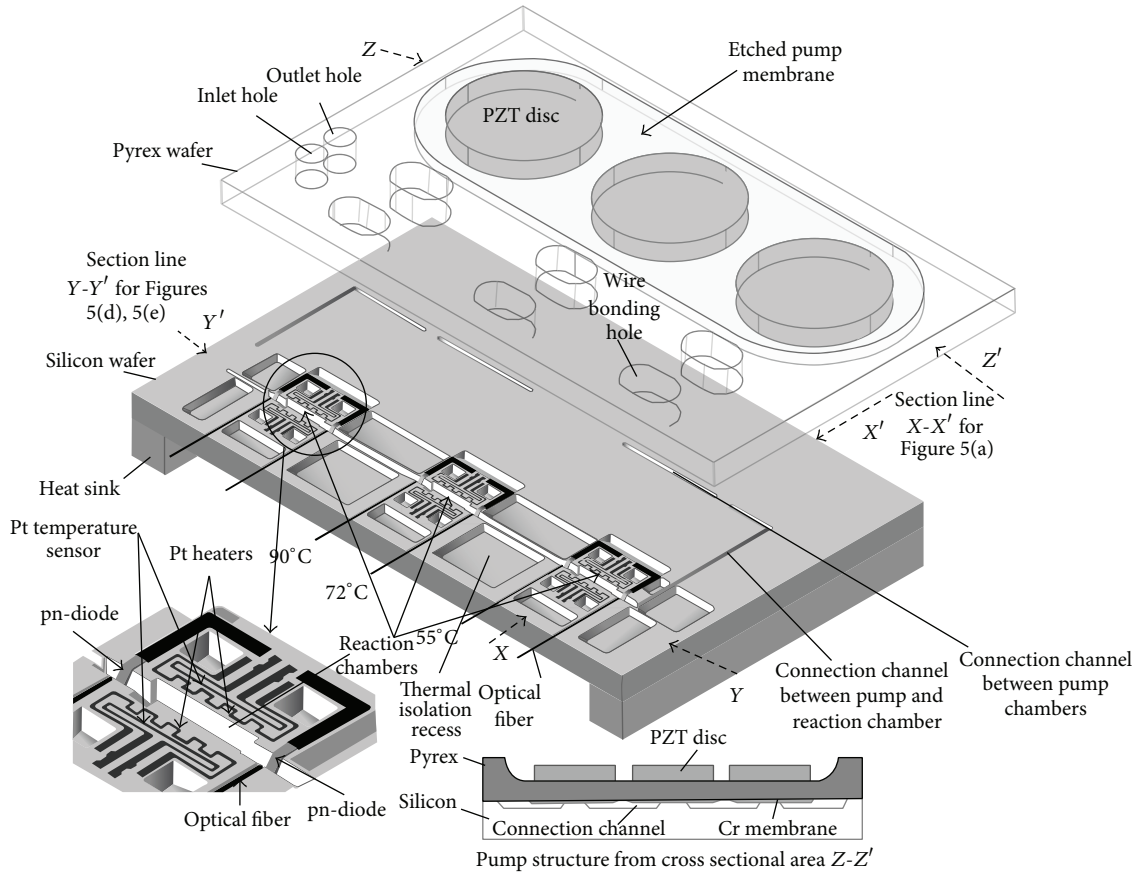


FIGURE 3: Schematic of the pump PCR chip. For simplification, the upper glass wafer and the lower silicon wafer are illustrated apart, although in the actual device both wafers are connected by anodic bonding. The lower left insert figure shows an expanded view of the reaction chamber and the lower right insert shows the cross-section of the micropump. Copyright 2003. Reprinted from [39] with permission from IOP Publishing Ltd.

#### 4. Impedimetric Detection of Genomic Signal

In conventional genomic detection, optical measurement, for example, fluorescent labeling technique, was utilized to quantify the genomic activity, for example, DNA hybridization and PCR product. But this measurement technique is time consuming and labor intensive. Alternatively, impedimetric detection was proposed to be one of the promising techniques to quantify biological activity in the microfluidic systems. The detection results are represented by electrical signals which can easily interface with miniaturized instruments. For example, electrical detection of DNA hybridization using electrochemical impedance spectroscopy (EIS) was demonstrated [40]. Results showed a 25% increase of impedance for double-stranded DNA on gold electrode compared with the same electrode with immobilized single-stranded DNA. Another example showed that the DNA hybridization could be detected by the resistance change across the electrode [41, 42]. DNA hybridization on a pair of electrodes was indicated by gold nanoparticles and the gold nanoparticles were physically amplified to a silver conductive layer on the electrode. The hybridization result could be measured by the conductivity changes across the electrode. These demonstrated showed an alternative method for detecting

the genomic signal. For the application of cell proliferation study, the entire process requires a long period of time and in a controlled environment. It is more preferable to perform in a bench-top system. However, a miniaturized and portable device is more preferable for the on-site rapid diagnostic application. The combination of microfluidic and impedimetric technologies would be suitable for such a specific application.

#### 5. Impedimetric Foundation

As mentioned, the impedimetric method provides a versatile way that can be used for many biological applications including the quantification of genomic activity and the noninvasive monitoring of cell proliferation and chemosensitivity with a microfluidic chip. The underlying principle of the technique can be explained from Figure 5. Let us assume, for the sake of simplicity, that the sample under test (SUT) consists only of a resistor that is connected with two electrodes. The upper electrode is commonly called “anode” or “working electrode.” The lower electrode is called “auxiliary electrode” functioning as “cathode.” To understand SUT, an active alternating current (AC),  $I_S(t)$ , is generated and injected into the close loop.

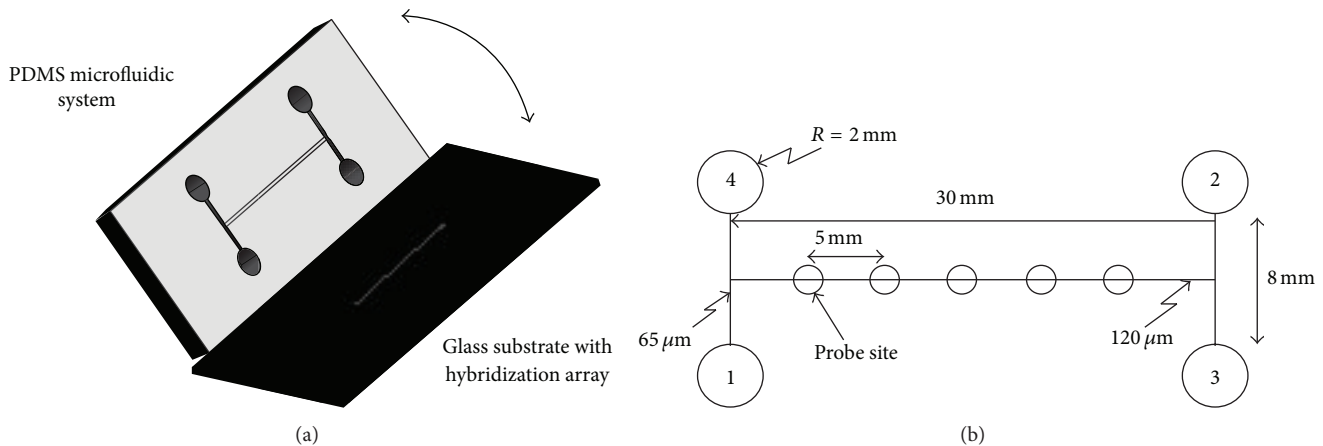


FIGURE 4: (a) Assembly procedure for PDMS fluidics and immobilized hybridization array. (b) H-type channel structure for DNA hybridization chip: (1) sample port, (2) auxiliary port, (3) buffer port, and (4) wash port. Copyright 2004. Reprinted from [1] with permission from the American Chemical Society.

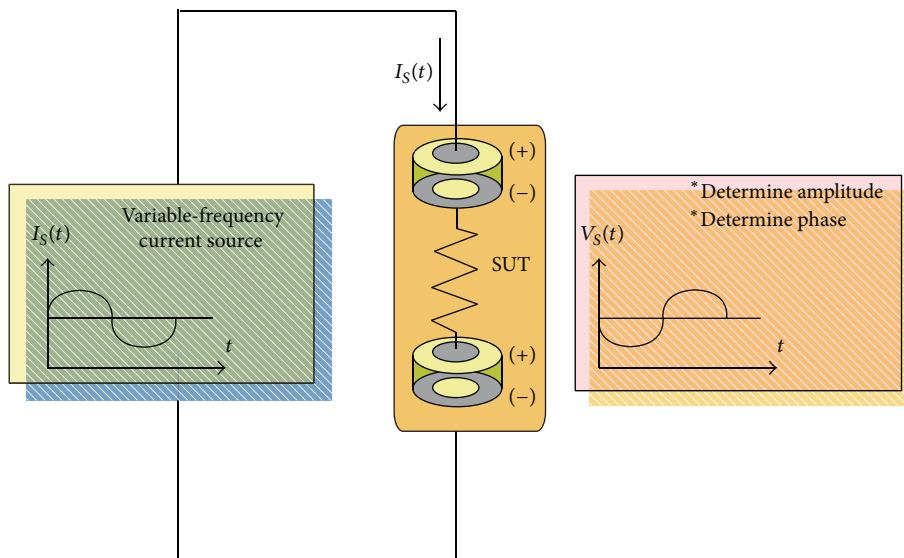


FIGURE 5: The basic model of equivalent circuit used to elaborate on the relation of sample under test (SUT) to the generated current source and resulting voltage response.

The resulting voltage drop across the two electrodes can be measured to derive the resistance of SUT by means of Ohm's law, provided that both the two electrodes have zero voltage drop. When the equivalent circuit of electrode becomes a complex number, as the combination shown in Figure 6(a), variable-frequency current source is required to draw so-called "Nyquist plot" (Figure 6(b)) [43]. The model shown in Figure 6(a) is based on electrochemical point of view. It is consisted of an ohmic resistance  $R_o$  stemming from the solution resistance and electrode geometry, a charge transfer resistance  $R_{ct}$  stemming from the charge transfer between the interface of electrode and electrolyte, an electric double-layer capacitance  $C_d$  stemming from placing a large-area charge in the electrolyte in proximity to that on the porous electrodes at the medium-frequency region, a Warburg impedance  $Z_w$  representing the mobility of the internal ions resulting from

the diffusion and migration at the low-frequency region, and an electrode inductance  $L_d$  stemming from reduction in the penetration depth of the ions at the high-frequency region, respectively [43, 44]. As a matter of fact, with regard to the ohmic resistance of SUT, an electrode immersed into an electrolyte creates a potential that is related to the oxidation-reduction concentration, according to the Nernst law [44]. The corresponding potentials cancel out as long as the two electrodes are the same. Unfortunately, this would never happen and a potential difference of a few millivolts would always exist between SUT and either of the electrodes [44].

## 6. Impedimetric Consideration

There have been several technically sound circuits and systems demonstrated in the literature to implement

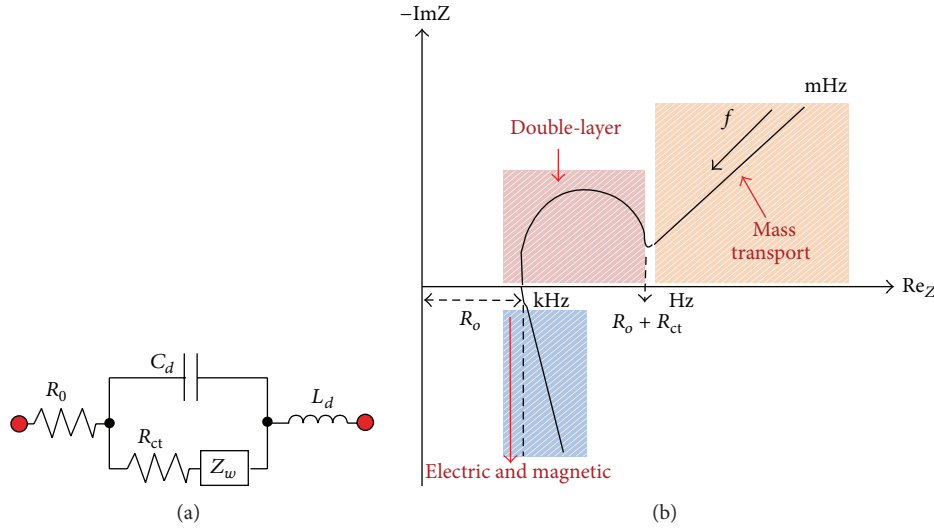


FIGURE 6: (a) Schematic of the equivalent circuit of electrode in an electrochemical point of view. (b) The so-called Nyquist plot showing the characteristic of frequency response versus the decomposition of impedance.

the impedimetric method so far [44–49]. They are similar to a coherent demodulation technique demonstrated in Figure 7, where a four-electrode method was adopted [45]. The impedance sensing method shown in Figure 5 is premised on the assumption that both working and auxiliary electrodes have resistance value of “zero.” However, as mentioned, this would never be the case and there exist voltage drops of them in the close loop as soon as an electrical current flows through, turning out that certain inversion formula is unavoidable for derivation of the ohmic resistance of SUT. This may be taxing on postprocessing and result in incapability of real-time impedance monitoring. By taking the advantages of the advances in modern semiconductor technologies, an amplifier with ultrahigh input impedance (almost open circuit) can be readily available. In addition, differential sensing is always a better choice than the single-ended counterpart as a result of better noise immunity [46, 50]. These form the foundation of the architecture shown in Figure 7.

## 7. Circuits and Systems for Bioimpedance Measurement

Referring to Figure 7, in addition to the necessary electrodes  $\text{Ze1}$  and  $\text{Ze4}$  to form a loop, two additional electrodes  $\text{Ze2}$  and  $\text{Ze3}$  were added and combined with the instrumentation amplifier (IA) whose common-mode rejection ratio (CMRR) is significantly improved as compared with the ordinary counterpart [45, 46]. The variable-frequency sinusoidal current used for sensing was generated by a dedicated voltage-controlled oscillator (VCO). Thanks to the high-impedance feature of the amplifier, there was no current flowing through  $\text{Ze2}$  and  $\text{Ze3}$ . As a result, the sensed voltage drop across SUT has predetermined current and therefore can be used to represent the impedance of SUT. A system with this kind

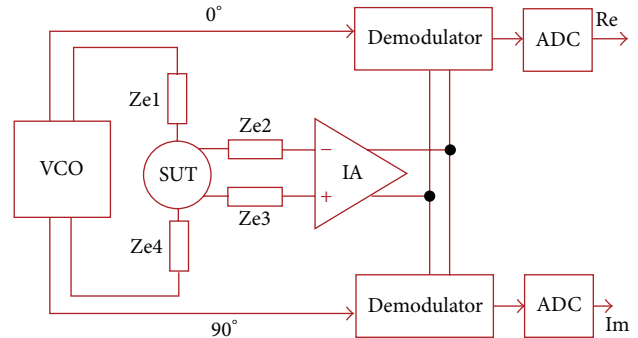


FIGURE 7: Impedance sensing architecture presented in [45], with which the four-electrode method accompanies, demonstrating the coherent demodulation technique.

of 4-electrode configuration is also known as a system using “tetrapolar method” [48].

To decompose the complex number of impedance, two orthogonal AC signals are required in the coherent demodulation, based on the Euler’s formula to represent a periodic signal using a combination of sine and cosine. The AC signals were generated in the same VCO to reduce the system complexity and save the implementation cost. The Demodulator circuits functioned as “mixer” and their outputs were quantized by the dedicated analog-to-digital converters (ADCs). The real part (Re) and imaginary part (Im) can be used to draw Nyquist plot for impedance analysis. It should be noticed that, practically, there still exists certain electric potential difference between  $\text{Ze2}$  and  $\text{Ze3}$  in spite of the zero current at the inputs of IA, and due to that  $\text{Ze2}$  and  $\text{Ze3}$  could not be identical. As a result, high CMRR is necessary to reject the potential difference of IA, resulting in design challenge. The major bottleneck in implementation is

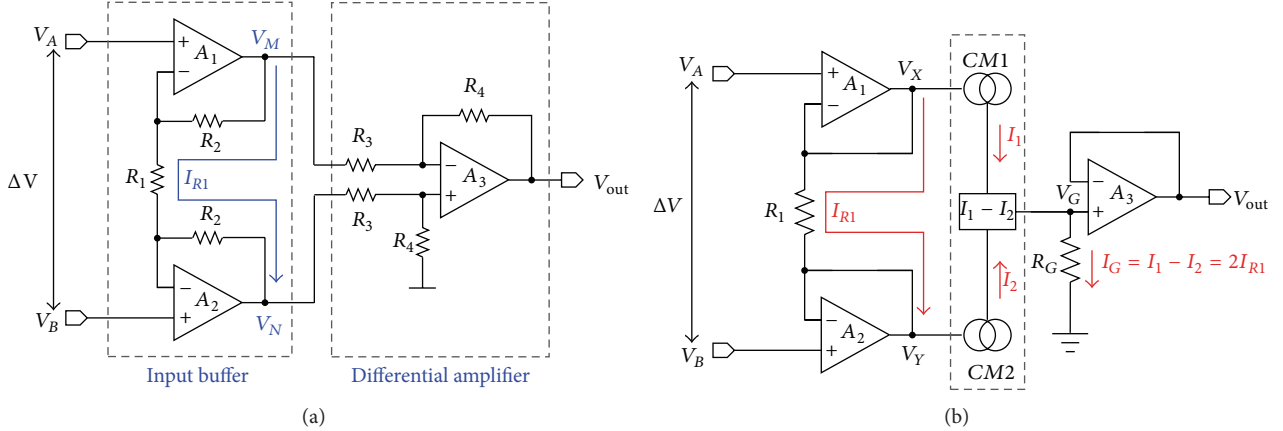


FIGURE 8: (a) The circuit schematic of conventional instrumentation amplifier (IA) in [50]. (b) The circuit schematic of improved counterpart in [51].

the matching of resistors involved in the commonly adopted IA structure shown in Figure 8(a) [50] where the output of IA can be expressed as

$$V_{out} = -\frac{R_4}{R_3} \left( 1 + \frac{2R_2}{R_1} \right) (V_A - V_B) = K_1 (V_A - V_B). \quad (1)$$

Achieving sufficient resistive matching between \$R\_4\$ and \$R\_3\$ (or \$R\_2\$ and \$R\_1\$) to obtain high CMRR relies on post-IC-fabrication trimming, which is cost ineffective and difficult to fulfill miniaturization in practice. As a result, the design shown in Figure 8(b) was proposed [51]. The most significant feature of the design is that it requires only two resistors. \$A\_1\$ and \$A\_2\$ form source followers as conventional, thereby forcing \$V\_A = V\_X\$ and \$V\_B = V\_Y\$. The current flowing out of \$A\_1\$ and that of \$A\_2\$ are equal, but they have opposite polarities. By using a current subtractor, marked in the dotted line, one can obtain \$I\_G = 2I\_{R1}\$; hence the output of IA becomes

$$V_{out} = \frac{2R_G}{R_1} (V_A - V_B) = K_2 (V_A - V_B). \quad (2)$$

This circuit structure successfully alleviates the impact of mismatched resistance, achieving both high CMRR and miniaturization at the cost of increased power consumption as compared with that shown in Figure 8(a). High CMRR can also be attained by means of considerably increased differential gain. Unfortunately, the energy efficiency of system is further compromised.

An often overlooked factor in correct impedance monitoring is that the electrode-referred DC offset (ERDO) limits the available CMRR, affecting the operation of IA and degrading overall performance no matter how good the following circuits and systems can be. Two renowned techniques have been proposed so far to cancel ERDO. A technique called “autozeroing” is shown in Figure 9(a) [52]. It uses three switches to cancel ERDO, \$V\_{OS}\$. When \$\phi\$ is at a logic-“high” level, the amplifier involved samples \$V\_{OS}\$ and store them on \$C\_S\$. Assuming that the open-loop gain of amplifier is \$A\$, the voltage on \$C\_S\$ will be \$V\_{OS} \cdot (A/(1+A))\$ after settling. When \$\phi\$ becomes a logic-“low” level, \$V\_{OS}\$ of previous

state will be subtracted from \$V\_i\$ which is superimposed with current \$V\_{OS}\$ which will be with the same value as that of previous state, resulting in a considerably decreased ERDO of \$V\_{OS} \cdot (1/(1+A))\$ present at the positive terminal of amplifier. The autozeroing technique can also effectively reduce the “flicker” noise of modern semiconductor process but comes with a penalty of high-frequency interference stemming from the sampling clocks of the switches. Its major drawback is the wide bandwidth of amplifier as a result of the voltage settling on \$C\_S\$.

Another efficient candidate is the work shown in Figure 9(b) where \$V\_{ip}\$ and \$V\_{in}\$ can be connected with \$Ze2\$ and \$Ze3\$, respectively. The circuit serves as a preamplifier located between the electrodes and IA to “continuously” remove ERDO [53]. Here we use single differential circuit configuration to detail its advantage but then it can turn into its fully differential counterpart to provide two output terminals to IA. The design embodies the AC coupling to reject ERDO in order to make itself free from malfunction as a result of the saturation. The low-frequency cutoff of the high-pass filter formed by the \$R\_2-C\_2\$ network can be adjusted through their time constant. The low-pass corner frequency can be adjusted by the time constant of the lumped impedance at the output of the preamplifier and \$C\_L\$. Owing to the low frequencies required by the impedance measurement, an extremely large \$R\_2-C\_2\$ time constant is unavoidable. As a result, a pseudoresistor configuration shown in Figure 9(c) can be adopted [53]. The pseudoresistor operates the transistors involved at “subthreshold” operation to achieve a large equivalent resistance value that is almost impossible to be realized on the basis of “on-chip” miniaturization. The closed-loop midband gain of the preamplifier can be determined by \$C\_1/C\_2\$.

It should also be noticed that the accuracy of current of measurement, signals generated from VCO for the demodulation and how accurate their frequencies and phases can be achieved by the system shown in Figure 7, will also affect the final outcome dramatically. The frequencies and phases can be adjusted and finely tuned by means of a phase-locked loops with a precise reference frequency [54]. Such

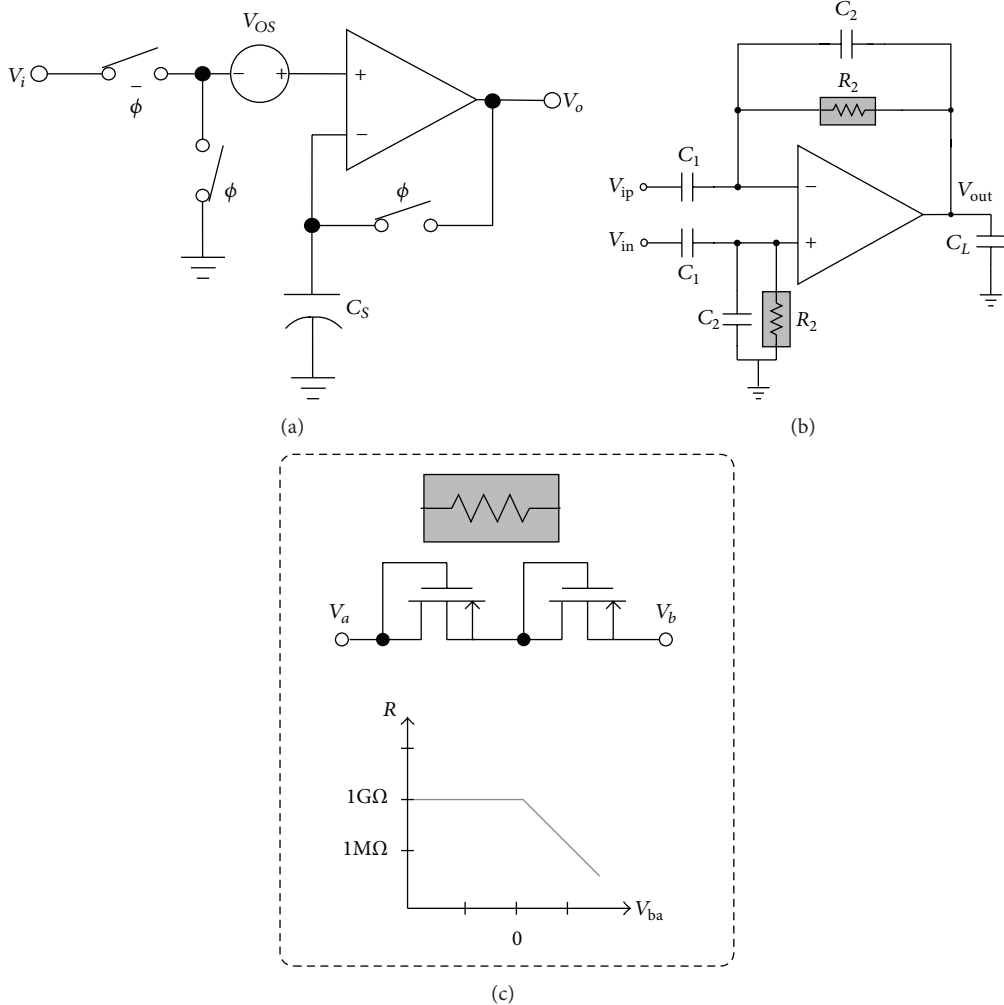


FIGURE 9: (a) The autozeroing technique [52]. (b) The AC-coupled technique [53]. (c) The pseudoresistor technique [53].

a frequency can be generated from an electronic circuit containing a mechanically resonant vibrating crystal (so-called crystal oscillator) [54]. Precise current of measuring SUT can be obtained through the use of a “current mirror” with sufficiently high output impedance. Modern semiconductor technologies offer many well developed and miniaturized circuit topologies to achieve such a goal [55, 56].

To advance miniaturization, the architecture shown in Figure 7 could be further improved as the complexity-reduced alternative shown in Figure 10 [48]. The architecture, which is called synchronous sampling, has mainly two most significant features: (a) removal of IA and (b) representing final results in pulse-width modulation (PWM) (using a one-bit ADC). The elements  $Z_{EA}$  to  $Z_{ED}$  correspond to the impedance of the four electrodes and the media were modeled by the elements  $Z_{MA}$  to  $Z_{MD}$ . Each of these impedances has real and imaginary components associated with the conductivity and dielectric properties of the media, respectively [48]. The voltage on the negative terminal of  $OTA_{BIAS}$  will be forced to become the reference voltage  $V_{ref}$  which was set to halve the supply voltage and was used as the “ground” in

the analog circuits involved, thanks to the high open-loop gains of the amplifiers achieving the “virtual short.” It turns out to be reducing the loss in the parasitic elements and avoiding the need for IA and the differential AC-coupled inputs. The demodulated results, followed by the low-pass filter (LPF), were compared with  $V_{ref}$  to obtain a PWM waveform that is easy to be transmitted wirelessly without parallel-serial converter commonly seen at the output of ADC for serial link. This architecture avoids two demodulation channels by incorporating a sampling mechanism using the proper sampling times.

Recently, a closed-loop architecture shown in Figure 11 was proposed [49]. Despite the same theory principle for impedance measurement, its target used to determine the final outcome is unlike the two representative architectures shown in Figures 7 and 10. In this design, the resulting voltage across the impedance under test (ZUT) including SUT will be confined to a predetermined amount using the error amplifier EA with the given reference voltage  $V_{ref}$  at its input. This will help to operate the electrodes involved in a linear and predictable region. The generated AC current  $i_X$  flowing through

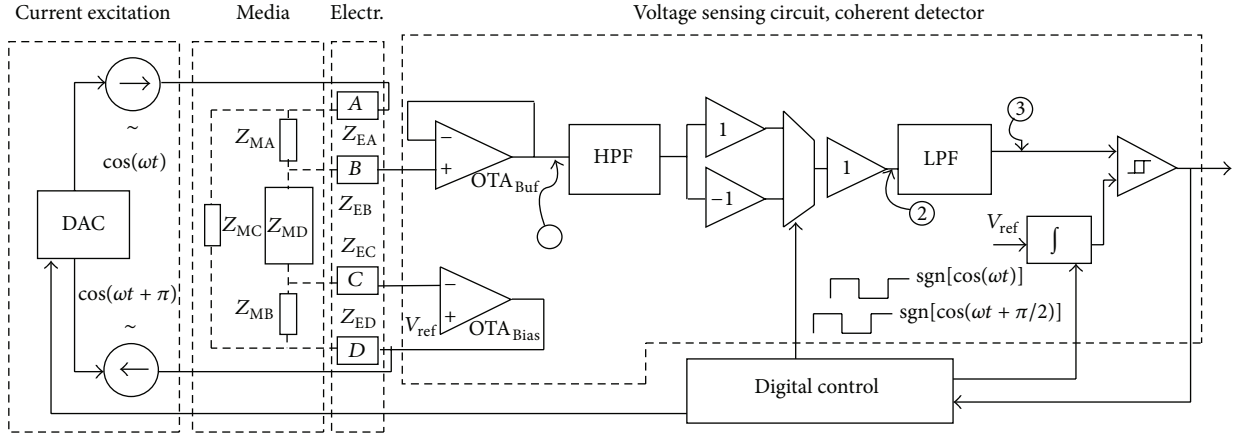


FIGURE 10: Synchronous sampling impedance sensing architecture. Copyright 2009. Reprinted from [48] with permission from Elsevier.

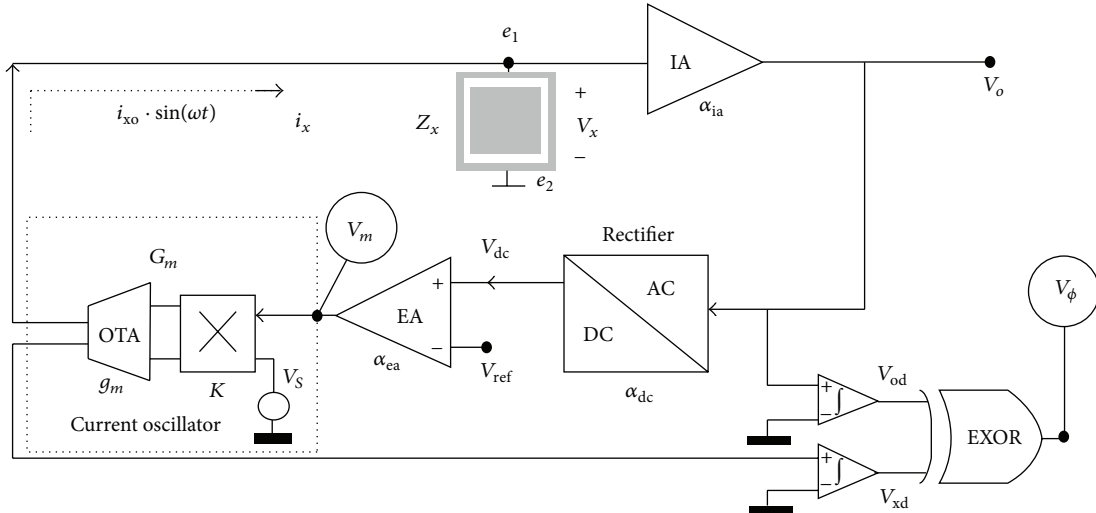


FIGURE 11: The closed-loop impedance sensing architecture. Copyright 2010. Reprinted from [49] with permission from Elsevier.

ZUT can be controlled timely as a result of the feedback loop at  $V_O$ . Because the transconductance of OTA ( $g_m$ ) can be deduced during design and measurement phases and both the multiplication factor  $K$  and signal source  $V_S$  can be given,  $i_X$  can be obtained, provided that  $V_m$  is available after being monitored. With  $V_X$  and  $i_X$ , the impedance “magnitude” of ZUT can be measured. The impedance “phase” can be measured by comparing the digitized results  $V_{od}$  and  $V_{xd}$  of  $V_O$  and the output of OTA to each other.

Although the architecture shown in Figure 11 provides a good candidate to achieve not only an operation taking the contribution of electrodes into account but also a safe measurement with a decent accuracy as compared with others demonstrated in the literature, its overall performance is governed by the bandwidth, open-loop gain, input offset, and CMRR of amplifier, similar to its counterparts. However, high-gain, wide-bandwidth, low-offset, and high-CMRR

amplifier consumes considerable power consumption, which goes against portability requiring miniaturization. In a nutshell, it has been believed that the performance of analog front end is of primary importance for the precise measurement of impedimetric system. The miniaturization effort involves making trade-offs among different aspects of mixed-signal (analog and digital) circuit design. The technical strategies illustrated with Figures 8 and 9 are by no means the total solutions but have demonstrated that they can be used to effectively deal with the mentioned problems in terms of miniaturization point of view. Last but not least, with regard to some implantable applications where an extremely miniaturized design of real-time impedance monitoring must be fulfilled in limited space to allowing integration to the most degree, the test current of SUT and ZUT could be generated by an electrical stimulator without the dedicated circuit such as VCO, DAC, or current oscillator shown in Figures 7, 10,

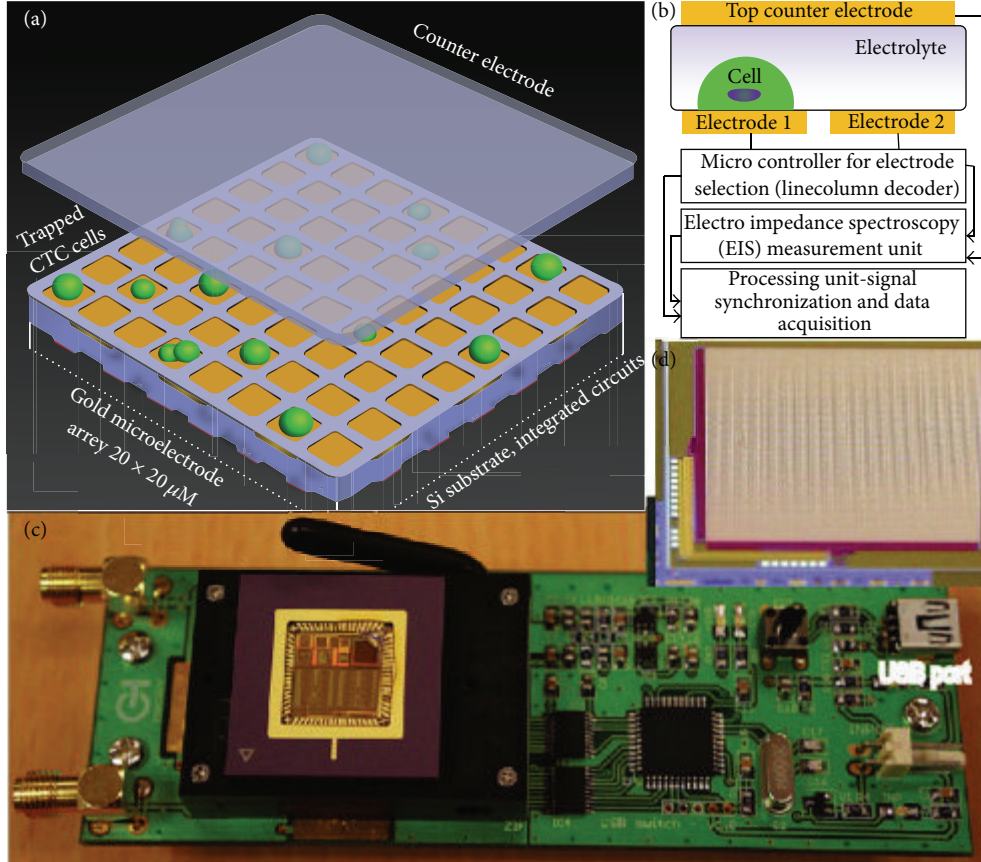


FIGURE 12: CMOS based sensor array for cell counting. (a) Schematic of the microelectrode arrays for the cell detection. (b) Illustration of the sensor layout and the addressing scheme employed in the CMOS sensor chip. (c) CMOS chip packaged with a switching PCB. (d) Microphotograph of more than nine thousand electrodes in a single chip. Copyright 2012. Reprinted from [57] with permission from Elsevier.

and 11, respectively [56, 58, 59]. This turns out to be good for the system on a chip (SoC) in modern semiconductor technologies.

## 8. Impedimetric Imaging Instrumentation in Omics

We have reviewed in detail the technologies regarding miniaturization. One might want to know the relevance between them and “imaging.” For the delivery of next-generation therapies, functional characterization of genes using a systematic way is imperative. One of the manners doing this kind of characterization requires downregulation of the expression of specific genes in order to comprehensively study the functions of genes [60]. To this end, the cell-based functional assay has been emerged as one of the powerful tools for acute observation [61]. The cell-based functional assay can be used to acquire the information about the phenotypic effect of targeted “gene knockdown,” which is a technique to reduce the expression of one or more of an organism’s genes, in a way “incisive” when using RNA interference (RNAi) [62]. However, almost all of the assays are used only for experiencing a rapid onset (i.e., to say “for a given point of time”) currently, implying that most of the changes are

missed in measurement. In addition, it has been demonstrated that advanced state-of-the-art electronic biosensors with microwell plates should be developed to be able to record impedimetric cell-to-electrode responses in a way “label-free” by means of microelectrodes. The combination of the requirements “continuous monitoring,” “impedimetric cell-to-electrode recording,” and “bidimensional-space (2D) electrode array manipulation” form the base of new-generation time-dependent profiling for cell responses. One of the most recent works with respect to the development of impedimetric spectrum platform with different application regarding cell has been demonstrated in Figure 12 where advanced semiconductor process and circuit techniques have been employed to advance miniaturized sensing system with light weight and low power in the platform [57]. By displaying the results of 2D spectrum continuously, real-time impedimetric imaging can be realized to ceaselessly measure the cell status of importance.

## 9. Concluding Remarks

The ever increasing demand in the modern technologies has improved the quality of life. Microfluidic systems have been applied to different genomic applications and showed

realizable opportunity for point-of-care diagnostic devices. The advances in circuits and systems have been driving a technical revolution in the microfluidic systems that are essential to the “-omics” era. Impedimetric detection is a promising technique to develop miniaturized measurement equipment. The improved impact on the SoC techniques has enabled sustainable solutions which have been demonstrated so far to be effective to pressing real problems in such a field. Several representative solutions ranging from impedimetric architectures and efficiency-enhanced miniaturized techniques have been discussed in detail in this paper. Many researchers have pursued the ideas of using the techniques they have learned to facilitate interdisciplinary collaborations among SoC design, micromechanical technologies, material science, and biomedical engineering. It is almost impossible to embody miniaturization towards light weight and low power, while at the same time achieving an accurate impedance signal conditioning and the reduced response time without the help of microfabricated and mixed-signal technologies, not to mention the portability. In addition to the applications and advantages mentioned, it can be envisioned that by leveraging the architectures and techniques, low-price and precise early detection of many fatal diseases, such as the cancers, will eventually come true. Despite the strength and importance of impedance measurement system, those prior arts suffer the most from the contamination of electrode. Once the electrodes dip into the sample, non-specific adsorption of biological components starts to take place. The contamination of electrode is still an open question and is accompanied with distortion of measured impedance spectrum, resulting in observable (inductive) artifact at some frequencies. In order to eliminate the contamination of detection electrodes and reaction chamber, the device is normally designed to be disposable for the rapid diagnostic applications. Moreover, the electrodes are made of noble metals, for example, Au and Pt, in order to prevent the surface oxidation. The contamination may also be overcome by having a large number of in vitro tests on electrode-sample reactions (redox) as an index of lookup stored in an on-chip memory. This may greatly help differentiate the shifted impedance spectrum from its normal circumstances (through some kinds of algorithms). In conclusion, the microfluidic systems incorporated with impedimetric detection technique provide simple, miniaturized, and sensitive detection of genomic signal. It is believed that these systems can develop practical point-of-care genomic diagnostic devices.

## Conflict of Interests

The authors declare that there is no conflict of interests regarding the publication of this paper.

## Acknowledgments

This study was supported in part by the National Science Council (NSC), Taiwan, under Grant no. NSC 102-2218-E-182-003-. The authors would also like to thank funding support from the Chang Gung University, Taiwan, and

Chang Gung Memorial Hospital, Taiwan, under Grants nos. UERPD2D0011, CMRPD2C0141, and CMRPD2D0021.

## References

- [1] D. Erickson, X. Liu, U. Krull, and D. Li, “Electrokinetically controlled DNA hybridization microfluidic chip enabling rapid target analysis,” *Analytical Chemistry*, vol. 76, no. 24, pp. 7269–7277, 2004.
- [2] P. K. Yuen, G. Li, Y. Bao, and U. R. Müller, “Microfluidic devices for fluidic circulation and mixing improve hybridization signal intensity on DNA arrays,” *Lab on a Chip*, vol. 3, no. 1, pp. 46–50, 2003.
- [3] R. H. Liu, R. Lenigk, R. L. Druyor-Sanchez, J. Yang, and P. Grodzinski, “Hybridization enhancement using cavitation microstreaming,” *Analytical Chemistry*, vol. 75, no. 8, pp. 1911–1917, 2003.
- [4] M. K. McQuain, K. Seale, J. Peek et al., “Chaotic mixer improves microarray hybridization,” *Analytical Biochemistry*, vol. 325, no. 2, pp. 215–226, 2004.
- [5] Y. C. Chung, Y. C. Lin, M. Z. Shiu, and W. N. T. Chang, “Microfluidic chip for fast nucleic acid hybridization,” *Lab on a Chip*, vol. 3, no. 4, pp. 228–233, 2003.
- [6] D. R. Reyes, D. Iossifidis, P. A. Auroux, and A. Manz, “Micro total analysis systems. 1. Introduction, theory, and technology,” *Analytical Chemistry*, vol. 74, no. 12, pp. 2623–2636, 2002.
- [7] P.-A. Auroux, D. Iossifidis, D. R. Reyes, and A. Manz, “Micro total analysis systems. 2. Analytical standard operations and applications,” *Analytical Chemistry*, vol. 74, no. 12, pp. 2637–2652, 2002.
- [8] T. Vilkner, D. Janasek, and A. Manz, “Micro total analysis systems. Recent developments,” *Analytical Chemistry*, vol. 76, no. 12, pp. 3373–3386, 2004.
- [9] Y. Zhang and P. Ozdemir, “Microfluidic DNA amplification—a review,” *Analytica Chimica Acta*, vol. 638, no. 2, pp. 115–125, 2009.
- [10] A. Bange, H. B. Halsall, and W. R. Heineman, “Microfluidic immunosensor systems,” *Biosensors and Bioelectronics*, vol. 20, no. 12, pp. 2488–2503, 2005.
- [11] K. F. Lei, “Microfluidic systems for diagnostic applications: a review,” *Journal of Laboratory Automation*, vol. 17, pp. 330–347, 2012.
- [12] Y. Xia and G. M. Whitesides, “Soft lithography,” *Annual Review of Materials Science*, vol. 28, no. 1, pp. 153–184, 1998.
- [13] A. Gerlach, G. Knebel, A. E. Guber et al., “Microfabrication of single-use plastic microfluidic devices for high-throughput screening and DNA analysis,” *Microsystem Technologies*, vol. 7, no. 5-6, pp. 265–268, 2002.
- [14] W. W. Y. Chow, K. F. Lei, G. Shi, W. J. Li, and Q. Huang, “Microfluidic channel fabrication by PDMS-interface bonding,” *Smart Materials and Structures*, vol. 15, pp. S112–S116, 2006.
- [15] K. F. Lei, S. Ahsan, N. Budraa, W. J. Li, and J. D. Mai, “Microwave bonding of polymer-based substrates for potential encapsulated micro/nanofluidic device fabrication,” *Sensors and Actuators A: Physical*, vol. 114, no. 2-3, pp. 340–346, 2004.
- [16] Z. J. Jia, Q. Fang, and Z.-L. Fang, “Bonding of glass microfluidic chips at room temperatures,” *Analytical Chemistry*, vol. 76, no. 18, pp. 5597–5602, 2004.
- [17] C. W. Tsao and D. L. DeVoe, “Bonding of thermoplastic polymer microfluidics,” *Microfluidics and Nanofluidics*, vol. 6, no. 1, pp. 1–16, 2009.

- [18] K. F. Lei, H. Cheng, K. Y. Choy, and L. M. C. Chow, "Electrokinetic DNA concentration in microsystems," *Sensors and Actuators A: Physical*, vol. 156, no. 2, pp. 381–387, 2009.
- [19] Y. He, M. Tsutsui, C. Fan, M. Taniguchi, and T. Kawai, "Gate manipulation of DNA capture into nanopores," *ACS Nano*, vol. 5, no. 10, pp. 8391–8397, 2011.
- [20] M. A. Burns, B. N. Johnson, S. N. Brahmasandra et al., "An integrated nanoliter DNA analysis device," *Science*, vol. 282, no. 5388, pp. 484–487, 1998.
- [21] F. Wang and M. A. Burns, "Performance of nanoliter-sized droplet-based microfluidic PCR," *Biomedical Microdevices*, vol. 11, no. 5, pp. 1071–1080, 2009.
- [22] L. Shui, J. G. Bomer, M. Jin, E. T. Carlen, and A. van den Berg, "Microfluidic DNA fragmentation for on-chip genomic analysis," *Nanotechnology*, vol. 22, no. 49, Article ID 494013, 2011.
- [23] J. Khandurina, T. E. McKnight, S. C. Jacobson, L. C. Waters, R. S. Foote, and J. M. Ramsey, "Integrated system for rapid PCR-based DNA analysis in microfluidic devices," *Analytical Chemistry*, vol. 72, no. 13, pp. 2995–3000, 2000.
- [24] D. Sabourin, J. Petersen, D. Snakenborg et al., "Microfluidic DNA microarrays in PMMA chips: streamlined fabrication via simultaneous DNA immobilization and bonding activation by brief UV exposure," *Biomedical Microdevices*, vol. 12, no. 4, pp. 673–681, 2010.
- [25] A. H. Diercks, A. Ozinsky, C. L. Hansen, J. M. Spotts, D. J. Rodriguez, and A. Aderem, "A microfluidic device for multiplexed protein detection in nano-liter volumes," *Analytical Biochemistry*, vol. 386, no. 1, pp. 30–35, 2009.
- [26] K. F. Lei, "Quantitative electrical detection of immobilized protein using gold nanoparticles and gold enhancement on a biochip," *Measurement Science and Technology*, vol. 22, no. 10, Article ID 105802, 2011.
- [27] K. F. Lei and Y. K. C. Butt, "Colorimetric immunoassay chip based on gold nanoparticles and gold enhancement," *Microfluidics and Nanofluidics*, vol. 8, no. 1, pp. 131–137, 2010.
- [28] A. E. Herr, A. V. Hatch, D. J. Throckmorton et al., "Microfluidic immunoassays as rapid saliva-based clinical diagnostics," *Proceedings of the National Academy of Sciences of the United States of America*, vol. 104, no. 13, pp. 5268–5273, 2007.
- [29] A. Bhattacharyya and C. M. Klapperich, "Design and testing of a disposable microfluidic chemiluminescent immunoassay for disease biomarkers in human serum samples," *Biomedical Microdevices*, vol. 9, no. 2, pp. 245–251, 2007.
- [30] S. Lai, S. Wang, J. Luo, L. J. Lee, S. T. Yang, and M. J. Madou, "Design of a compact disk-like microfluidic platform for enzyme-linked immunosorbent assay," *Analytical Chemistry*, vol. 76, no. 7, pp. 1832–1837, 2004.
- [31] D. Yang, X. Niu, Y. Liu et al., "Electrospun nanofibrous membranes: a novel solid substrate for microfluidic immunoassays for HIV," *Advanced Materials*, vol. 20, no. 24, pp. 4770–4775, 2008.
- [32] T. Glawdel and C. L. Ren, "Electro-osmotic flow control for living cell analysis in microfluidic PDMS chips," *Mechanics Research Communications*, vol. 36, no. 1, pp. 75–81, 2009.
- [33] F. T. G. van den Brink, E. Gool, J.-P. Frimat, J. Bomer, A. van den Berg, and S. le Gac, "Parallel single-cell analysis microfluidic platform," *Electrophoresis*, vol. 32, no. 22, pp. 3094–3100, 2011.
- [34] R. N. Zare and S. Kim, "Microfluidic platforms for single-cell analysis," *Annual Review of Biomedical Engineering*, vol. 12, pp. 187–201, 2010.
- [35] G. Mehta, J. Lee, W. Cha, Y.-C. Tung, J. J. Linderman, and S. Takayama, "Hard top soft bottom microfluidic devices for cell culture and chemical analysis," *Analytical Chemistry*, vol. 81, no. 10, pp. 3714–3722, 2009.
- [36] K. F. Lei and P. H. M. Leung, "Microelectrode array biosensor for the detection of *Legionella pneumophila*," *Microelectronic Engineering*, vol. 91, pp. 174–177, 2012.
- [37] K. F. Lei, M. H. Wu, C. W. Hsu, and Y. D. Chen, "Real-time and non-invasive impedimetric monitoring of cell proliferation and chemosensitivity in a perfusion 3D cell culture microfluidic chip," *Biosensors and Bioelectronics*, vol. 51, pp. 16–21, 2014.
- [38] K. F. Lei, M. H. Wu, P. Y. Liao, Y. M. Chen, and T. M. Pan, "Development of a micro-scale perfusion 3D cell culture biochip with an incorporated electrical impedance measurement scheme for the quantification of cell number in a 3D cell culture construct," *Microfluidics and Nanofluidics*, vol. 12, no. 1–4, pp. 117–125, 2012.
- [39] M. Bu, T. Melvin, G. Ensell, J. S. Wilkinson, and A. G. R. Evans, "Design and theoretical evaluation of a novel microfluidic device to be used for PCR," *Journal of Micromechanics and Microengineering*, vol. 13, pp. S125–S130, 2003.
- [40] K.-S. Ma, H. Zhou, J. Zoval, and M. Madou, "DNA hybridization detection by label free versus impedance amplifying label with impedance spectroscopy," *Sensors and Actuators B: Chemical*, vol. 114, no. 1, pp. 58–64, 2006.
- [41] S. J. Park, T. A. Taton, and C. A. Mirkin, "Array-based electrical detection of DNA with nanoparticle probes," *Science*, vol. 295, no. 5559, pp. 1503–1506, 2002.
- [42] C. Fang, Y. Fan, J. Kong, Z. Gao, and N. Balasubramanian, "Electrical detection of oligonucleotide using an aggregate of gold nanoparticles as a conductive tag," *Analytical Chemistry*, vol. 80, no. 24, pp. 9387–9394, 2008.
- [43] R. L. Testerman, N. R. Hagfors, and S. I. Schwartz, "Design and evaluation of nerve stimulating electrodes," *Medical research engineering*, vol. 10, no. 1, pp. 6–11, 1971.
- [44] M. Sawan, F. Mounaim, and G. Lesbros, "Wireless monitoring of electrode-tissues interfaces for long term characterization," *Analog Integrated Circuits and Signal Processing*, vol. 55, no. 1, pp. 103–114, 2008.
- [45] A. Yufera, G. Leger, E. O. Rodriguez-Villegas et al., "An integrated circuit for tissue impedance measure," in *Proceedings of the 2nd Annual International IEEE-EMB Special Topic Conference on Microtechnologies in Medicine & Biology*, pp. 88–93, Madison, Wis, USA, 2002.
- [46] A. Yúfera, A. Rueda, J. M. Muñoz, R. Doldán, G. Leger, and E. O. Rodríguez-Villegas, "A tissue impedance measurement chip for myocardial ischemia detection," *IEEE Transactions on Circuits and Systems I: Regular Papers*, vol. 52, no. 12, pp. 2620–2628, 2005.
- [47] R. Pallas-Areny and J. G. Webster, "Bioelectric impedance measurements using synchronous sampling," *IEEE Transactions on Biomedical Engineering*, vol. 40, no. 8, pp. 824–829, 1993.
- [48] J. Sacristán-Riquelme, F. Segura-Quijano, A. Baldi, and M. Teresa Osés, "Low power impedance measurement integrated circuit for sensor applications," *Microelectronics Journal*, vol. 40, no. 1, pp. 177–184, 2009.
- [49] A. Yúfera and A. Rueda, "Design of a CMOS closed-loop system with applications to bio-impedance measurements," *Microelectronics Journal*, vol. 41, no. 4, pp. 231–239, 2010.
- [50] A. S. Sedra and K. C. Smith, *Microelectronic Circuit*, Oxford University Press, New York, NY, USA, 5th edition, 2007.

- [51] A. Harb and M. Sawan, "New low-power low-voltage high-CMRR CMOS instrumentation amplifier," in *Proceedings of the IEEE International Symposium on Circuits and Systems (ISCAS '99)*, vol. 6, pp. 97–100, June 1999.
- [52] C. C. Enz and G. C. Temes, "Circuit techniques for reducing the effects of Op-Amp imperfections: autozeroing, correlated double sampling, and chopper stabilization," *Proceedings of the IEEE*, vol. 84, no. 11, pp. 1584–1614, 1996.
- [53] R. R. Harrison and C. Charles, "A low-power low-noise CMOS amplifier for neural recording applications," *IEEE Journal of Solid-State Circuits*, vol. 38, no. 6, pp. 958–965, 2003.
- [54] J. A. Tierno, A. V. Rylyakov, and D. J. Friedman, "A wide power supply range, wide tuning range, all static cmos all digital pll in 65 nm SOI," *IEEE Journal of Solid-State Circuits*, vol. 43, pp. 42–51, 2008.
- [55] C. S. Alex Gong, K. W. Yao, and M. T. Shiue, "A CMOS multi-channel electrical stimulation prototype system," *International Journal of Circuit Theory and Applications*, vol. 41, no. 3, pp. 238–258, 2013.
- [56] M. Ghovanloo and K. Najafi, "A wireless implantable multichannel microstimulating system-on-a-chip with modular architecture," *IEEE Transactions on Neural Systems and Rehabilitation Engineering*, vol. 15, no. 3, pp. 449–457, 2007.
- [57] Y. Chen, C. C. Wong, T. S. Pui et al., "CMOS high density electrical impedance biosensor array for tumor cell detection," *Sensors and Actuators B: Chemical*, vol. 173, pp. 903–907, 2012.
- [58] G. Lesbros and M. Sawan, "Multiparameters monitoring for long term in-vivo characterization of electrode-tissues contacts," in *Proceedings of the 13th IEEE International Conference on Electronics, Circuits and Systems (ICECS '06)*, pp. 25–28, Nice, France, December 2006.
- [59] C. S. A. Gong, K. W. Yao, M. T. Shiue, and Y. Chang, "An impedance measurement analog front end for wirelessly bioimplantable applications," in *Proceedings of the IEEE Asia Pacific Conference on Circuits and Systems (APCCAS '12)*, pp. 172–175, Kaohsiung, Taiwan, December 2012.
- [60] I. Bantounas, L. A. Phylactou, and J. B. Unney, "RNA interference and the use of small interfering RNA to study gene function in mammalian systems," *Journal of Molecular Endocrinology*, vol. 33, no. 3, pp. 545–557, 2004.
- [61] Y. A. Abassi, B. Xi, W. Zhang et al., "Kinetic cell-based morphological screening: prediction of mechanism of compound action and off-target effects," *Chemistry and Biology*, vol. 16, no. 7, pp. 712–723, 2009.
- [62] "Using the xCELLigence System for Functional Genomics: Assessing Gene Function in Real Time," Application Note of ACEA Biosciences, Inc.

## Review Article

# The Role of Imaging in Radiation Therapy Planning: Past, Present, and Future

Gisele C. Pereira,<sup>1</sup> Melanie Traughber,<sup>2</sup> and Raymond F. Muzic Jr.<sup>3,4</sup>

<sup>1</sup> Department of Radiation Oncology, University Hospitals Case Medical Center, Case Western Reserve University, Cleveland, OH 44106, USA

<sup>2</sup> Philips Healthcare, MR Therapy, Cleveland, OH, USA

<sup>3</sup> Case Center for Imaging Research, Case Western Reserve University, Cleveland, OH, USA

<sup>4</sup> Department of Radiology, University Hospitals Case Medical Center, Case Western Reserve University, Cleveland, OH 44106, USA

Correspondence should be addressed to Raymond F. Muzic Jr.; raymond.muzic@case.edu

Received 19 December 2013; Accepted 17 February 2014; Published 10 April 2014

Academic Editor: Tzu-Chen Yen

Copyright © 2014 Gisele C. Pereira et al. This is an open access article distributed under the Creative Commons Attribution License, which permits unrestricted use, distribution, and reproduction in any medium, provided the original work is properly cited.

The use of ionizing radiation for cancer treatment has undergone extraordinary development during the past hundred years. The advancement of medical imaging has been critical in helping to achieve this change. The invention of computed tomography (CT) was pivotal in the development of treatment planning. Despite some disadvantages, CT remains the only three-dimensional imaging modality used for dose calculation. Newer image modalities, such as magnetic resonance (MR) imaging and positron emission tomography (PET), are also used secondarily in the treatment-planning process. MR, with its better tissue contrast and resolution than those of CT, improves tumor definition compared with CT planning alone. PET also provides metabolic information to supplement the CT and MR anatomical information. With emerging molecular imaging techniques, the ability to visualize and characterize tumors with regard to their metabolic profile, active pathways, and genetic markers, both across different tumors and within individual, heterogeneous tumors, will inform clinicians regarding the treatment options most likely to benefit a patient and to detect at the earliest time possible if and where a chosen therapy is working. In the post-human-genome era, multimodality scanners such as PET/CT and PET/MR will provide optimal tumor targeting information.

## 1. Introduction to Radiation Therapy

The three most important aspects of cancer treatment are surgery, chemotherapy (in earlier times referred to simply as medicine), and radiation therapy. Of these, surgery is the oldest with records discovered by Edwin Smith, an American Egyptologist, and describing the surgical treatment of cancer in Egypt circa 1600 B.C. [1]. Medicines were also used in ancient Egypt at the time of the pharaohs, although the use of chemotherapy in cancer was first used in the early 1900s by the German chemist, Paul Ehrlich [2]. In contrast, radiation therapy, the therapeutic use of ionizing radiation, is by far the most recent technique used to treat cancer. X-rays, a kind of ionizing radiation, were discovered in 1895 by Wilhelm Roentgen and within months were used to treat tumors. This use of ionizing radiation has undergone extraordinary

development during the past century. As we will discuss, the advancements in medical imaging have been critical to the evolution of modern radiation therapy.

In the late nineteenth century, three discoveries regarding ionizing radiation were instrumental in the development of radiation therapy:

- (1) November 8, 1895: X-rays discovered by Wilhelm Conrad Roentgen (1845–1923);
- (2) March 1, 1896: radioactivity discovered by Henri Becquerel (1852–1908);
- (3) December 26, 1898: radium discovered by Madame Curie (Maria Skłodowska) (1867–1934).

There are two, general classes of radiation therapy: brachytherapy and teletherapy. “Brachy,” a Greek word,

TABLE 1

Accelerator voltage	Mean photon energy	Classification
10–150 kV	3–50 keV	Superficial
150–500 kV	50–166 keV	Orthovoltage
500–1000 kV	166–333 keV	Supervoltage
>1000 kV (1 MV)	>333 keV (0.33 MeV)	Megavoltage

means short distance and “tele” means long distance. Brachytherapy is treatment performed by placing the radioactive source near or in contact with a tumor, that is, the use of intracavitary or intraluminal placement of the treatment source. Conversely, teletherapy is treatment with the radioactive source at a distance from the patient/tumor. Teletherapy, also known as external beam radiation therapy, may be classified by the voltage applied to produce X-ray photons as in Table 1 [3].

The lower energy beams, produced by X-ray tubes, are well suited for diagnostic imaging. However, the use of these lower energy beams is limited in radiation therapy. Because these beams are highly attenuated, that is, poorly penetrating, the treatment of deep tumors results in an excessive radiation dose to the skin, thus limiting the ability to deliver curative doses, and so are of limited clinical usefulness. In order to treat deep tumors while maintaining a lower radiation skin dose, high-energy beams with greater penetrating power are required.

High-energy gamma-ray photons are emitted during radioactive decay of certain radionuclides. (X-rays and gamma-rays are both photons and produce the same interactions with tissue. They differ according to their origin. Gamma-rays originate from the changes between energy levels in the nucleus, while X-rays originate from changes between energy levels in the electrons orbiting the nucleus.) External-beam radiation therapy units may be created by collimating the gamma-ray emissions from large quantities of radioactive material. Examples of these units are telerdium utilizing Radium-226 and emitting gamma-rays with average energy of 1.2 MeV, telecesium utilizing Cesium-137 and emitting gamma-rays with average energy of 0.66 MeV, and the Cobalt-60 unit emitting gamma-rays at 1.17 MeV and 1.33 MeV. All of these units require storage of large amounts of radioactive materials and have associated radiation safety concerns, including securing the materials so that they are not used for terrorist activities. Therefore, the use of radioactive materials has largely been replaced by megavoltage machines.

The first megavoltage machine used to produce therapeutic X-rays was a type of accelerator called the Van de Graaff generator. It is an electrostatic accelerator which accelerates charged particles, in this case electrons. The high-energy electrons strike a target to create X-rays from 1 to 2 MeV in energy. Its first clinical use was at Huntington Memorial Hospital in Boston when it was installed in 1937.

Another type of accelerator used in radiation therapy is a betatron which has a hollow, doughnut shape with an alternating magnetic field to accelerate electrons. These accelerators were used specifically for the production of therapeutic electron beams, rather than X-rays. Most of these units were installed in European medical centers, had electron energies up to 50 MeV, and were used to treat deeply located tumors.

Van de Graaff generators and betatrons were the precursors of linear accelerators or “linacs.” Linacs to be used for radiation therapy were developed during and after World War II and used the high-frequency and high-power microwave sources developed for the manufacture of radar systems. Linacs accelerate charged particles, most commonly electrons, to create therapeutic electron or X-ray beams up to 25 MeV in energy. Electrons achieve acceleration by traveling through a high electronic field in a magnetic field that causes the electrons to take a spiral path of increasing radius. X-rays are produced when these accelerated electrons collide with a high-atomic-number target. In 1953, the first isocentric linac was installed at the Christie Hospital in Manchester, United Kingdom, and these units continue to be the mainstay of modern radiation therapy. The chronology of the development of linear accelerators for radiotherapy use is as follows:

- 1953: first isocentric linac installed, United Kingdom;
- 1954: first dual-throttle (X-rays and electrons) linac installed, St Bartholomew's Hospital, London;
- 1973: first dual-photon-energy linac installed, Antoni van Leeuwenkoek, Amsterdam;
- 1981: introduction of motorized collimators;
- 1985: new series of fully computer-controlled linacs established, thus allowing the development of modern radiotherapy of high complexity.

## 2. Past: Introduction of Imaging in Radiation Therapy Planning

Together with the progress of radiation therapy linacs was the development of dose calculation and treatment-planning techniques. The ability to quantify the delivered dose evolved from simple skin erythema observations in the late 1800s to single-point calculations inside the patient in the mid 1900's and to computer-based dose calculations in the late 1960s. Finally, with the invention of computed tomography (CT) by Cormack and Hounsfield in 1972, three-dimensional (3D) dose calculation became possible. The use of CT in treatment planning allowed several important advances in radiation therapy and resulted in greater precision in dose distribution, dose optimization, and patient positioning. However, one of the most important advances CT provided for 3D dose calculation was the precise visualization of the geometric positions of tumor and normal tissue in a patient. The radiation dose could then be calculated and optimized in order to determine the best dose distribution in the target (tumor), thus avoiding the surrounding normal tissue. Another advance CT offered was the creation of digitally reconstructed radiographs or DRRs (Figure 1) for patient position verification at the time of treatment using the linac.

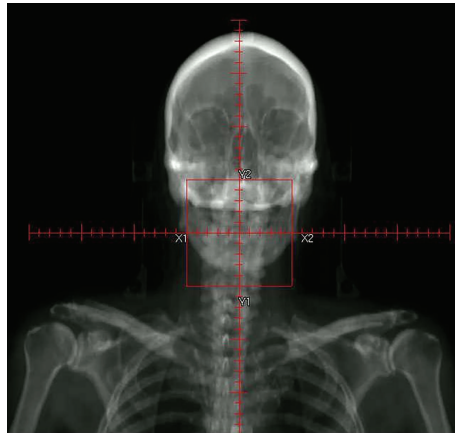


FIGURE 1: Creation of digital reconstructed radiographs or DRRs from CT.

### 3. Present: What Is Used in Practice Today

Currently, radiation therapy linacs are fully controlled by computers and with new techniques of dose delivery, such as intensity-modulated radiation therapy (IMRT), volumetric-modulated arc therapy (VMAT), and imaged-guided radiotherapy (IGRT), the treatment delivery precision is measured in millimeters [4]. A more precise method of target definition is necessary for such precise delivery. While CT has revolutionized the field of radiation therapy, further improvements in imaging are desirable in which the dose can be delivered with yet increased accuracy. CT has several limitations such as suboptimal tissue contrast, lack of functional information, and the inability to visualize small groups of cancer cells that are separated from the gross tumor. If we can overcome these limitations, we can further improve the precision of the target definition and provide better patient outcomes [5].

The application of other imaging modalities, such as magnetic resonance (MR) imaging and positron emission tomography (PET), can provide additional information in order to more precisely define tumor localization for treatment planning using radiation therapy [6–8]. In particular, MR has better soft-tissue contrast than CT and provides better visual discrimination between tissue that should be treated and that which should not (Figure 2) [9, 10]. PET allows the identification of areas of metabolic activity and thus allows the radiation oncologist to escalate the radiation dose for the most aggressively growing tumors or regions therein [11, 12] (Figure 3). Despite its limitations, for several reasons CT is currently the only 3D imaging method accepted for treatment planning. Most treatment-planning algorithms were developed specifically for CT as it was the first available 3D imaging modality and CT scanners are more commonly used than MR or PET. Furthermore, the geometric fidelity of CT is better than that of MR in which distortions may occur, and as CT generally has shorter acquisition times than MR or PET, organ/tumor motion management can be assessed. Most importantly, with CT it is possible to identify the mass attenuation coefficient ( $\mu/\rho$  ( $\text{m}^2/\text{Kg}$ ))

or attenuation characteristics for high-energy photons, X-rays, and gamma-rays, as this is critical for precise dose calculation.

Photon interactions with tissue, such as photo-electric absorption, Compton scatter, and pair production, are dependent on the atomic number, electron density of the tissue, and photon energy (Figure 4). Therefore, to accurately calculate the radiation dose, the specific mass attenuation factor for different types of tissue, that is, heterogeneity, encountered by a photon beam must be identified. For this reason the treatment planning dose calculation is still only possible using CT. Newly developed algorithms, such as convolution/superposition and Monte Carlo, provide more accurate dose calculations by using heterogeneity correction [13]. These new algorithms calculate the radiation absorption and scatter of different tissue densities and apply that to the dose calculation, although this is only possible because the tissue density is obtained using a table that relates the Hounsfield number to density. Four-dimensional CT (4DCT) is another development used to quantify respiratory and organ motion. Normally, the 4DCT is applied in thoracic and abdominal sites in which respiratory motion can cause incorrect information regarding the size and position of a tumor and critical organs [14].

The primary disadvantage of CT for treatment planning is the low tissue contrast which can result in the tumor definition varying significantly from physician to physician [15]. Other imaging modalities, such as MR and PET, may help in the tumor definition due to their improved soft-tissue contrast and functional information [16, 17]. Therefore, in contemporary radiation therapy practice MR and PET are often used to complement CT for tumor delineation and normal tissue identification, although only CT is used for dose calculation. Therefore, the ability to accurately coregister these various image sets is one of the most powerful tools for radiation therapy planning.

**3.1. MR.** Paul Lauterbur, at the State University of New York, USA, and Peter Mansfield, at the University of Nottingham, England, independently produced the first NMR image, now called MR, in the 1970s. Their invention had a profound impact on medical imaging, and they shared the 2003 Nobel Prize in Physiology or Medicine.

MR is a powerful diagnostic tool. Compared to CT imaging, MR has several advantages, such as greater intrinsic soft-tissue contrast and resolution than CT and nonionizing radiation, as it uses radiofrequency waves for signal generation. In many clinical specialties, such as orthopedics, neurology, and neurosurgery, as well as for various anatomies and pathologies, including pelvic organs and tumors, soft-tissue visualization is used for diagnosis. Therefore, MR is the preferred imaging modality for many diagnostic imaging applications. Despite the wide use of MR for diagnostic imaging, in radiation therapy treatment planning MR is still a secondary image modality due to its image artifacts, lack of tissue density information, and relatively small field of view (FOV).

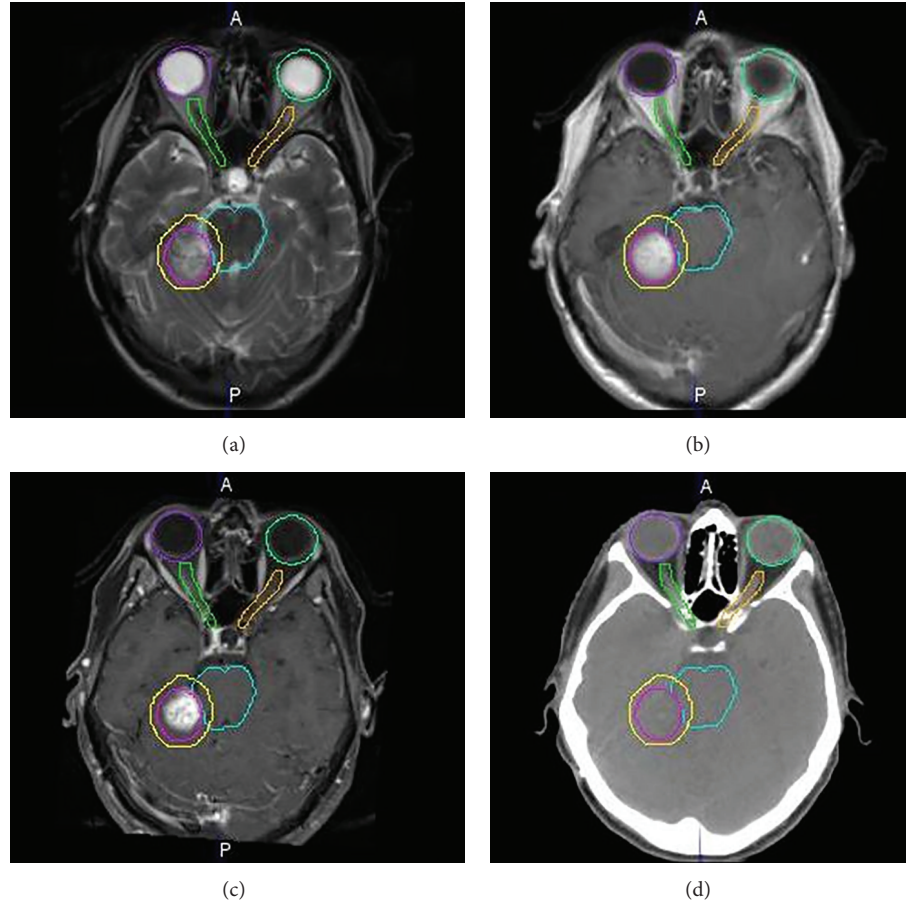


FIGURE 2: Differences in the soft-tissue contrast from four images. (a) is a T2-weighted MR image, (b) is a T1-weighted MR image, (c) is a T1-weighted MR image with contrast, and (d) is a CT image. The ROIs shown above are eyes (purple and light green colors), optical nerves (green and yellow colors), brain stem (teal color), gross tumor (pink color), and clinical target (yellow color) which extend from the gross tumor by a few millimeters with the intent of treating the subclinical microscopic extension of disease.

MR systems available only five years ago were less successful due to issues rendering them unsuitable for RT planning. However, improvements in MR hardware and software design have allowed MR imaging to become part of the RT planning workflow [18–21]. Protocols generated specifically for the purpose of RT planning rely on fundamentally robust, high-resolution, contrast-consistent, large FOV acquisitions, compared to the variety of sequences that may be used in diagnostic imaging. This effort has helped to increase the use of MR in RT planning, although still only as a secondary imaging set.

Two, significant issues keep MR relegated to a secondary role, that is, the lack of electron-density information derived from MR images and the potential error in its geometric accuracy. Regarding electron density, therapy planning entails estimating the radiation dose which depends on the manner and degree to which the radiation interacts with and deposits energy in the tissue. This occurs primarily due to Compton events in which the incident, high-energy X-rays interact with outer shell electrons in the tissue. The interaction probability is proportional to electron density,

on which the CT but not the MR signal depends. Although MR cannot directly image tissue density, there are several studies showing the potential to calculate the radiation dose and even generate DRRs based solely on MR data (Figure 5) [18, 20, 21]. A common approach is to assign a bulk density to the MR image using an atlas-based, electron-density mapping method [20, 22]. This remains an active area of research and new methods may be forthcoming.

Regarding the geometric accuracy, MR images may appear spatially warped so that the location of something appearing in the image differs from its actual physical location. This could be caused, for example, by distortions in the magnetic gradient fields. With MR, the spatial location is encoded by the spin frequency of protons which depends on the local magnetic-field strength. Magnetic gradients are used to vary the field strength in a spatially dependent manner. Spatial warping then results with aberrations in field strength that can be caused by residual error in system calibrations and by the presence of materials such as dental implants, prostheses and even due to transitions between materials, for example, between tissue and air.

TABLE 2: Sources of MR distortion, correction, and method for assessment.

Level of distortion	Distortion source	Distortion correction	Assessment of residual distortion
System	Gradient nonlinearity	Gradient coil design (HW) Model-based corrections (SW)	Geometric fidelity phantoms and assessment tools
	Static field (B0) inhomogeneity	Magnet design and static-field shims (HW)	B0-field map in phantoms
Patient	Static-field (B0) inhomogeneity	Gradient-shim coils (HW) Patient-specific B0 field correction (SW)	B0-field map in the patient
	Transmit-field (B1) inhomogeneity	Multiple RF transmit channels (HW) Patient-specific B1 field correction (SW)	B1-field map in the patient
Sequence	Gradient switching (eddy currents)	Gradient preemphasis (HW/SW) Protocols with low gradient slew rates (SW)	Visual inspection

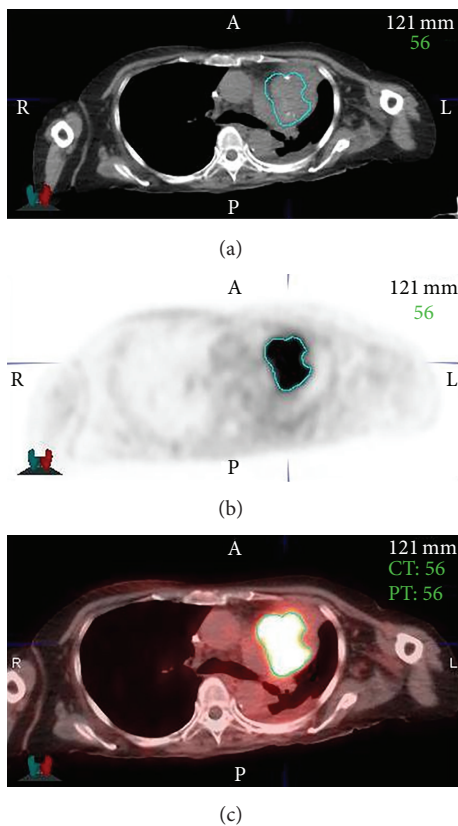


FIGURE 3: PET provides the ability to differentiate areas of neoplastic, hyper-metabolic activity within surrounding normal tissue where (a) is the CT image, (b) is the PET, and (c) is the fused PET/CT. All of the images show the gross tumor delineated from the PET image in teal color.

To mitigate these effects one can use acquisition sequences that are less sensitive to magnetic field inaccuracies. Table 2 shows the types of MR distortion, correction, and assessment. As mentioned above, current MR systems have hardware and software solutions available that optimize the geometric fidelity. Improved gradient linearity, static-field homogeneity, and patient-induced inhomogeneity compensation have brought MR greater acceptance for RT

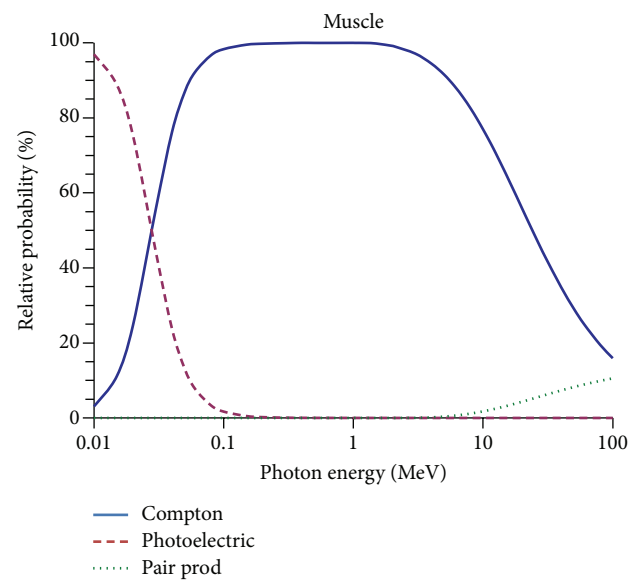


FIGURE 4: Probability of photon interaction (Compton, Photoelectric, and Pair Production) in muscle.

planning. Quality assurance tools to test various sources of image distortion can also be used to characterize these improvements on both a daily and a patient-by-patient basis. These advancements have increased the use of MR systems in radiation oncology clinical departments and have encouraged further development of MR-guided treatment solutions, including several projects intended to integrate MR imaging during external-beam radiation therapy [23–25].

**3.2. PET.** PET entails imaging the biodistribution of a radiolabeled compound selected based on its biochemical behavior. Most commonly, 2-[<sup>18</sup>F]fluoro-2-deoxy-D-glucose (FDG), a glucose analog, is used and is transported into cells, phosphorylated, and then trapped intracellularly. Differing from CT and conventional MR which show morphology, FDG-PET shows metabolically active tissue. As such, PET can be used to refine the target volume or to provide a dose boost to the most metabolically active tumors or areas therein [16]. PET can also be used to monitor tumor response, while

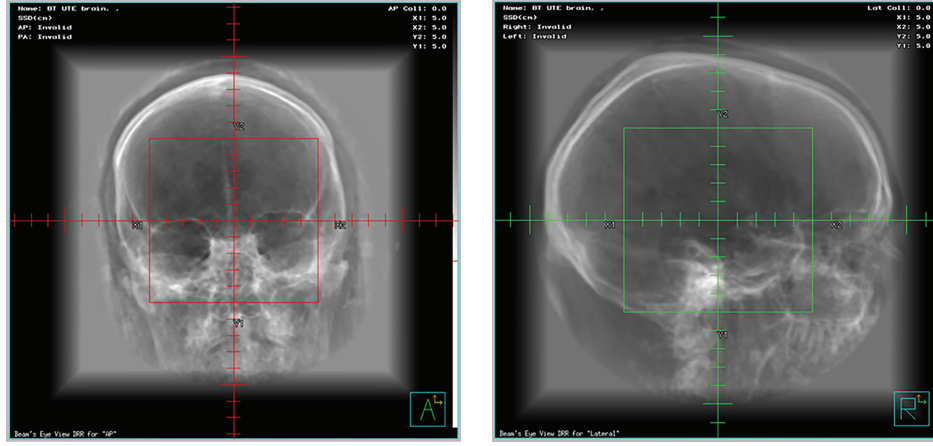


FIGURE 5: DRRs based solely on MR data.

noting that metabolic changes would precede changes in tumor shape and size [17].

While FDG is the most commonly used PET radiopharmaceutical, others may also be useful for radiation therapy. For example, some radiopharmaceuticals, such as  $^{64}\text{Cu}$ -diacetyl-bis( $\text{N}^4$ -methylthiosemicarbazone), commonly called  $^{64}\text{Cu}$ -ATSM, and  $^{18}\text{F}$ -fluoromisonidazole, commonly called  $^{18}\text{F}$ -FMISO, have been designed to demonstrate hypoxia, and as hypoxia is associated with radiation resistance, such areas may be targeted for additional radiation dosage [26].  $3'$ -[ $^{18}\text{F}$ ]fluoro- $3'$ -deoxythymidine,  $^{18}\text{F}$ -FLT has been developed as a marker of cellular proliferation and is used to assess the response to radiation therapy [27]. It has the potential to be an earlier indicator than FDG as radiation causes an inflammatory response that necessitates a delay between therapy and follow-up FDG-PET imaging [28].

Regardless of the radiotracer used, determining its spatial location is essential for radiation therapy planning. In this regard, image registration and fusion, that is, the ability to determine corresponding spatial locations in two or more image volumes and to visualize the result as a superpositioning of images, is a very useful technology. In the 1990s, image registration and fusion were achieved by scanning a patient on two, different scanners and then analyzing the data using a combination of computer software and human guidance to rotate and translate one of the two image volumes until it best matches the other. It is also possible to stretch or warp the image volumes to account for further differences in patient position and orientation, although it is less used and more prone to error than rigid-body transformations such as rotation and translation. Therefore, the advent of multimodality scanners, beginning around the year 2000, with combined PET-CT [29, 30], was a seminal advance for the use of imaging in radiation therapy planning as patients would be placed in the same position for both PET and CT. In fact, this change was so significant that the sale of PET scanners lacking CT absolutely disappeared within a few years. Motivated by the success of PET-CT, other combined instruments have been made, with PET-MR being the newest, and have the greatest number of technical challenges owing

to the difficulty of operating PET detectors in the strong magnetic field of MR [31, 32]. Despite these and other challenges, it is exciting that MR offers soft-tissue contrast that is not possible with CT and that facilitates, for example, visualization of prostate and head and neck cancer (Figure 6).

**3.3. Image Registration and Fusion.** The ability to fuse and coregister the three, main types of oncologic imaging techniques, that is, CT, MR, and PET, became available for radiation oncology planning in the early 1990s due to the improvement of the software algorithms used to register and fuse multimodality imaging datasets. Registration is the ability to align the same points from different images. In medical applications, these points are the same anatomical regions of the body, such as bone and organs, for the same patient. Fusion is the ability to display different types of registered images anatomically overlain on one another in a single, composite image [33]. Fusion provides the best information for each image, that is, geometric definition and tissue density from the CT image, soft-tissue contrast from the MR image, and metabolic information from the PET image. The combined information reduces the uncertainty regarding the tumor definition for geometric localization as well as determining the size and spread of the disease. By improving the accuracy of the target definition, image fusion can potentially improve the treatment outcome and decrease complications as less normal tissue is irradiated.

Currently, most radiation treatment planning systems support image registration and fusion. There are several fusion algorithms. The most common is geometrical transformation (rigid and nonrigid) that can be point-based, intensity-based, or based on the mechanical properties of the tissue [34]. Registration algorithms are very complex and can create undesirable image artifacts, thus causing errors in the tumor and normal tissue localization. To minimize potential issues using software-based registration, it is desirable to position patients as similarly as possible and to use the software to refine the result. This can be achieved by using immobilization devices as well as using flat tables for diagnostic imaging equipment and which match the geometry of the

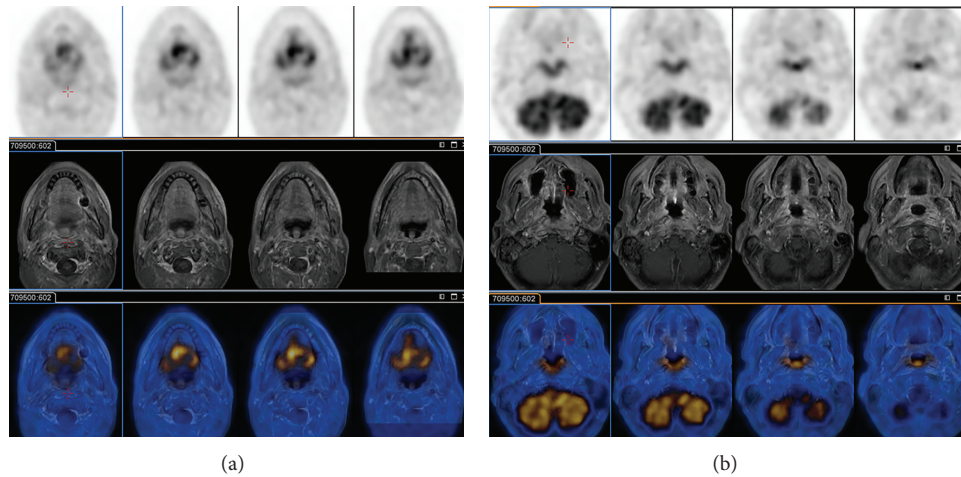


FIGURE 6: Axial-view images of a patient using a combined PET/MR scanner. The upper rows show PET images of FDG activity corresponding to glucose metabolism. The middle rows show MR images acquired using a T1-weighted, fat saturation sequence. The lower rows show the fused images. The PET images show elevated FDG uptake indicating cancer in (a), the tongue base and (b) the epiglottis.

treatment couch. As a patient's body may still move between and during the image set acquisitions, a 3-dimensional registration is necessary. Keeping the patient immobilized in the image set will produce smaller corrections for the fusion algorithm, thus causing fewer registration errors. Currently, the process of fusing multiple image techniques in radiation oncology is labor-intensive and requires manual verification of the quality of the registration by qualified experts [35]. Automation of this process will depend on improvements in the algorithms as well as better metrics for accuracy verification.

#### 4. Future Considerations

The primary goal of treatment planning is to precisely calculate the radiation dose to the tumor in order to improve the outcome and reduce toxicity. The future of imaging in radiation therapy treatment planning is promising, and other advances will contribute to better target definition. Higher resolution imaging will be developed for all of the modalities discussed. Specifically, higher definition PET-CT scanners and high magnetic field MR have the ability to improve the visualization of tumors even to the level of microscopic disease extension [6].

Emerging algorithms for image fusion [33] will be more accurate and will allow an automated fusion process and verification. These new algorithms will make the tumor localization in the several types of images more precise and less time-consuming.

As previously mentioned, several solutions have been introduced in order to allow MR-based simulation and planning to become a reality. This may ultimately lead to the elimination of CT in radiation therapy, and which has been the foundation of treatment planning during the past four decades. This has far-reaching implications including lower overall cost and reduced X-ray exposure. However, another issue that has slowed the adoption of MR by radiation

oncology is the lack of staff training for MR imaging and explaining the use of MR for treatment planning during traditional professional education.

Once MR systems are readily available for imaging patients undergoing radiation treatment, the opportunity to assess their response to treatment and to adapt the treatment plan for improved patient outcomes is likely [36–41]. The number and types of functional measurements which can be determined using MR imaging are multiple. Table 3 shows some of the basic, functional imaging types that have shown promise in predicting the clinical outcomes for various tumor types.

**4.1. “Omics” and the Future.** Several investigators are attempting to apply the field of “omics” to tailor individual treatment for a better outcome in cancer therapy through the expression of genes, proteins, and metabolites. In radiation therapy “omics” may be able to predict the treatment response through immunohistochemical markers, DNA microarray gene signatures, and nucleotide polymorphisms [42]. Identifying biomarkers that can predict the sensitivity or resistance of tumors to radiation therapy is another promising area of ongoing research [43].

The advances in omics imaging for radiation treatment planning will include molecular imaging such as the new MR sequences described in Table 3, functional imaging, as well as the development and application of new PET tracers, such as <sup>18</sup>F-FLT, <sup>64</sup>Cu-ATSM, and <sup>18</sup>F-FMISO, that can better identify regions of hypoxia, oxygen metabolism, microscopic disease, and high metabolism inside the tumor [27]. Tumor genetic and radiobiological factors will guide individualized radiation therapy with better target delineation, avoidance of normal tissue, dose escalation, dose fractionation, and better prediction of treatment response [44]. The semiquantitative, standardized uptake value (SUV) with different radiotracers for different tumor histologies will be able to predict the tumor heterogeneity based on metabolism. The SUV can

TABLE 3: Basic MR functional imaging types that have shown promise in predicting outcomes for various tumor types.

Type of measurement	Functional imaging method	Known as	What is measured
Perfusion	Dynamic contrast enhanced	DCE, permeability	Gadolinium-induced shortening of T1
	Dynamic susceptibility contrast	DSC	Gadolinium-induced shortening of T2*
	Arterial spin labeling	ASL	Intrinsic contrast enhancement generated from magnetization of arterial blood
Diffusion	Diffusion weighting imaging	DWI	Gradient-induced sensitization of molecular diffusion
Metabolic function	Spectroscopy	MRSI	Chemical composition based on resonant frequency
Oxygenation	BOLD-level oxygen dependent	BOLD, fMRI	T2* differences in oxy- and deoxyhemoglobin

identify more aggressive (metabolically active) or radioresistant (hypoxic) areas within a tumor and allow these areas to be treated with higher radiation doses (dose painting) [44].

In the omics era, therapy may be personally optimized based on pathologic and genetic characterization of tumors in order to target the relevant treatment pathways while minimizing undesirable side effects [45]. In both the past and present, detailed characterization requires biopsy. However, biopsy is invasive and only provides a snapshot of a subset of the cells of interest. As tumors are often heterogeneous, there may be multiple regions in a tumor, each with its own genetic profile. Tumors may be near nerves or other critical structures that make needle placement unacceptably risky. Molecular imaging has the promise to overcome these pitfalls while providing key insight regarding the tumor genetics, active pathways, and sensitivity to radiation, all as a spatial map which can be used to target a constellation of tumors and even regions within tumors [46].

In conclusion, the future of image-guided treatment planning is boundless and with continuous innovations that will ultimately lead to higher cure rates and less treatment-associated toxicity.

## Conflict of Interests

The authors declare that they have no conflict of interests regarding the publication of this paper.

## Acknowledgments

The authors thank David Mansur, M.D., for review of the paper and Bonnie Hami, M.A. (USA), for her editorial assistance in the preparation of the paper.

## References

- [1] R. E. Pollock and D. L. Morton, "Principles of surgical oncology," in *Cancer Medicine*, D. W. Kufe and R. E. Pollock, Eds., B. C. Decker, Hamilton, Ontario, Canada, 2000.
- [2] V. T. de Vita Jr. and E. Chu, "A history of cancer chemotherapy," *Cancer Research*, vol. 68, no. 21, pp. 8643–8653, 2008.
- [3] F. M. Khan, "Clinical radiation generators," in *The Physics of Radiation Therapy*, Lippincott Williams & Wilkins, Philadelphia, Pa, USA, 2010.
- [4] T. Bortfeld and R. Jeraj, "The physical basis and future of radiation therapy," *British Journal of Radiology*, vol. 84, no. 1002, pp. 485–498, 2011.
- [5] D. Vordermark, "Ten years of progress in radiation oncology," *BMC Cancer*, vol. 11, article 503, 2011.
- [6] W. Schlegel, "If you can't see it, you can miss it: the role of biomedical imaging in radiation oncology," *Radiation Protection Dosimetry*, vol. 139, no. 1–3, pp. 321–326, 2010.
- [7] P. H. Ahn and M. K. Garg, "Positron emission tomography/computed tomography for target delineation in head and neck cancers," *Seminars in Nuclear Medicine*, vol. 38, no. 2, pp. 141–148, 2008.
- [8] D. Mak, J. Corry, E. Lau, D. Rischin, and R. J. Hicks, "Role of FDG-PET/CT in staging and follow-up of head and neck squamous cell carcinoma," *Quarterly Journal of Nuclear Medicine and Molecular Imaging*, vol. 55, no. 5, pp. 487–499, 2011.
- [9] D. R. Simpson, J. D. Lawson, S. K. Nath, B. S. Rose, A. J. Mundt, and L. K. Mell, "Utilization of advanced imaging technologies for target delineation in radiation oncology," *Journal of the American College of Radiology*, vol. 6, no. 12, pp. 876–883, 2009.
- [10] E. Glatstein, A. S. Lichter, and B. A. Fraass, "The imaging revolution and radiation oncology: use of CT, ultrasound, and NMR for localization, treatment planning and treatment delivery," *International Journal of Radiation Oncology Biology Physics*, vol. 11, no. 2, pp. 299–314, 1985.
- [11] A.-L. Grosu, M. Pier, W. A. Weber et al., "Positron emission tomography for radiation treatment planning," *Strahlentherapie und Onkologie*, vol. 181, no. 8, pp. 483–499, 2005.
- [12] K. U. Hunter and A. Eisbruch, "Advances in imaging: target delineation," *Cancer Journal*, vol. 17, no. 3, pp. 151–154, 2011.
- [13] N. Papanikolaou, J. J. Battista, A. L. Boyer et al., "Tissue inhomogeneity corrections for megavoltage photon beams," in *Report of Task Group 65*, pp. 1–142, American Association of Physics in Medicine, 2004.
- [14] P. Keall, "4-dimensional computed tomography imaging and treatment planning," *Seminars in Radiation Oncology*, vol. 14, no. 1, pp. 81–90, 2004.

- [15] R. J. H. M. Steenbakkers, J. C. Duppen, I. Fitton et al., "Reduction of observer variation using matched CT-PET for lung cancer delineation: a three-dimensional analysis," *International Journal of Radiation Oncology Biology Physics*, vol. 64, no. 2, pp. 435–448, 2006.
- [16] J. Li and Y. Xiao, "Application of FDG-PET/CT in radiation oncology," *Frontiers in Oncology*, vol. 3, pp. 1–6, 2013.
- [17] V. Grégoire, K. Haustermans, X. Geets, S. Roels, and M. Lonneux, "PET-based treatment planning in radiotherapy: a new standard?" *Journal of Nuclear Medicine*, vol. 48, no. 1, pp. 68S–77S, 2007.
- [18] E. M. Kerkhof, J. M. Balter, K. Vineberg, and B. W. Raaymakers, "Treatment plan adaptation for MRI-guided radiotherapy using solely MRI data: a CT-based simulation study," *Physics in Medicine and Biology*, vol. 55, no. 16, pp. N433–N440, 2010.
- [19] K. L. Maletz, R. D. Ennis, J. Ostenson, A. Pevsner, A. Kagen, and I. Wernick, "Comparison of CT and MR-CT fusion for prostate post-implant dosimetry," *International Journal of Radiation Oncology Biology Physics*, vol. 82, no. 5, pp. 1912–1917, 2012.
- [20] J. A. Dowling, J. Lambert, J. Parker et al., "An atlas-based electron density mapping method for magnetic resonance imaging (MRI)—alone treatment planning and adaptive MRI-based prostate radiation therapy," *International Journal of Radiation Oncology Biology Physics*, vol. 83, no. 1, pp. e5–e11, 2012.
- [21] M. Kapanen, J. Collan, A. Beule, T. Seppälä, K. Saarilahti, and M. Tenhunen, "Commissioning of MRI-only based treatment planning procedure for external beam radiotherapy of prostate," *Magnetic Resonance in Medicine*, vol. 70, no. 1, pp. 127–135, 2013.
- [22] J. H. Jonsson, M. G. Karlsson, M. Karlsson, and T. Nyholm, "Treatment planning using MRI data: an analysis of the dose calculation accuracy for different treatment regions," *Radiation Oncology*, vol. 5, no. 1, article 62, 2010.
- [23] B. G. Fallone, B. Murray, S. Rathee et al., "First MR images obtained during megavoltage photon irradiation from a prototype integrated linac-MR system," *Medical Physics*, vol. 36, no. 6, pp. 2084–2088, 2009.
- [24] B. W. Raaymakers, J. J. W. Lagendijk, J. Overweg et al., "Integrating a 1.5 T MRI scanner with a 6 MV accelerator: proof of concept," *Physics in Medicine and Biology*, vol. 54, no. 12, pp. N229–N237, 2009.
- [25] J. Dempsey, "WE-E-ValA-06: a real-time MRI guided external beam radiotherapy delivery system," *Medical Physics*, vol. 33, no. 6, pp. 2254–2254, 2006.
- [26] M. M. Clausen, "Dose escalation to high-risk sub-volumes based on non-invasive imaging of hypoxia and glycolytic activity in canine solid tumors: a feasibility study," *Radiation Oncology*, vol. 8, article 262, 2013.
- [27] B. J. Allen, E. Bezak, and L. G. Marcu, "Quo Vadis radiotherapy? Technological advances and the rising problems in cancer management," *BioMed Research International*, vol. 2013, Article ID 749203, 9 pages, 2013.
- [28] S. Chandrasekaran, "18F-fluorothymidine-pet imaging of glioblastoma multiforme: effects of radiation therapy on radiotracer uptake and molecular biomarker patterns," *The Scientific World Journal*, vol. 2013, Article ID 796029, 12 pages, 2013.
- [29] T. Beyer, D. W. Townsend, T. Brun et al., "A combined PET/CT scanner for clinical oncology," *Journal of Nuclear Medicine*, vol. 41, no. 8, pp. 1369–1379, 2000.
- [30] D. Thorwarth, X. Geets, and M. Paiusco, "Physical radiotherapy treatment planning based on functional PET/CT data," *Radiotherapy and Oncology*, vol. 96, no. 3, pp. 317–324, 2010.
- [31] H. Herzog and J. van den Hoff, "Combined PET/MR systems: an overview and comparison of currently available options," *Quarterly Journal of Nuclear Medicine and Molecular Imaging*, vol. 56, no. 3, pp. 247–267, 2012.
- [32] B. J. Pichler, M. S. Judenhofer, and C. Pfannenberg, "Multimodal imaging approaches: PET/CT and PET/MRI," *Handbook of Experimental Pharmacology*, no. 185, pp. 109–132, 2008.
- [33] A. Ardesir Goshtasby and S. Nikolov, "Image fusion: advances in the state of the art," *Information Fusion*, vol. 8, no. 2, pp. 114–118, 2007.
- [34] J. M. Fitzpatrick, D. L. G. Hill, and C. R. Maurer, "Image registration," in *Handbook of Medical Imaging*, M. Sonka and J. M. Fitzpatrick, Eds., SPIE Press, 2009.
- [35] M. L. Kessler, "Image registration and data fusion in radiation therapy," *British Journal of Radiology*, vol. 79, pp. S99–S108, 2006.
- [36] B. A. Moffat, T. L. Chenevert, T. S. Lawrence et al., "Functional diffusion map: a noninvasive MRI biomarker for early stratification of clinical brain tumor response," *Proceedings of the National Academy of Sciences of the United States of America*, vol. 102, no. 15, pp. 5524–5529, 2005.
- [37] J.M. Lupo, E. Essock-Burns, A. M. Molinaro et al., "Using susceptibility-weighted imaging to determine response to combined anti-angiogenic, cytotoxic, and radiation therapy in patients with glioblastoma multiforme," *Neuro-Oncology*, vol. 15, no. 4, pp. 480–489, 2013.
- [38] Y. Cao, "The promise of dynamic contrast-enhanced imaging in radiation therapy," *Seminars in Radiation Oncology*, vol. 21, no. 2, pp. 147–156, 2011.
- [39] A. R. Padhani and K. A. Miles, "Multiparametric imaging of tumor response to therapy," *Radiology*, vol. 256, no. 2, pp. 348–364, 2010.
- [40] A. R. Padhani, G. Liu, D. Mu-Koh et al., "Diffusion-weighted magnetic resonance imaging as a cancer biomarker: consensus and recommendations," *Neoplasia*, vol. 11, no. 2, pp. 102–125, 2009.
- [41] J. E. Bayouth, T. L. Casavant, M. M. Graham, M. Sonka, M. Muruganandham, and J. M. Buatti, "Image-based biomarkers in clinical practice," *Seminars in Radiation Oncology*, vol. 21, no. 2, pp. 157–166, 2011.
- [42] S. M. Bentzen, "From cellular to high-throughput predictive assays in radiation oncology: challenges and opportunities," *Seminars in Radiation Oncology*, vol. 18, no. 2, pp. 75–88, 2008.
- [43] C. H. Chung, S. Wong, K. K. Ang et al., "Strategic plans to promote head and neck cancer translational research within the radiation therapy oncology group: a report from the translational research program," *International Journal of Radiation Oncology Biology Physics*, vol. 69, no. 2, pp. S67–S78, 2007.
- [44] A. Basu, "The scope and potentials of functional radionuclide imaging towards advancing personalized medicine in oncology: emphasis on PET-CT," *Discovery Medicine*, vol. 13, no. 68, pp. 65–73, 2012.
- [45] H. Schoder and S. C. Ong, "Role of positron emission tomography in radiation oncology," *Seminars in Nuclear Medicine*, vol. 38, no. 2, pp. 119–128, 2008.
- [46] S. A. Amundson, M. Bittner, and A. J. Fornace Jr., "Functional genomics as a window on radiation stress signaling," *Oncogene*, vol. 22, no. 37, pp. 5828–5833, 2003.

## Research Article

# Development and Evaluation of an Open-Source Software Package “CGITA” for Quantifying Tumor Heterogeneity with Molecular Images

Yu-Hua Dean Fang,<sup>1,2</sup> Chien-Yu Lin,<sup>3,4</sup> Meng-Jung Shih,<sup>5</sup> Hung-Ming Wang,<sup>4,6</sup> Tsung-Ying Ho,<sup>4,7</sup> Chun-Ta Liao,<sup>4,8</sup> and Tzu-Chen Yen<sup>2,4,7</sup>

<sup>1</sup> Department of Electrical Engineering, College of Engineering, Chang Gung University, Taoyuan 333, Taiwan

<sup>2</sup> Molecular Imaging Center, Chang Gung Memorial Hospital, Linkou, Taiwan

<sup>3</sup> Department of Radiation Oncology, Chang Gung Memorial Hospital, Linkou, Taiwan

<sup>4</sup> Head and Neck Oncology Group, Chang Gung Memorial Hospital and Chang Gung University, Taoyuan 333, Taiwan

<sup>5</sup> Advanced Research Institute, Institute for Information Industry, Taipei, Taiwan

<sup>6</sup> Medical Oncology, Chang Gung Memorial Hospital, Linkou, Taiwan

<sup>7</sup> Department of Nuclear Medicine, Chang Gung Memorial Hospital, No. 5 Fu-Hsin Street, Kwei-Shan, Taoyuan 333, Taiwan

<sup>8</sup> Otorhinolaryngology, Head and Neck Surgery, Chang Gung Memorial Hospital, Linkou, Taoyuan 333, Taiwan

Correspondence should be addressed to Tzu-Chen Yen; [yentc1110@gmail.com](mailto:yentc1110@gmail.com)

Received 18 October 2013; Revised 1 February 2014; Accepted 5 February 2014; Published 17 March 2014

Academic Editor: Dimitris Visvikis

Copyright © 2014 Yu-Hua Dean Fang et al. This is an open access article distributed under the Creative Commons Attribution License, which permits unrestricted use, distribution, and reproduction in any medium, provided the original work is properly cited.

**Background.** The quantification of tumor heterogeneity with molecular images, by analyzing the local or global variation in the spatial arrangements of pixel intensity with texture analysis, possesses a great clinical potential for treatment planning and prognosis. To address the lack of available software for computing the tumor heterogeneity on the public domain, we develop a software package, namely, Chang-Gung Image Texture Analysis (CGITA) toolbox, and provide it to the research community as a free, open-source project. **Methods.** With a user-friendly graphical interface, CGITA provides users with an easy way to compute more than seventy heterogeneity indices. To test and demonstrate the usefulness of CGITA, we used a small cohort of eighteen locally advanced oral cavity (ORC) cancer patients treated with definitive radiotherapies. **Results.** In our case study of ORC data, we found that more than ten of the current implemented heterogeneity indices outperformed  $SUV_{mean}$  for outcome prediction in the ROC analysis with a higher area under curve (AUC). Heterogeneity indices provide a better area under the curve up to 0.9 than the  $SUV_{mean}$  and TLG (0.6 and 0.52, resp.). **Conclusions.** CGITA is a free and open-source software package to quantify tumor heterogeneity from molecular images. CGITA is available for free for academic use at <http://code.google.com/p/cgita>.

## 1. Background

Molecular imaging has become a significant component of patient management in clinical oncology. The importance of extracting quantitative measurements from molecular images has been widely embraced. Recently, there is an increasing interest to quantify the “tumor heterogeneity” from molecular images, especially, PET, as the tumor heterogeneity is an important biomarker for aggressiveness and disease outcome [1–3]. The computation of tumor heterogeneity can be related to texture analysis that refers to

numerous mathematical methods to compute quantitative textural features from 2D or 3D images based on the spatial variation of pixel intensity. To properly address the nature of quantification goals of this study, we use the term “heterogeneity index” to denote the calculated tumor heterogeneity in a numerical form. Although there is an emerging enthusiasm in quantification of tumor heterogeneity [4–13], such techniques remain to be evaluated and tested for clinical applications [13].

One existing challenge for investigators interested in testing the usefulness of heterogeneity indices lies in the

lack of software available on the public domain. Because texture analysis is a relatively new concept for PET and nuclear medicine community, most software packages offered by vendors do not include functions for such analysis. Commercial third-party software also lacks these functions in general. To address these challenges, we implemented a software package for computing tumor heterogeneity indices and share it with the research community of molecular imaging. This report aims to describe this open-source project of our software package, namely, Chang-Gung Image Texture Analysis (CGITA) toolbox, for quantifying tumor heterogeneity. We will describe its implementation, data flow, and currently supported functions. To evaluate the usefulness of CGITA, we used a cohort of eighteen advanced oral cavity (ORC) cancer patients that were treated with definitive radiotherapy to demonstrate the use of tumor heterogeneity as a biomarker of prognosis assisted by CGITA.

## 2. Methods and Materials

**2.1. Tumor-Wise and Voxel-Wise Heterogeneity Quantification.** The calculation of tumor heterogeneity is implemented in CGITA with two different levels: tumor-wise and voxel-wise heterogeneity. For the former level that generates heterogeneity indices based on the whole delineated tumor, we used the same processing scheme described by Tixier et al. [10]. In brief, a tumor or target volume of tissue is first delineated from the image volume either manually or with automatic segmentation. The intensities of delineated voxels are then redigitized and carried into the mathematical transformation to compute the heterogeneity indices. The second level, on the other hand, computes the heterogeneity indices on a voxel-wise basis. The intensities of surrounding voxels around a specific voxel are used to calculate the heterogeneity indices for this voxel. By repeating the same computation for each voxel, a parametric map can be formed to represent the heterogeneity distribution.

**2.2. Implementation of CGITA.** CGITA was implemented in MATLAB (version 2012a, MathWorks Inc., Natick, MA, USA). It is now distributed over the Internet as an open-source project with two forms of program distribution. For users with a MATLAB license, the MATLAB codes of CGITA are available for them to download, use, and even modify. CGITA is supported and tested on the Windows and Linux platforms. For users without a MATLAB license, a stand-alone CGITA executable is available, although this version does not support the user-defined functions in general. All CGITA functions were implemented in native MATLAB without using compiled C++ functions or MEX files so that cross-platform support can be maximized. The only exception is the dependence of some executable functions in DCMTK [14] on DICOM query and retrieval.

**2.3. Tumor Delineation.** CGITA allows two types of tumor delineation. First, CGITA accepts the volume of interest (VOI) saved as DICOM-RT structures or the VOI drawn and saved with PMOD (PMOD Technologies Ltd, Zurich,

Switzerland). Second, the user may use our semiautomatic segmentation functions to delineate the tumor. Currently, the built-in segmentation in CGITA includes a threshold-based region-growing method and a fuzzy C-means method. CGITA allows users to add new segmentation methods as well.

**2.4. Computational Methods for Whole-Tumor Heterogeneity Indices.** We begin by defining what a “heterogeneity index” is. Since the term “heterogeneity” is a general description of mixed composition within an object, there is not a single or specific mathematical definition of heterogeneity. This is why we chose to use the term “heterogeneity index.” Each heterogeneity index indicates the degree of heterogeneity. However, the exact way for computing its value varies from index to index. From the texture analysis point of view, each heterogeneity index is represented by a “textural feature.” We use the term “heterogeneity index” instead of “textural feature” to specifically describe the biological parameter of a tumor that we wish to quantify.

The computation of tumor heterogeneity indices is performed in two steps: the computation of a “parent” matrix and the parameter extraction from this parent matrix. The “parent matrix” refers to a matrix obtained by a numerical transformation that accounts for the spatial arrangement, intensity, and relationship of the voxels contained within the VOI. We have implemented the four parent matrices described in the study by Tixier et al. [10]. We also included an additional four parent matrices: the texture spectrum matrix [15], texture feature coding matrix [16], texture feature coding cooccurrence matrix [16, 17], and neighborhood gray-level dependence matrix [18]. For each of those eight parent matrices, a variable number of heterogeneity indices are calculated. Table 1 summarizes the currently supported indices in CGITA and their references. At present, there are a total of 72 heterogeneity indices included in CGITA. These heterogeneity indices, in brief, all point to the degree of spatial nonuniformity that directly correlates with tumor heterogeneity in tracer uptake. The difference between individual indices lies in the mathematical computation. For example, the indices computed with voxel-alignment matrix are related to the length of “run,” which is defined as the length of voxels aligned on a line that have the same pixel intensity. Among those indices, for example, the heterogeneity index “long-run emphasis” puts a stronger weighting on the intensities of voxels with long runs. Such an index can be used to measure the tumor heterogeneity by examining the voxels that have the similar tracer uptake and align along the same line.

Some conventional image-derived indices, such as  $SUV_{mean}$ ,  $SUV_{max}$ ,  $SUL_{peak}$  [23], and total lesion glycolysis (TLG), are included in these indices based on literatures [10].

**2.5. Software Validation.** The software validation is performed in two different levels. First, we validate the computation of heterogeneity indices against other software packages. Since we do not have access to other in-house software packages for computing the tumor heterogeneity, we are only able to validate some of the conventional indices such

TABLE 1: Summary of the currently supported heterogeneity indices of CGITA.

Parent matrix	Feature measure
Cooccurrence matrix [17]	Second angular moment, contrast, entropy, homogeneity, dissimilarity, inverse difference moment
Voxel-alignment matrix [19]	Short-run emphasis, long-run emphasis, intensity variability, run-length variability, run percentage, low-intensity run emphasis, high-intensity run emphasis, low-intensity short-run emphasis, high-intensity short-run emphasis, low-intensity long-run emphasis, high-intensity long-run emphasis
Neighborhood intensity difference matrix [20]	Coarseness, contrast, busyness, complexity, strength
Intensity size-zone matrix [21]	Short-zone emphasis, large-zone emphasis, intensity variability, size-zone variability, zone percentage, low-intensity zone emphasis, high-intensity zone emphasis, low-intensity short-zone emphasis, high-intensity short-zone emphasis, low-intensity large-zone emphasis, high-intensity large-zone emphasis
Normalized cooccurrence matrix [17]	Second angular moment, contrast, entropy, homogeneity, inverse difference moment, dissimilarity, correlation
Voxel statistics	Minimum SUV, maximum SUV, mean SUV, SUV variance, SUV SD, SUV skewness, SUV kurtosis, SUV skewness (bias corrected), SUV kurtosis (bias corrected), TLG, tumor volume, entropy, SUL <sub>peak</sub>
Texture spectrum [15]	Max spectrum, Black-white symmetry
Texture feature coding [16]	Coarseness, homogeneity, mean convergence
Texture feature coding cooccurrence matrix [16]	Second angular moment, contrast, entropy, homogeneity, intensity, inverse difference moment, correlation, variance, code similarity
Neighborhood gray-level dependence [22]	Small-number emphasis, large-number emphasis, number nonuniformity, second moment, entropy

as SUV<sub>mean</sub> and TLG against commercial software PMOD. Tested with clinical PET images, CGITA is able to obtain nearly identical results as PMOD for SUV<sub>mean</sub> and TLG. The second level of software validation is the software reliability after each update and revision. In order to ensure the software quality, each time a function is added or modified, a set of clinical PET images and its corresponding VOI are kept internally for testing CGITA. Computed heterogeneity indices are generated and compared to historical results, in order to check if the computation remains consistent after software update.

**2.6. Parametric Imaging.** For a given image volume, the parametric image of heterogeneity indices is computed by looping through every voxel and repeating the following steps for each voxel. The user must first choose how many voxels should be used to calculate the parametric image. For example, the user may elect to use a  $3 \times 3 \times 3$  cube centered at a specific voxel. The choice of cube size would affect the sharpness of the resulted heterogeneity parametric images. A larger cube size includes more voxels for analysis, potentially improving the heterogeneity accuracy but decreasing the spatial resolution. For a  $3 \times 3 \times 3$  cube, the intensities of those twenty-seven voxels are then treated as a delineated volume that is carried into the computation of heterogeneity indices as described in the previous sections. As a result, a heterogeneity index will be computed for the specified heterogeneity index at this given voxel. By looping through all of the voxels, except for those on the edges, a parametric image volume can be formed with the voxel-wise heterogeneity indices.

**2.7. Evaluation of Heterogeneity Indices for Outcome Prediction in Oral Cavity Cancer Patients.** We evaluated the heterogeneity indices implemented in CGITA with patient data from a cohort of ORC patients treated with definitive radiotherapy. These patients are a subgroup of a prospective dose-painting trial, approved by the Institutional Review Board of Chang-Gung Memorial Hospital. This study was conducted in the Linkou and Keelung branches of Chang-Gung Memorial Hospital, from January 2008 to December 2009. A total of 38 nonmetastatic, stage IV ORC patients who were ineligible for radical surgery were included. Informed consent was obtained from every participating subject. Simultaneous integrated boost, intensity-modulated radiation therapy (SIB-IMRT) was used to escalate the irradiation dose within gross tumor volumes to test the treatment efficacy and toxicity. For the quantitative analysis of tumor heterogeneity, we retrieved a uniform treatment group ( $n = 18$ ) who received neoadjuvant chemotherapy followed by concurrent chemoradiation. The group was comprised of 17 males (94.4%) and one female (5.6%), with a median age of 54.2 years (range: 35.9–73.4 years) and a mean age of  $53 \pm 10.5$  years. Most patients had the habits of smoking ( $n = 14$ , 77.8%), drinking ( $n = 16$ , 88.9%), and betel-quid chewing ( $n = 16$ , 88.9%). The preliminary observation was completed in June 2012, and the median follow-up times for all patients were 19.3 months (range: 4.3–50.7) and 38.1 months (range: 30.1–50.7) for survivors. A successful outcome was defined as a state free of disease progression for at least 30 months. Eighteen patients were ultimately classified into the successful group ( $n = 9$ ) and the failed group ( $n = 9$ ). In the successful



FIGURE 1: A screen shot of the CGITA program. The CGITA GUI provides users with a simple image display interface that allows users to examine different slices and views. The computation of heterogeneity indices is achieved simply by button clicking. As an open-source project, the current functions and interfaces of CGITA can be customized by users familiar with MATLAB programming. The screen shot here shows a subject with the FDG-PET images fused over CT images.

group, 8 lived without evidence of recurrence, but one died of nondisease-related causes at 16 months after completion of treatment. All other deceased patients died of disease-related events. The pretreatment PET images of all eighteen subjects were used for image analysis.

Each patient in our cohort received a pretreatment FDG-PET/CT scan for staging. Those pretreatment PET/CT scans provided the image sets with which we tested the texture analysis. Fifty minutes after the 370-MBq FDG injection, a whole-body static PET emission scan was acquired on a GE Discovery ST 16 PET/CT (GE Healthcare, Milwaukee, WI) [24] from the skull base to the mid-thigh, with three minutes per bed position. Images were reconstructed with OSEM (ten subsets, four iterations) with pixel spacing of 4.7 mm and 3.3 mm in the transverse and axial directions, respectively. Quantification of the tumor heterogeneity with PET images was performed as follows. First, the tumor contour is delineated by a board-certified nuclear physician in PMOD with a scheme similar to that of the previously reported head and neck tumor delineation [25]. We elected to draw the VOI semiautomatically, since automatic segmentation in ORC patients is generally difficult because some surrounding oral tissues are benign but show a high FDG uptake. After the lesion was first manually outlined from the fused PET/CT images by the nuclear physician, this outlined lesion area was then reviewed to remove benign tissues with high FDG uptake. Once the lesion was outlined, an SUV value of 2.5 was used to delineate the outer contour of the main tumor. Image intensities of the delineated voxels are then used to calculate heterogeneity indices and saved for each patient. Parametric images of heterogeneity indices were calculated for selected subjects.

**2.8. Performance Evaluation.** After the tumor-wise heterogeneity indices were calculated for every subject, the subjects were divided into two groups based on their outcome, with  $n = 9$  in each group. A receiver operative characteristics (ROC) curve was plotted for each heterogeneity index independently. We calculated the area under the curve (AUC) from the ROC curves and the optimal sensitivity/specificity for each index. In addition, a Kruskal-Wallis test was performed for each index to evaluate the performance of these metrics [26]. The AUC and the  $P$  value of the Kruskal-Wallis test calculated from the average intratumor SUV ( $SUV_{mean}$ ) were compared to the AUC and  $P$  value calculated from each of the other indices.

### 3. Results

The appearance of CGITA is shown with a screen shot in Figure 1. Through a graphical user interface (GUI), CGITA's image display interface can be used to view the images and confirm whether the imported VOI aligns properly with the target tissue after importing images and VOIs. Table 2 summarizes the currently implemented heterogeneity indices in CGITA. The calculated indices, currently totaling 72, can be exported as spreadsheets. In addition to processing one subject at a time using the CGITA GUI, the user may also elect to use the batch mode by processing all subjects automatically without the user input. We tested the batch function on our ORC patient data. On average, each subject takes approximately 30 seconds to process, including image importation and the computation of all 72 features. CGITA is currently hosted at <http://code.google.com/p/cgita> with

TABLE 2: Summary of the software features of CGITA.

Feature	CGITA implementation
Programming environment	MATLAB (MathWorks Inc.)
License	Free for academic use
Source code availability	Open source
Supported image format	DICOM (either local files or direct access to a PACS server for image retrieval)
Supported VOI format	DICOM-RT, PMOD
Currently supported textural features	72 (i) Parametric imaging of heterogeneity indices (ii) Batch mode for processing a large cohort (iii) Compiled stand-alone application available (iv) Supporting user-defined functions for heterogeneity calculation
Other features	

TABLE 3: Comparison of AUC, specificity, and sensitivity of heterogeneity indices vs.  $SUV_{mean}$  and TLG.

Parent	Feature	AUC	Sensitivity (%)	Specificity (%)	P value <sup>†</sup>
Intensity-size-zone	Low-intensity short-zone emphasis	0.90*	77.8	88.9	0.004
Intensity-size-zone	Short-zone emphasis	0.81*	77.8	66.7	0.024
Texture Feature Coding Cooccurrence	Contrast	0.72	55.6	88.9	0.085
Intensity-size-zone	High-intensity zone emphasis	0.70	66.7	77.8	0.145
Intensity-size-zone	Zone percentage	0.70	55.6	88.9	0.122
SUV statistics	Entropy	0.70	66.7	77.8	0.145
SUV statistics	Mean SUV	0.60	66.7	66.7	0.453
SUV statistics	Maximum SUV	0.57	66.7	66.7	0.627
SUV statistics	TLG	0.52	55.6	66.7	0.895

\* denotes that the P value is less than 0.05 given the null hypothesis of AUC < 0.5.

<sup>†</sup> calculated using the Kruskal-Wallis test (19 indices have a P value greater than 0.453).

both the source code and executables available for download. There is also a user manual for CGITA available at its website. Academic research uses are free of charge. As the hosting service also provides a version control system, users may also participate in this open-source project as developers to contribute new functions to CGITA.

The usefulness of heterogeneity quantification was evaluated with our ORC patient cohort. In terms of outcome prediction, the AUC from ROC analysis was calculated for each heterogeneity index, as was the P value for the Kruskal-Wallis test. Out of the total 72 textural features implemented in CGITA, we found that 13 textural features have a higher AUC and 19 have a lower P value than the  $SUV_{mean}$ . The heterogeneity indices with the highest AUC are summarized in Table 3 and compared to conventional markers such as  $SUV_{mean}$  and TLG. The conventional markers did not provide satisfactory discriminative power with low AUC (0.6 for  $SUV_{mean}$  and 0.52 for TLG) and high P value under the Kruskal-Wallis test. On the other hand, some heterogeneity indices stood out as better indicators for prognosis under the current tests. Two indices computed from the intensity-size-zone matrix (ISZ) [21], low-intensity short-zone emphasis (ISZ-LISZE), and short-zone emphasis (ISZ-SZE) showed high AUC (0.9 and 0.81, resp.) and low P values (0.004 and 0.024, resp.). Compared to the  $SUV_{mean}$ , LISZE improved

the sensitivity and specificity by 11% and 22%, respectively. Including ISZ-LISZE and ISZ-SZE, six indices computed from the intensity-size-zone matrix provided an AUC over 0.7. The ROC curves of ISZ-LISZE and ISZ-SZE are plotted in Figure 2 along with the ROC curves of  $SUV_{mean}$  and TLG. Parametric images based on the textural features of one subject are shown in Figure 3, illustrating a pattern not in the original PET images. Visual inspection revealed that parametric images formed with different heterogeneity indices exhibit various textural patterns.

## 4. Discussion

The search for image-based biomarkers remains an important but challenging aspect of clinical cancer imaging. As imaging technology continues to improve, information extraction from the reconstructed images becomes very important in maximizing the benefit of imaging studies. Recently, the term “radiomics” is proposed to describe the concept of integrating the information extracted from medical images into the proteogenomic and phenotypic information [7, 8]. It is apparent that, for such applications, conventional indices like SUV may not provide sufficient information. Advanced image analysis and information extraction methods become

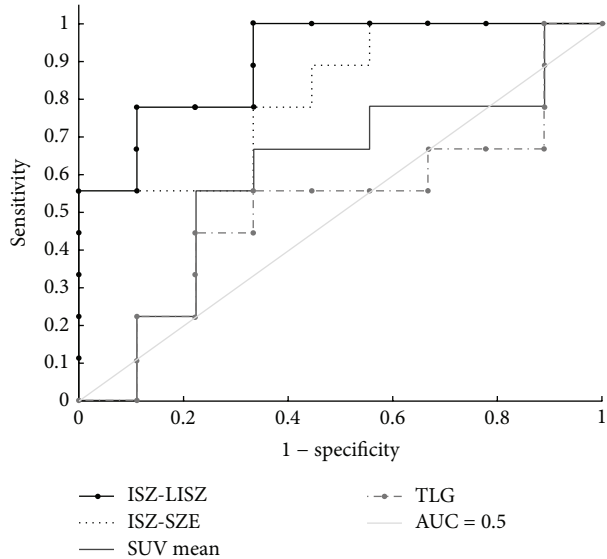


FIGURE 2: ROC curves of the heterogeneity indices, comparing two of the indices to the conventional metrics. The heterogeneity indices show a higher discriminative power than  $\text{SUV}_{\text{mean}}$  and TLG.

an inevitable component for the concept of radiomics, in order to maximize the amount of information that can be extracted from medical images. Quantification of tumor heterogeneity with texture analysis has been regarded as a promising field by several recent review articles [7, 8, 11, 13]. Recent reports have shown the application of tumor heterogeneity measured with textural features in nonsmall cell lung cancer [4], nasopharyngeal carcinoma [5], cervical cancer [6], peripheral nerve sheath tumors [9], gastrointestinal stromal tumors [12], and esophageal squamous cell carcinoma [27] based on FDG-PET images. Heterogeneity analysis has also been applied to the molecular image analysis of data from animal studies [28–30].

Although texture analysis may be a useful tool to quantify tumor heterogeneity from images, many questions require answers before this concept becomes a clinical standard. The first question arises from the signal and contrast source for different imaging methods. For example, FDG-PET reflects the glucose metabolism of tissues. A tumor that is spatially heterogeneous in cell proliferation may not appear heterogeneous in FDG-PET images, even with perfect resolution, as glucose metabolism may not be directly correlated to the proliferation. On the other hand, the properties of an imaging modality are also critical to texture analysis. The spatial resolution and signal-to-noise ratio (SNR) will both affect the performance of texture analysis. Low spatial resolution degrades the heterogeneity displayed on the acquired image, while high noise will cause a natively homogeneous image to show a high variation in pixel intensity. As a result, the results from texture analysis obtained from clinical PET images should be carefully interpreted and evaluated due to the resolution and noise limitations of PET. Researchers, who believe in the usefulness of quantification for tumor

heterogeneity, should take on the responsibility of providing the imaging community with evidence-based studies.

As heterogeneity quantification or texture analysis with molecular images is still a relatively new technology, especially for nuclear medicine community, a free and open-source software package can become a key component for the success of such emerging technologies. Without it, investigators wishing to evaluate heterogeneity indices must develop in-house software, which can be time-consuming and resource limited. A free software package can therefore attract more investigators and allow them to test such new quantification methods on their data with a minimum effort and cost. The other important software characteristic that is much desired is the availability of the source codes to the users. Such efforts for open-source projects in medical imaging have been undertaken by many groups, producing tools such as the kinetic modeling software COMKAT [31, 32] and radiation therapy software CERR [33]. An open-source project has many benefits. It allows the source code to be examined for programming errors. Users with programming abilities may contribute to new functionalities. Most importantly, once the source code is agreed upon by most of the developers, such a software package may become a standardized platform for different groups of researchers to have a common ground for data comparison. A very successful model is the Statistical Parametric Mapping (SPM) [34], which has now become the standard software tool for neuroimaging research as it continues to expand its functionality and user base. CGITA has a long way to go before achieving such maturity like SPM. But with more users and developers being attracted by CGITA, we believe that it has the potential to become the standard software platform for studying the tumor heterogeneity with molecular images. For vendors who wish to develop and test heterogeneity functions in their commercial software, CGITA may also serve as a reference for software verification, thereby accelerating the research and understanding of quantifying tumor heterogeneity.

In brief, CGITA has the following features that may be attractive to different user groups. First, it is easy to use and has a simple GUI. For users without a MATLAB license, a compiled stand-alone executable is also provided on the website. Users without a programming background can easily apply CGITA to their image data. Second, it is open source and allows users to create new functions. Third, it supports more than seventy textural features and its functionalities continue to expand in this regard. Fourth, it has the unique feature of parametric imaging with heterogeneity indices. Finally, CGITA can be executed under a batch mode. The texture analysis of multiple subjects can be performed automatically without user intervention, which is extremely helpful for processing a large amount of data, an unavoidable task for future studies aiming to evaluate the heterogeneity quantification of molecular images. As a result, we believe CGITA will serve as a useful and practical tool for molecular imaging investigators.

A cohort of eighteen ORC patients was used in our study to test our software and demonstrate the potential application of heterogeneity indices. Because the cohort size is small, our

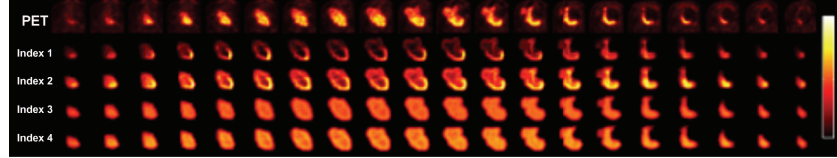


FIGURE 3: Parametric images of textural features computed from a single patient compared to the original PET image. The PET image, shown in the top row, is displayed between SUVs of zero and twenty. Heterogeneity indices 1 to 4 represent, respectively, the contrast, dissimilarity, entropy, and inverse difference moment calculated from the cooccurrence matrix. Note that the parametric images appear different according to the spatial variation in voxel intensity. Furthermore, different index images display different tumor heterogeneity patterns.

intention is not to perform a theoretical study for establishing a standard to stratify advanced ORC patients with textural features. Instead, this case study is a demonstration of how a software package for heterogeneity quantification could be applied to patient data for research purposes. In our report, we chose the task of using heterogeneity indices for prognosis, aiming to test whether heterogeneity indices computed with CGITA might be better discriminators than conventional metrics, such as SUV. Indeed, the results support the claim that textural features may be more informative than SUV in this small-cohort case study. Judging from the ROC analysis, many of the implemented textural features showed better AUC than the AUC with  $SUV_{mean}$  in outcome prediction power. Two of these features (ISZ-LISZE, ISZ-SZE) even improve the AUC from 0.6 to 0.81 and 0.9. The sensitivity and specificity have also been improved by heterogeneity indices. Although this study is not aimed to find the theoretical relationship between the heterogeneity indices and disease outcome, we may still speculate the reasons behind such findings. SUV and heterogeneity indices, by nature, represent different physiological and biological mechanisms. In general, SUV represents the “amount” of tracer present in local areas (e.g.  $SUV_{max}$ ) and the whole tumor ( $SUV_{mean}$ ), while heterogeneity indices express the “distribution variation” of tracer activities. The more heterogeneous a tumor is, the more likely a tumor is attempting to differentiate and generating different colonies to survive in its environment, especially during therapy. This may be the underlying reason that enables ISZ-LISZE and ISZ-SZE to improve the AUC from  $SUV_{mean}$  because they are capable of capturing the tumor’s heterogeneity by emphasizing the tumors with many small “zones,” which is defined as the number of interconnected voxels with the same voxel intensity. As a result, the quantified tumor heterogeneity may serve as a better indicator for tumor aggressiveness which has a direct impact on patients’ prognosis and survival. This might explain why heterogeneity indices in general show stronger power for outcome prediction, in our data as well as in the literature [35–37]. However we would also like to point out that, because we have a small patient cohort, the heterogeneity indices that are found with the best performance need to be further validated with a larger amount of data. Further validation is necessary in the future.

The image quality is also an important factor for heterogeneity quantification that requires further study and validation, especially in the spatial resolution and SNR. In our study, we used a PET camera with a spatial resolution

of about 6 mm and system sensitivity of about 0.7% [24]. Current state-of-art cameras could achieve a higher spatial resolution of about 4 mm and system sensitivity of 0.9% [38]. Improvement on the spatial resolution with new cameras and image SNR by a higher tracer dose undoubtedly will increase the accuracy for heterogeneity quantification. However, the minimum requirement of image quality for a specific disease remains to be further studied. In our study, since the tumor size is generally large in our cohort with an average volume of 107 mL, a spatial resolution of 6 mm is probably sufficient. Similarly, since the tracer uptake is fairly high with  $SUV_{mean}$  above five, the SNR should not be a concern under the standard injection dose of 370 MBq of FDG. With our current data, it is not feasible to determine the smallest tumor or the worst noise level that can still produce accurate tumor heterogeneity quantification. Such studies may require animal or phantom studies, in which the injected dose and image acquisition mode can be more freely modified and tested. CGITA may facilitate such testing on the software side. The exact determination of the spatial resolution and system sensitivity requirements awaits future investigation.

We are not the first group to propose the parametric imaging of heterogeneity indices. For example, a previous report has demonstrated such techniques applied to MRI for lesion segmentation purposes [39]. However, to our knowledge, we are the first group to implement this function as part of an open-source project for quantifying the tumor heterogeneity of medical imaging. We tested this functionality in our patient cohort and were able to obtain heterogeneity parametric images. Unfortunately, we do not possess in vitro images of tumor heterogeneity with which our parametric images are compared because our cohort did not undergo surgical dissection of the tumor. However, it is still quite interesting to examine these images, as shown in Figure 3. For example, in the cooccurrence-contrast images, a hot spot is shown on the bottom right portion of the tumor, indicating a high variation in the voxel intensity in this area. It is easy to see that the hot spots in the original PET images and the heterogeneity images are quite different in terms of both size and location. This is reasonable because the parametric images are calculated based on the heterogeneity indices and therefore represent the spatial variation of tracer uptake. Efforts have been reported to use heterogeneity parametric images for tumor delineation and radiation targeting [40]. We believe such heterogeneity images could do much more than simply determining the tumor contour. One potential role for heterogeneity images in particular, we believe, is to serve

as the guide for dose-boosting techniques for targeting the radiation dose at the most aggressive areas. Further validation must be done to verify the relationship between heterogeneity images and local aggressiveness of the tumor. This could be achieved by comparing the heterogeneity images to the whole-mount pathology or immunohistochemistry data. Since we do not have appropriate data to study the relationship between heterogeneity images and the distribution of aggressive colonies, we hope that CGITA may encourage investigators who own such data to test this hypothesis for expanding the use of heterogeneity indices.

We would also like to comment that, although CGITA is targeted at oncological applications, it can also be applied in other fields, such as neurology. It is also not limited to PET, as long as the images are stored in the DICOM format that CGITA can import. This makes CGITA also a useful tool for analyzing experimental animal data. We have tested CGITA with CT and MR images for heterogeneity index computation, as shown in Supplemental Figures 1 and 2 (see Supplementary Materials available online at <http://dx.doi.org/10.1155/2014/248505>). Quite a few CGITA features can be further improved in the future for image display, segmentation, and acceleration for computation. New texture analysis methods, such as those based on wavelets [41], will be investigated and added to CGITA in the future. At this moment, CGITA is solely for research purposes and shall not be used for clinical diagnosis. Interested developers are welcome to join the project to advance the functionalities of CGITA.

## 5. Conclusion

We present the CGITA software package for quantifying the tumor heterogeneity with molecular images. As a user-friendly, open-source program that is free for academic use, CGITA could assist investigators to apply heterogeneity analysis to their data. With a pilot cohort of eighteen advanced ORC patients treated with definitive radiotherapy, we found that heterogeneity indices may serve as better prognosis predictors for patient outcome by improving both the sensitivity and specificity. We believe that CGITA will facilitate and accelerate our understanding of the usefulness of heterogeneity quantification and its future clinical role in patient management. Furthermore, we hope an open-source software model like CGITA can facilitate the establishment of clinical standards for heterogeneity analysis in the future to further expand its clinical use.

## Conflict of Interests

The authors declare that they have no competing interests.

## Acknowledgment

This work is supported by the National Science Council in Taiwan under Grant 102-2221-E-182-074-MY2.

## References

- [1] T. A. Denison and Y. H. Bae, "Tumor heterogeneity and its implication for drug delivery," *Journal of Controlled Release*, vol. 164, pp. 187–191, 2012.
- [2] D. L. Longo, "Tumor heterogeneity and personalized medicine," *The New England Journal of Medicine*, vol. 366, no. 10, pp. 956–957, 2012.
- [3] D. Shibata, "Heterogeneity and tumor history," *Science*, vol. 336, no. 6079, pp. 304–305, 2012.
- [4] G. J. Cook, C. Yip, M. Siddique et al., "Are pretreatment 18F-FDG PET tumor textural features in non-small cell lung cancer associated with response and survival after chemoradiotherapy?" *Journal of Nuclear Medicine*, vol. 54, pp. 19–26, 2013.
- [5] B. Huang, T. Chan, D. L. Kwong, W. K. Chan, and P. L. Khong, "Nasopharyngeal carcinoma: investigation of intratumoral heterogeneity with FDG PET/CT," *American Journal of Roentgenology*, vol. 199, pp. 169–174, 2012.
- [6] E. A. Kidd and P. W. Grigsby, "Intratumoral metabolic heterogeneity of cervical cancer," *Clinical Cancer Research*, vol. 14, no. 16, pp. 5236–5241, 2008.
- [7] V. Kumar, Y. Gu, S. Basu et al., "Radiomics: the process and the challenges," *Magnetic Resonance Imaging*, vol. 30, pp. 1234–1248, 2012.
- [8] P. Lambin, E. Rios-Velazquez, R. Leijenaar et al., "Radiomics: extracting more information from medical images using advanced feature analysis," *European Journal of Cancer*, vol. 48, no. 4, pp. 441–446, 2012.
- [9] J. Salamon, T. Derlin, P. Bannas et al., "Evaluation of intratumoural heterogeneity on (18)F-FDG PET/CT for characterization of peripheral nerve sheath tumours in neurofibromatosis type 1," *European Journal of Nuclear Medicine and Molecular Imaging*, vol. 40, no. 5, pp. 685–692, 2013.
- [10] F. Tixier, C. Cheze le Rest, M. Hatt et al., "Intratumor heterogeneity characterized by textural features on baseline 18F-FDG PET images predicts response to concomitant radiochemotherapy in esophageal cancer," *Journal of Nuclear Medicine*, vol. 52, no. 3, pp. 369–378, 2011.
- [11] D. Visvikis, M. Hatt, F. Tixier, and C. Cheze le Rest, "The age of reason for FDG PET image-derived indices," *European Journal of Nuclear Medicine and Molecular Imaging*, vol. 39, pp. 1670–1672, 2012.
- [12] T. Watabe, M. Tatsumi, H. Watabe et al., "Intratumoral heterogeneity of F-18 FDG uptake differentiates between gastrointestinal stromal tumors and abdominal malignant lymphomas on PET/CT," *Annals of Nuclear Medicine*, vol. 26, pp. 222–227, 2012.
- [13] S. Chicklore, V. Goh, M. Siddique, A. Roy, P. K. Marsden, and G. J. Cook, "Quantifying tumour heterogeneity in (18)F-FDG PET/CT imaging by texture analysis," *European Journal of Nuclear Medicine and Molecular Imaging*, vol. 40, pp. 133–140, 2013.
- [14] M. Eichelberg, J. Riesmeier, T. Wilkens, A. J. Hewett, A. Barth, and P. Jensch, "Ten years of medical imaging standardization and prototypical implementation: the DICOM standard and the OFFIS DICOM Toolkit (DCMTK)," in *Medical Imaging: PACS and Imaging Informatics*, Proceedings of SPIE, pp. 57–68, International Society for Optics and Photonics, February 2004.
- [15] D.-C. He and L. Wang, "Texture features based on texture spectrum," *Pattern Recognition*, vol. 24, no. 5, pp. 391–399, 1991.
- [16] M.-H. Horng, Y.-N. Sun, and X.-Z. Lin, "Texture feature coding method for classification of liver sonography," *Computerized Medical Imaging and Graphics*, vol. 26, no. 1, pp. 33–42, 2002.

- [17] R. M. Haralick, K. Shanmugam, and I. Dinstein, "Textural features for image classification," *IEEE Transactions on Systems, Man and Cybernetics*, vol. 3, no. 6, pp. 610–621, 1973.
- [18] Y. Sun, J. Lu, and T. Yahagi, "Texture classification for liver tissues from ultrasonic B-scan images using testified PNN," *IEICE Transactions on Information and Systems*, vol. 89, no. 8, pp. 2420–2428, 2006.
- [19] H.-H. Loh, J.-G. Leu, and R. C. Luo, "The analysis of natural textures using run length features," *IEEE Transactions on Industrial Electronics and Control Instrumentation*, vol. 35, no. 2, pp. 323–328, 1988.
- [20] M. Amadasun and R. King, "Textural features corresponding to textural properties," *IEEE Transactions on Systems, Man and Cybernetics*, vol. 19, no. 5, pp. 1264–1273, 1989.
- [21] G. Thibault, B. Fertil, C. Navarro et al., "Texture indexes and gray level size zone matrix: application to cell nuclei classification," pp. 140–145, Pattern Recognition and Information Processing (PRIP), Minsk, Belarus, 2009.
- [22] C. Sun and W. G. Wee, "Neighboring gray level dependence matrix for texture classification," *Computer Vision, Graphics and Image Processing*, vol. 23, no. 3, pp. 341–352, 1983.
- [23] R. L. Wahl, H. Jacene, Y. Kasamon, and M. A. Lodge, "From RECIST to PERCIST: evolving considerations for PET response criteria in solid tumors," *Journal of Nuclear Medicine*, vol. 50, no. 1, pp. 122S–150S, 2009.
- [24] B. J. Kemp, C. Kim, J. J. Williams, A. Ganin, and V. J. Lowe, "NEMA NU 2-2001 performance measurements of an LYSO-based PET/CT system in 2D and 3D acquisition modes," *Journal of Nuclear Medicine*, vol. 47, no. 12, pp. 1960–1967, 2006.
- [25] M. K. Chung, H.-S. Jeong, G. P. Sang et al., "Metabolic tumor volume of [18F]-fluorodeoxyglucose positron emission tomography/computed tomography predicts short-term outcome to radiotherapy with or without chemotherapy in pharyngeal cancer," *Clinical Cancer Research*, vol. 15, no. 18, pp. 5861–5868, 2009.
- [26] W. H. Kruskal and W. A. Wallis, "Use of ranks in one-criterion variance analysis," *Journal of the American Statistical Association*, vol. 47, pp. 583–621, 1952.
- [27] X. Dong, L. Xing, P. Wu et al., "Three-dimensional positron emission tomography image texture analysis of esophageal squamous cell carcinoma: relationship between tumor 18F-fluorodeoxyglucose uptake heterogeneity, maximum standardized uptake value, and tumor stage," *Nuclear Medicine Communications*, vol. 34, pp. 40–46, 2013.
- [28] S. Blouin, M. F. Moreau, M. F. Baslé, and D. Chappard, "Relations between radiograph texture analysis and microcomputed tomography in two rat models of bone metastases," *Cells Tissues Organs*, vol. 182, no. 3-4, pp. 182–192, 2006.
- [29] M. Dominiotto, S. Lehmann, R. Keist, and M. Rudin, "Pattern analysis accounts for heterogeneity observed in MRI studies of tumor angiogenesis," *Magnetic Resonance in Medicine*, vol. 70, no. 5, pp. 1481–1490, 2013.
- [30] F. Risse, J. Pesic, S. Young, and L. E. Olsson, "A texture analysis approach to quantify ventilation changes in hyperpolarised<sup>3</sup>He MRI of the rat lung in an asthma model," *NMR in Biomedicine*, vol. 25, no. 1, pp. 131–141, 2012.
- [31] R. F. Barajas Jr., J. G. Hodgson, J. S. Chang et al., "Glioblastoma multiforme regional genetic and cellular expression patterns: influence on anatomic and physiologic MR imaging," *Radiology*, vol. 254, no. 2, pp. 564–576, 2010.
- [32] R. F. Muzic Jr. and S. Cornelius, "COMKAT: compartment model kinetic analysis tool," *Journal of Nuclear Medicine*, vol. 42, no. 4, pp. 636–645, 2001.
- [33] J. O. Deasy, A. I. Blanco, and V. H. Clark, "CERR: a computational environment for radiotherapy research," *Medical Physics*, vol. 30, no. 5, pp. 979–985, 2003.
- [34] K. J. Friston, J. T. Ashburner, S. J. Kiebel, T. E. Nichols, and W. D. Penny, *Statistical Parametric Mapping: The Analysis of Functional Brain Images*, Academic Press, New York, NY, USA, 2011.
- [35] J. F. Eary, F. O'Sullivan, J. O'Sullivan, and E. U. Conrad, "Spatial heterogeneity in sarcoma 18F-FDG uptake as a predictor of patient outcome," *Journal of Nuclear Medicine*, vol. 49, no. 12, pp. 1973–1979, 2008.
- [36] I. El Naqa, P. W. Grigsby, A. Apte et al., "Exploring feature-based approaches in PET images for predicting cancer treatment outcomes," *Pattern Recognition*, vol. 42, no. 6, pp. 1162–1171, 2009.
- [37] M. Vaidya, K. M. Creach, J. Frye, F. Dehdashti, J. D. Bradley, and I. El Naqa, "Combined PET/CT image characteristics for radiotherapy tumor response in lung cancer," *Radiotherapy and Oncology*, vol. 102, no. 2, pp. 239–245, 2012.
- [38] B. W. Jakoby, Y. Bercier, M. Conti, M. E. Casey, B. Bendriem, and D. W. Townsend, "Physical and clinical performance of the mCT time-of-flight PET/CT scanner," *Physics in Medicine and Biology*, vol. 56, no. 8, pp. 2375–2389, 2011.
- [39] F. Kruggel, J. S. Paul, and H.-J. Gertz, "Texture-based segmentation of diffuse lesions of the brain's white matter," *NeuroImage*, vol. 39, no. 3, pp. 987–996, 2008.
- [40] H. Yu, C. Caldwell, K. Mah et al., "Automated radiation targeting in head-and-neck cancer using region-based texture analysis of PET and CT images," *International Journal of Radiation Oncology Biology Physics*, vol. 75, no. 2, pp. 618–625, 2009.
- [41] S. Joseph and K. Balakrishnan, "Local binary patterns, haar wavelet features and haralick texture features for mammogram image classification using artificial neural networks," *Communications in Computer and Information Science*, vol. 198, pp. 107–114, 2011.

## Review Article

# Pushing CT and MR Imaging to the Molecular Level for Studying the “Omics”: Current Challenges and Advancements

**Hsuan-Ming Huang and Yi-Yu Shih**

*Healthcare Sector, Siemens Limited Taiwan, 2F No. 3, Yuan Qu Street, Nan Gang District, Taipei 11503, Taiwan*

Correspondence should be addressed to Yi-Yu Shih; [yiyushih@gmail.com](mailto:yiyushih@gmail.com)

Received 18 October 2013; Revised 26 December 2013; Accepted 24 January 2014; Published 13 March 2014

Academic Editor: Yu-Hua Dean Fang

Copyright © 2014 H.-M. Huang and Y.-Y. Shih. This is an open access article distributed under the Creative Commons Attribution License, which permits unrestricted use, distribution, and reproduction in any medium, provided the original work is properly cited.

During the past decade, medical imaging has made the transition from anatomical imaging to functional and even molecular imaging. Such transition provides a great opportunity to begin the integration of imaging data and various levels of biological data. In particular, the integration of imaging data and multiomics data such as genomics, metabolomics, proteomics, and pharmacogenomics may open new avenues for predictive, preventive, and personalized medicine. However, to promote imaging-omics integration, the practical challenge of imaging techniques should be addressed. In this paper, we describe key challenges in two imaging techniques: computed tomography (CT) and magnetic resonance imaging (MRI) and then review existing technological advancements. Despite the fact that CT and MRI have different principles of image formation, both imaging techniques can provide high-resolution anatomical images while playing a more and more important role in providing molecular information. Such imaging techniques that enable single modality to image both the detailed anatomy and function of tissues and organs of the body will be beneficial in the imaging-omics field.

## 1. Transition from Morphological to Molecular Imaging

Over the past few decades, imaging data have been widely used to study how body system work together at the organ-tissue level. In contrast, omics data obtained from genomics, metabolomics, proteomics, and pharmacogenomics have been used to provide biological information at the cellular and molecular level. Such omics data may provide a great opportunity to understand the development and progression of diseases. With the integration of imaging and omics data, scientists may find new insights into the mechanism of disease and its treatment. To integrate images as part of the omics, imaging techniques are needed to be safe, fast, accurate and convenient. More importantly, these techniques should have the ability to provide anatomical and functional information.

Among several imaging techniques, computed tomography (CT) and magnetic resonance imaging (MRI) have the potential to satisfy the above requirements. First, human anatomical structures can be imaged using both CT and MRI.

Second, recent studies showed that genomics data were correlated with functional (molecular) CT and MRI data [1–8]. It is noteworthy that MR spectroscopy is a conventional technology which could approach *in vivo* molecular and metabolism information, and there are many valuable results combined with various omics data in different clinical applications, such as oncology and neural diseases, in recent decades [9–12]. Moreover, several nanoparticles such as gold nanoparticles [13, 14] and polymer-coated bismuth sulfide nanoparticles [15] have emerged as novel CT contrast agents for cancer detection. Similarly, some novel genetically encoded MRI contrast agents and advanced sequence technologies have been used to detect gene expression [16–19]. Finally, due to the advantages of cost, convenience (for CT), and safety (for MRI), both CT and MRI will be appropriate imaging techniques for imaging-omics integration.

To build and validate the relationship between omics data and imaging features, there are several limitations that need to be considered. In CT, both anatomical and functional data can be obtained within a few minutes. However, multiple CT scans are required, and patients would receive a high dose

	Filter and collimator	Subject-related parameters	Detector	Image reconstruction
Dose saving	20%~40%	Tube current: 20%~40% Tube voltage: 20%~60%	ASIC: 20%~30% Photon-counting detector: >40%	50%~80%

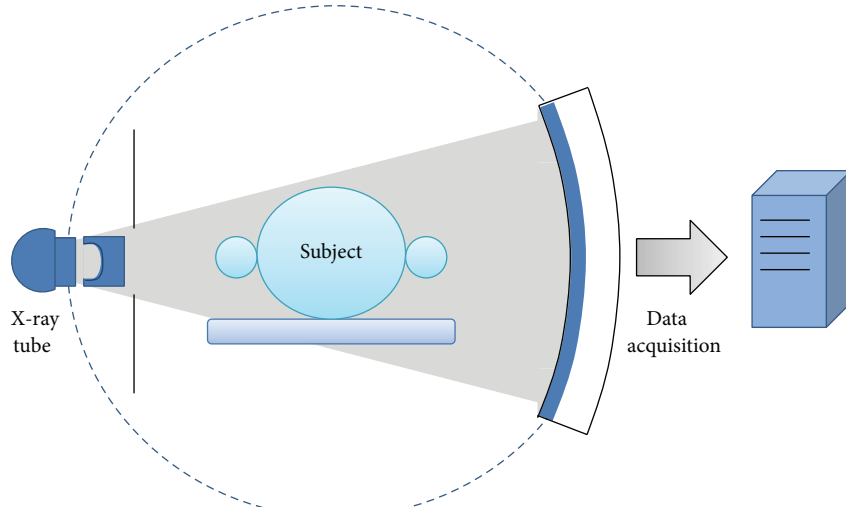


FIGURE 1: The key component of a CT system and the dose-saving potential of each component.

of radiation that may increase the risk of developing cancer. As a result, dose reduction in CT is an important issue for the integration between CT and omics data. Unlike CT, MRI does not use ionizing radiation. However, it takes a relatively long acquisition time to obtain anatomical and functional data and may not be acceptable for uncooperative subjects. Thus, acceleration is an important issue for the integration between MRI and omics data. Since the radiation dose of CT and acquisition time of MRI can determine the quantity and quality of anatomical and functional data, they are the key to imaging-omics integration. Hence, the aim of this paper is to review existing technological strategies and new directions that are used for reducing radiation dose in CT and acquisition time in MRI.

## 2. Dose Reduction in Computer Tomography

Nowadays, CT is one of the most commonly used imaging modalities because CT scanning is simple, fast, noninvasive, and accurate. Despite the tremendous benefits of CT scans, radiation dose from CT scans may be a potential risk factor for cancer development. In order to keep radiation as low as reasonably achievable (ALARA), techniques and strategies for reducing patient dose are highly desirable. We would discuss the dose-saving strategies of each component in a CT system shown in Figure 1.

### 2.1. CT Data Acquisition and Processing

**2.1.1. Beam Filtration.** Generally, X-ray beam emitted from an X-ray tube contains a spectrum of photon energies. Among these X-rays, soft (i.e., low-energy) X-rays are not hard

enough to efficiently penetrate the subject. As a result, soft X-rays contribute to patient radiation dose without providing useful information. In order to reduce the radiation dose to a patient, X-ray filters that block soft X-rays were developed. Due to differences in attenuations between the central and peripheral regions, commercial CT scanners are commonly equipped with a beam-shaping filter or bow-tie filter instead of the flat filter [22, 23]. In addition, specific beam-shaping filters that adapt to different examinations such as head, body, and cardiac were developed [24]. One possibility for further reducing patient dose is to use dynamic bow-tie filters which modify X-ray beam as a function of view angle [25, 26].

**2.1.2. Collimator.** Since the focal spot in the X-ray tube is not truly a point source, beam coverage in some regions is partially irradiated. These regions are called penumbra. In multislice CT, overbeaming caused by focal spot penumbra does not contribute to image reformation. As a result, exposure to such radiation is unnecessary. In multislice row CT, thick beam collimation has better radiation utilization [27]. This is because radiation dose due to overbeaming constitutes a smaller percentage of total absorbed doses. However, thick collimation only allows reconstruction of thick sections. To reconstruct thin sections, thin collimator that reduces radiation utilization is required. This indicates that beam collimation should be selected based on the requirements of clinical examinations.

In multislice CT, spiral scan is the commonly used scanning mode which results in overscanning or overradiation [28, 29]. To obtain sufficient data for reconstructing image at the beginning and end of the  $z$ -axis scan range, at least an additional one-half of a gantry rotation is prerequisite. This

so-called overscanning contributes to patient dose but does not contribute to image reformation. Therefore, a hardware-based solution that uses the dynamic or adaptive collimator to block the pre- and postspiral radiation was introduced and used in clinical practice [30, 31].

**2.1.3. Detector.** In a CT system, X-ray detector is probably the most important component that converts incident X-ray beam into digital signals. In the 1980s, xenon-gas ionization chamber detectors were commonly used in CT. However, with improvements in technology, xenon-gas detectors are replaced by solid-state detectors (e.g., gadolinium oxysulfide) which have higher quantum efficiency. In normal-dose CT examinations, noise from the electronic components of the detector system is negligible and has no significant impact on image quality. However, in low-dose CT examinations, electronic noise becomes one of the most significant factors determining image quality. Hence, it is important to figure out how electronic noise in low-dose scans can be reduced. In recent years, two new CT detectors, GE's Gemstone Detector and Siemens' Stellar Detector, were introduced into the market. Gemstone Detector made from a garnet-based scintillator enables improvements in spatial resolution and signal-to-noise ratio (SNR). Besides, Stellar Detector that combines the photodiode and the analog-to-digital converters (ADC) in one application specific integrated circuit (ASIC) allows a ~20% reduction in electronic noise. As a result, CT scanners equipped with new detectors are expected to have a reduction in patient dose.

Generally, X-ray detectors currently used in clinical CT scanners are energy integrating. In contrast to conventional energy-integrating detectors, photon-counting detectors not only count each photon individually but also record the energy level of each detected photon. Based on the energy-resolving information, photon-counting detectors have the ability to eliminate electronic noise as well as scattered radiation [32, 33]. In addition, photon-counting detectors with energy discrimination capabilities can be used to improve SNR by assigning an energy-dependent weighting factor to each individual photon [34–36]. Due to the improvement of SNR, the patient dose can be further reduced while maintaining acceptable image quality.

In practice, photon-counting detectors are not widely used in CT systems. This is primarily because the fluxes of incident photons are too high. Under high flux irradiation, the pulse resolving time is relatively too long to allow the detector recording each individual photon. As a result, overlapping pulses which lead to a spectral distortion and a loss of counts may occur. This phenomenon is called pulse pileup [37]. Although a clinical CT scanner equipped with photon-counting detectors is not available yet, recent advances in detector electronics and semiconductor detector materials have been contributed to developing a photon counting-based micro-CT system [38–40]. We expect that a photon counting-based CT will soon be ready for clinical study.

**2.1.4. Tube Current.** Among many scanning parameters, tube current is one of the important factors determining the

radiation dose delivered to the patient. Hence, one commonly used technique to reduce radiation exposure is to adapt the tube current according to the patient's size, shape, and attenuation. Methods that automatically modulate the tube current to adapt differences in patient attenuation are known generically as automatic exposure control (AEC) [41–44]. Now, in most modern CT scanners, AEC can perform automatic adjustment of tube current both during tube rotation (i.e., angular modulation) and along the *z*-axis of the patient (i.e., *z*-axis modulation). In angular modulation, the tube current is adjusted to adapt differences in attenuation between anteroposterior and lateral positions. Unlike angular modulation, the *z*-axis modulation adjusts the tube current to accommodate differences in attenuation along the *z*-axis of the patient (e.g., shoulder and abdomen). The main aim of AEC is not only to modulate tube current but also to deliver the right dose in order to achieve adequate image quality for each individual patient and each diagnostic task. The underlying principle of AEC is similar; however, due to different definitions of image quality, AEC systems from four major CT manufacturers are implemented somewhat differently [45]. Despite these different implementations, the AEC techniques used in modern CT scanners contribute to a significant reduction in radiation dose to the patient while maintaining the adequate image quality [45].

**2.1.5. Tube Potential.** To date, lowering tube potential has been demonstrated to improve image quality or reduce radiation dose in several clinical CT exams [46–52]. The underlying principle is based on the fact that iodine has an increased attenuation (i.e., higher contrast) as photon energy decreases toward the *k*-edge energy of iodine. This indicates that for the same radiation dose, the lower tube potential can yield better image quality than the higher tube potential. Alternatively, the improvement in image quality can contribute to reducing patient dose. However, with the increase of the patient size, low kilovoltage (kV) settings would lead to an increase in image noise. Hence, dose reduction using lower tube potential is feasible only if the patient size is below a particular threshold. However, in routine CT scans, it is difficult to determine the optimal kV setting for individual patient, simply because of the complex relationship among kV, mAs, dose, contrast, and image noise. To solve this problem, Siemens recently introduced a novel tool, CARE kV, which allows the optimal kV to be determined automatically for each individual patient and each specific exam. Basically, CARE kV uses information obtained from the topogram to determine the optimal kV which is used to maintain image quality (e.g., contrast-to-noise ratio). Together with AEC described above, this tool can be beneficial in optimizing and reducing radiation dose to each individual patient.

**2.1.6. Image Reconstruction.** Filtered back projection (FBP) is still the most common reconstruction method used in CT. Over the past two decades, iterative reconstruction (IR) method has been shown to be superior to conventional FBP method in terms of image noise and spatial resolution [53–56]. The improvement in image quality can directly lead to

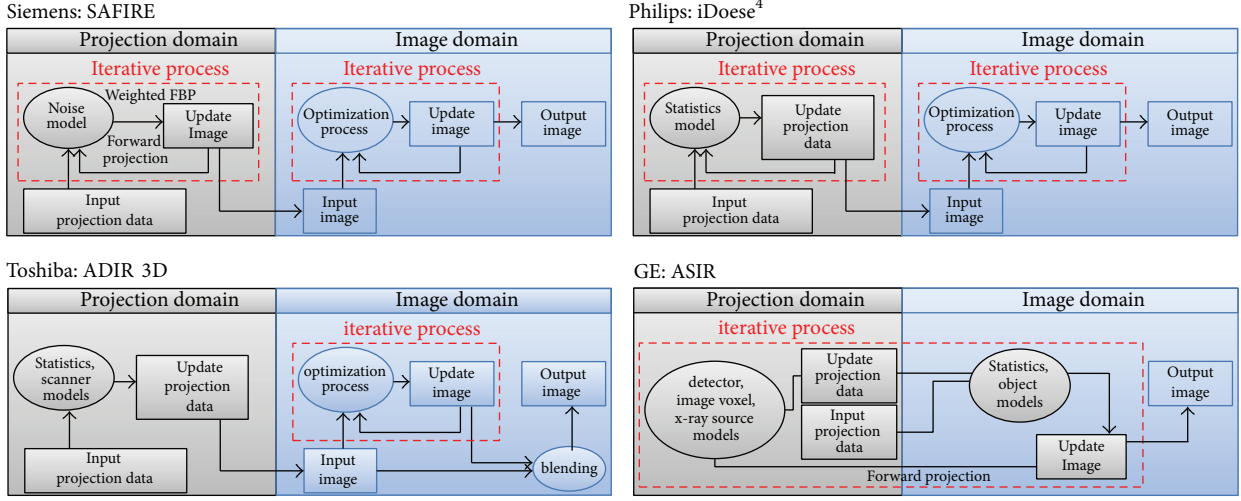


FIGURE 2: The schematic of four CT manufacturers' IR algorithms: Siemens' Sinogram Affirmed Iterative Reconstruction (SAFIRE), Philips' iDose<sup>4</sup>, Toshiba's Adaptive Iterative Dose Reduction 3D (ADIR 3D), and GE's Adaptive Statistical Iterative Reconstruction (ASIR). Both SAFIRE and iDose<sup>4</sup> have a similar iterative correction process operating in the image domain. In the projection domain, SAFIRE performs a projection data correction via forward and backward (i.e., weighted FBP) projection; however, iDose<sup>4</sup> directly corrects projection data. ADIR 3D performs a noniterative correction in the projection domain and an iterative correction in the image domain. Also, a weighted blending is applied to the input image (i.e., after projection data correction) and the output image (i.e., after iterative process). Unlike the other three IR algorithms, ASIR performs an iterative correction process by comparing synthesized projection data to measured projection data.

a significant reduction in patient dose. However, IR method is rarely used in routine CT exams, mainly owing to the high computational time required for modeling the system geometry and incorporating physical effects (e.g., noise, scatter, beam hardening, and detector response). Due to advances in hardware [57–59] and renewed emphasis on CT dose reduction, fast IR methods have recently been developed and implemented for radiation dose reduction. Now, IR methods are available on many CT scanners from four major CT manufacturers with different algorithms (Figure 2), to perform corrections in both the projection and the image domain. They are applied to achieve noise reduction and artifact reduction as well as to preserve structural edges.

Another important image reconstruction technique toward the goal of reducing radiation dose is the use of incomplete projection data, either to acquire a small number of projection angles or to use the truncated projection data. The first strategy is the sparse-view CT and the second one is the interior CT [60]. With the recent introduction of compressed sensing (CS) in CT [61, 62], it is possible to perform image reconstruction from a small number of projections while still maintaining image quality [63–67]. The basic concept of CS is to recover a signal or an image from measured data with sampling rates below the Nyquist criterion. To accurately restore the signal from the undersampled data, computational load may be still too high for practical use. Thanks to the hardware-accelerated image reconstruction technique [57–59], it is expected that fast CS-based reconstruction methods will be introduced to allow an ultra-low dose CT scan in clinical routine. On the other hand, interior CT uses the projection data passing through a region of interest (ROI) to reconstruct image. In practical, this technique can lead to a dose reduction in patients with cardiac or

breast CT scans. The exact ROI reconstruction methods from such truncated projection data have been proposed [68, 69]. Unlike approximate reconstruction methods [70, 71], the new analytical reconstruction method called differentiated backprojection (DBP) was shown to have a potential to exactly solve the ROI reconstruction [60]. Despite the fact that these reconstruction methods have a great potential to reduce CT radiation dose, there are some assumptions needed to be satisfied. For example, some prior knowledge about the object is required.

**2.2. Dual-Energy CT (DECT).** Due to the recent advances in CT technology including sandwiched detectors [72, 73], rapid kV switching [74], and dual-source and detector [75–77], there is a renewed interest in DECT. To date, DECT has many clinical applications such as bone removal with plaque highlighting, quantification of iodine concentration, visualization of tendons and ligaments, and characterization of renal calculi [78–80]. Using the material-specific information provided by DECT data, virtual noncontrast (VNC) images can be generated by removing iodine content from the dual-energy contrast-enhanced CT images. As a result, DECT has the advantage of omitting one unenhanced (i.e., precontrast) CT scan, thus reducing the overall radiation dose. For example, VNC images generated from either nephrographic- or excretory-phase DECT data may have the potential to replace unenhanced CT images for detection of urinary stone [81, 82], evaluation of haematuria [83] and characterization of renal masses [84, 85]. One recent study showed that iodine map generated from DECT can be used to differentiate between benign and malignant mediastinal tumors [86]. Moreover, iodine concentration provided by DECT strongly correlated with the maximum standardized uptake value of

<sup>18</sup>FDG PET that was commonly used functional imaging technology [87]. More importantly, initial results showed that DECT can be used as an imaging biomarker for predicting the therapeutic benefit in patients with gastrointestinal stromal tumors [88]. We believe that DECT is capable not only of providing functional imaging information but also of giving dose-saving opportunities.

**2.3. Perfusion CT (PCT).** PCT is an existing imaging technique that has been used to determine tissue perfusion from dynamic contrast-enhanced CT data. Due to the feasibility of rapid acquisition of data (i.e., multislice spiral CT) and the availability of commercial software, clinical applications of PCT in acute stroke, cardiology, and oncology have continued to increase [89, 90]. Recent results showed that PCT positively correlated with tumors in the study of animal models [91, 92]. With PCT, it is also possible to detect and predict tumor response to chemotherapy and radiation therapy [93]. To obtain perfusion parameters (e.g., blood flow and volume and vascular permeability), sequential acquisition of CT data after a bolus injection of contrast agent is required. Typical image acquisition time is about 30 seconds or longer, depending on organ or tissue being scanned, so the radiation dose of a PCT scan is much higher than that of a routine CT scan [94]. As a result, methods that allow for a significant reduction of CT dose without degrading image quality are highly desirable. Since PCT contains temporal information, reconstruction algorithms that incorporate temporal filtering techniques have been proposed to reduce image noise [95–99]. Indeed, such reconstruction algorithms can allow a significant reduction in image noise, thereby having a large potential to reduce the radiation dose in PCT. One alternative strategy to reduce radiation dose in PCT is to optimize scanning parameters such as total scanning time and sampling interval [100, 101]. With the implementation of dose-reduction technologies, PCT will be increasingly used in clinical practice.

**2.4. Summary.** We would like to summarize the CT dose reduction technologies so that it would be easier to understand their feasibilities.

- (i) To accomplish the principle of ALARA, each CT scan should be customized for the patient's age, weight, size, and imaging task. Individual customized CT scanning techniques used in current clinical CT scanners include examination-specific bow-tie filters, adaptive collimator, and automatic tube potential selection with tube current modulation.
- (ii) CT detectors with integrated electronics or a garnet-based scintillator have a great potential to reduce noise, thereby improving image quality and dose efficiency. CT scanners equipped with high-rate photon-counting detectors will be available in the near future for further dose reduction.
- (iii) As provided by four major CT manufactures, iterative reconstructions result in significant dose reduction and improved image quality over conventional filtered back projection reconstruction methods. New

reconstruction methods for sparse-view CT and interior CT will be an alternative to dose reduction.

### 3. Imaging Acceleration in Magnetic Resonance Imaging

Since the introduction of MRI in the early 1970's [102], its techniques have been much improved from hardware to image reconstruction. Due to the intrinsic physical limitation of MRI, the speed of data acquisition is always the problem comparing to CT. Hence, a number of acceleration techniques have been developed over the past four decades and the shortened acquisition time has greatly expanded clinical applications of MRI, especially for dynamic or time-resolved MRI, such as perfusion imaging [103–106], contrast-enhanced MR angiography [107–111], functional MRI [112, 113], and cardiac function examinations [114–117]. Those acceleration techniques could be divided into two categories: parallel imaging and dynamic acceleration. Besides, CS, which is beyond the limitation of Nyquist criterion [61, 62], inspires the MR physicists and the radiologists for even faster scans.

**3.1. Parallel Imaging.** The typical acquisition time of an MR image is the product of the repetition time (TR), number of phase-encoding lines ( $N_{PE}$ ), and the slice number ( $N_s$ ) (Figure 3). In order to shorten the scan time, the reduced phase-encoding  $k$ -space lines are generally acquired, which would either sacrifice the image resolution or result in the aliasing artifacts. Parallel imaging technique, which combines the design of the phase-arrayed coil and various image reconstruction algorithms, makes the faster data acquisition possible. Hence, the common features of the parallel imaging include the under-sampled  $k$ -space data and the phase-arrayed coils, which provided additional spatial information for image reconstruction to solve the aliasing patterns. The reconstruction algorithms could be divided into SENSE and GRAPPA family, where the undersampled data are reconstructed in image domain and  $k$ -space, respectively. Besides, the multislice acceleration acquisition is a kind of extension of parallel imaging and we would discuss it after the two conventional techniques.

**3.1.1. Generalized Autocalibrating Partially Parallel Acquisition (GRAPPA).** GRAPPA [118] technique originated from SMASH [119]. SMASH technique reconstructed the MR images from filling in the missing phase-encoding lines by using the phased-array coil, whose elements are parallel to the phase-encoding direction. Because the acquired signals from different surface coils imply the spatial sensitivity information in the meantime, they could be used to generate multiple datasets, which are called harmonics, by using linear combination with different weightings to complete the whole  $k$ -space. The restored full  $k$ -space was then Fourier-transformed to obtain the reconstructed image (Figures 2 and 3 in [119]). Depending on the concept of linear algebra,  $N$  components could form maximal  $N$  linearly independent combinations and result in maximal acceleration rate of  $N$ .

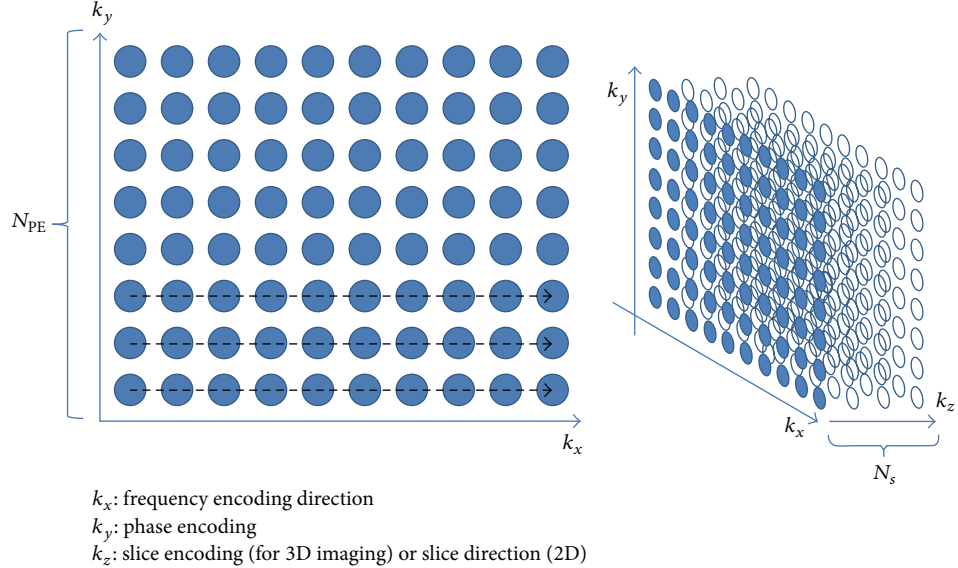


FIGURE 3: Illustration of three-dimensional  $k$ -space in MRI. Generally, the sampling time of  $k_x$  was less than repetition time (TR), so the acquisition time of a set of image could be written as  $\text{TR} \times N_{\text{PE}} \times N_s$ .

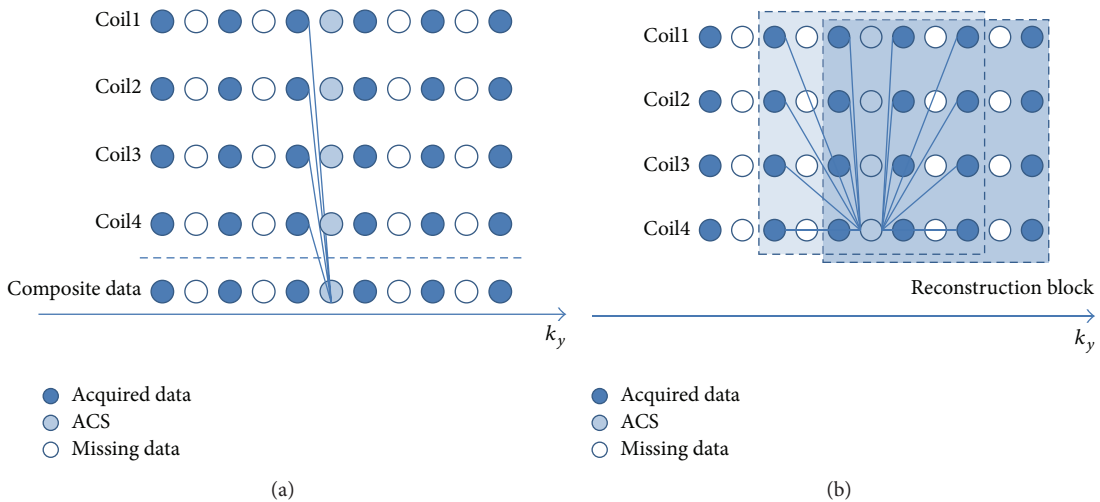


FIGURE 4: (a) AUTO-SMASH or VD-AUTO-SMASH reconstruction process for the acceleration rate of 2. Each  $k$ -line in a single coil was composited to fit the ACS line, and the relationship was applied to fill in the missing  $k$ -lines. The procedures constructed the whole  $k$ -space and then the reconstructed images were obtained. SMASH did not additionally acquire ACS. It used the estimated coil sensitivities to composite the missing data. (b) GRAPPA used multiple lines from all coils to fit a line in one coil. The reconstructed images from each coil were obtained after the  $k$ -space acquired from each coil was fully restored. The uncombined images were merged using sum of squares or other adaptive algorithms. The concept of reconstruction block made GRAPPA flexible using different "blocks" to fit the ACS lines for better performance. For example, at least there were three blocks used for ACS lines fitting, which would provide a more accurate outcome.

However, the harmonics are generally less than the total number of array components due to the geometrical constraints.

However, the major pitfall of SMASH is its high dependence on accurate coil sensitivity function, which might be easily affected by coil positions, subjects, and magnetic field inhomogeneities. Hence, some other methods accompanying the acquisition of autocalibration signals (ACS) near the central  $k$ -line were developed for the sensitivity function calibration, such as AUTO-SMASH [120] and VD-AUTO-SMASH [121]. Furthermore, GRAPPA provided a more

general form to reconstruct the full  $k$ -space data using multiple blocks in sliding manners rather than SMASH and its analogies from adjacent acquired  $k$ -lines (Figure 4). It is more flexible to fit the ACS from the acquired signals and restores the missing  $k$ -space data more precisely. The number of ACS is another factor to influence the reconstruction quality. Generally speaking, the more ACS acquired, the more accurate GRAPPA weightings obtained, which result in less artifacts but reduced the acceleration efficiency. GRAPPA is a more robust method and less relies on the coil sensitivity

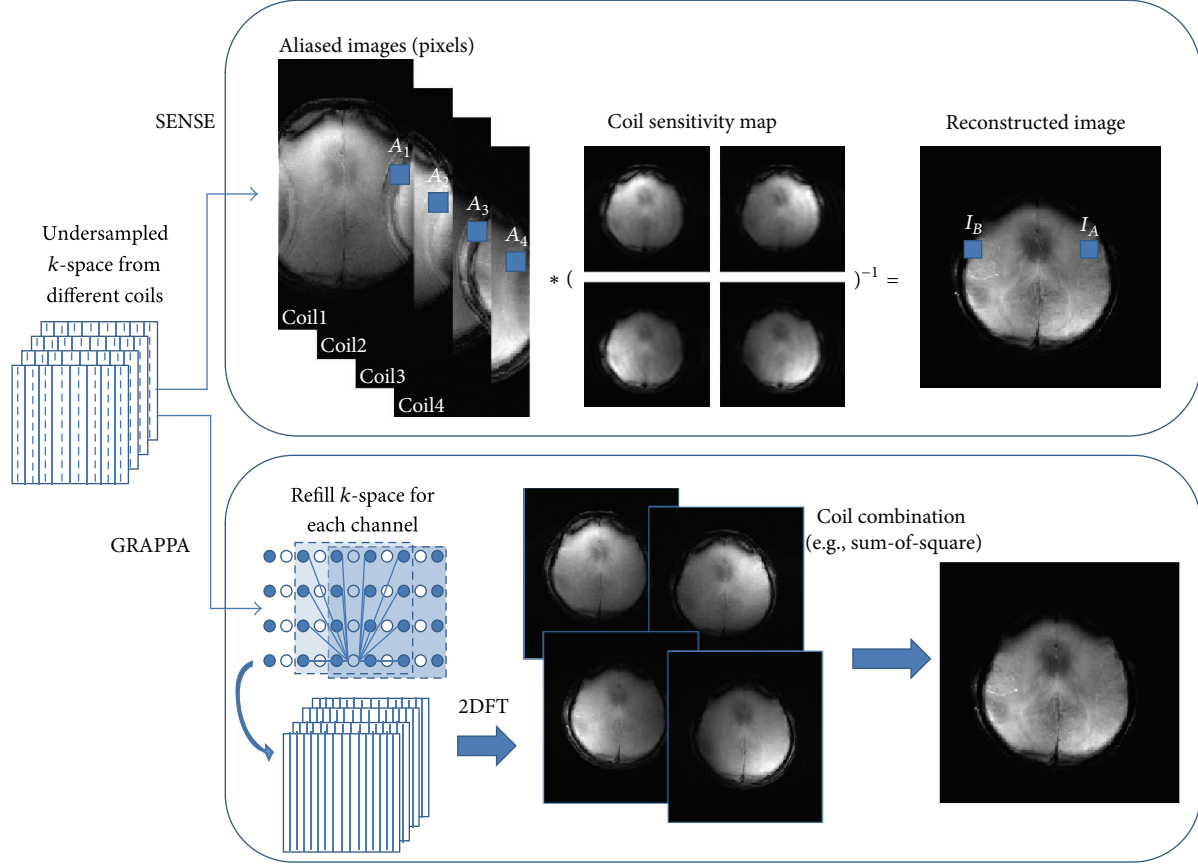


FIGURE 5: The reconstruction process of SENSE and GRAPPA. The example used a four-channel array coil for the acceleration rate of two. Each of the aliased pixels ( $A_1, A_2$ , and so on) came from  $I_A$  and  $I_B$  with different weightings depending on the coil sensitivity values. It could be represented as  $A_i = I_A C_{Ai} + I_B C_{Bi}$ , where  $A$  was the aliased pixel,  $I$  was the intensity of the unaliased pixel, and  $C$  was the coil sensitivity weighting from the corresponding location. It could be possible to reconstruct the data by finding the inverse matrices of coil sensitivity maps, which could be written as  $AC^{-1} = I$ . GRAPPA reconstructed the undersampled  $k$ -space using ACS fittings to calculate the GRAPPA weightings and refill the missing lines from each coil. Each restored full  $k$ -space was transformed to obtain the single-coil images, which were then combined together to finalize the reconstruction.

maps, so that the cardiac, lung, and abdominal applications become feasible. Besides, it could be also applied to 3D imaging [122, 123].

**3.1.2. Sensitivity Encoding (SENSE).** SENSE [124] technique began from the aliased images resulting from the undersampled  $k$ -space acquisition. Considering the case of acceleration factor  $R$ , each aliased pixel from different phase-arrayed coils should be divided into  $R$  partitions with different weightings relating to coil sensitivities (Figure 5). Hence, the coil sensitivity map, which is usually obtained from a low-resolution prescan at the beginning of the image acquisition, is the prior information for SENSE reconstruction. Since SENSE reconstruction much relies on the coil sensitivity map, the inaccurate sensitivity map would lead to residual aliasing artifacts. One of the most important factors to sensitivity map is SNR. Low SNR regions, for example, lung images, have a difficulty in determining the coil sensitivity distribution.

The common features for the two parallel imaging families are the reduction of SNR and the residual aliasing. The

significant difference is the reconstruction domain:  $k$ -space for GRAPPA and image domain for SENSE (Figure 5). The SNR reduction of parallel imaging could be generalized to

$$\text{SNR}_{\text{PI}} = \frac{\text{SNR}_{\text{fs}}}{g\sqrt{R}}, \quad (1)$$

where  $\text{fs}$  means full sampling,  $R$  is the acceleration factor, and  $g$  is the factor relating to some coil properties, such as geometry design [125, 126]. The meanings of  $g$ -factor in GRAPPA and SENSE are different, but it is mostly larger than one. Hence, many dedicated surface coils were developed, such as breast coils, spine arrays, and head coils, to reduce the noise enhancement. In addition, the ill-conditioned problem also leads to the loss of SNR. Thus, the use of regularization in SENSE [127–129] as well as GRAPPA [130] was developed. Though there are some compromises in parallel imaging, it is still routinely used in various clinical applications [131] due to improvements in acquisition time, spatial or temporal resolution, and image quality such as reduction of motion artifacts and EPI geometric distortion.

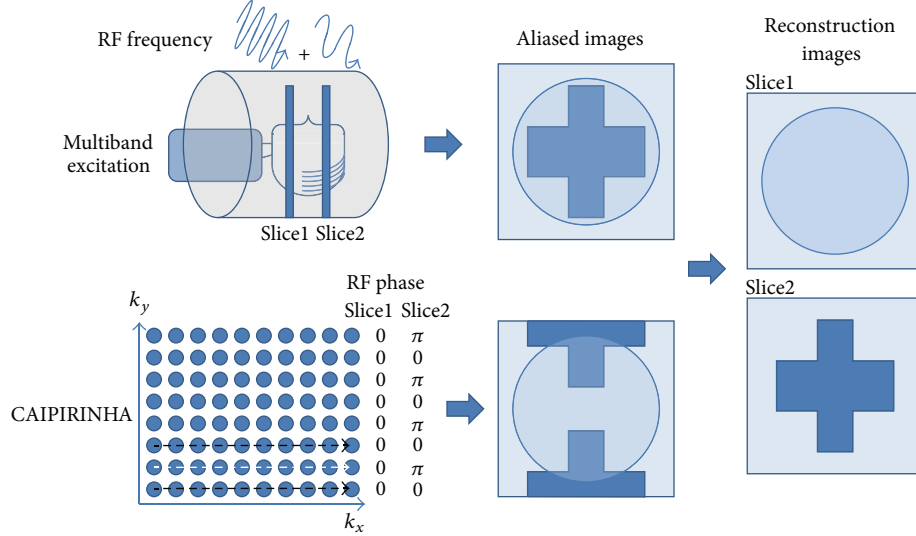


FIGURE 6: Schematic description of the differences between MB excitation and CAIPIRINHA. The slice selection gradient would be applied during the RF excitation, where the RF frequency and the slice resonant frequency were the same. Since MB excitation and CAIPIRINHA excited multiple slices simultaneously, the bandwidth of RF excitation would become wider than the single slice excitation. MB excitation modulated the RF excitation pulse with several frequencies to excite multiple slices, so the acquired images would overlap together without FOV shifting (the upper row). Considering the bandwidth of frequency encoding and the removal of the artifacts, the excitation slices should have gaps with several centimeters depending on the gradient strength. Besides, the pixel skew was another factors controlled by the gradient strength [20]. CAIPIRINHA, which also excited multiple slices simultaneously, controlled the aliasing pattern by phase-modulated RF pulses. In the figure, for example, the phase of RF pulse in the second slice was interlacedly altered to shift the overlapping patterns with  $FOV/2$  (the lower row). The black dashed arrow indicated the phase-encoding line without phase alteration in both slices, and the white one did the phase alteration of  $\pi$  only in the second slice. It could improve the  $g$ -factor to increase the SNR in image reconstruction. The technology could get rid of the pixel skew in MB excitation and make adjacent slice excitation feasible.

**3.1.3. Multislice Excitation.** GRAPPA and SENSE could be extended to 3D imaging [122, 123], which is slab excited without additional RF modification. An alternative idea for acceleration is the multislice simultaneous excitation with the sharing data acquisition schemes. The RF excitation type could be divided into frequency modulation, such as multiple band (MB) excitation [20, 132], and phase cycling, such as CAIPIRINHA [133] (Figure 6).

Both techniques have some intrinsic limitations. In MB excitation, the frequency offsets between slices should be at least equal to or larger than the slice bandwidth to ensure the successful reconstruction from the slice aliased images. Thus, two solutions could be applied: either to increase the gap between the excited slices at around several centimeters or to strengthen the slice selection gradient, which would result in the pixel skew. CAIPIRHNA, on the other hand, controlled the aliasing pattern using phase modulated multislice RF excitation pulses to avoid the pitfalls in MB excitation technique and improved the image quality of 2D-GRAPPA or 2D-SENSE reconstruction resulting from  $g$ -factor related noise enhancement (Figures 6 and 7 in [133]). Furthermore, instead of providing phase modulated RF pulses, the shifted aliasing patterns could perform more easily in 3D volume images via changing the encoding strategy (2D CAIPIRINHA) [21]. Hence, various developments in sequences [134, 135] and clinical applications [136, 137] were demonstrated more easily. However, neither CAIPIRINHA nor conventional MB excitation techniques are not applicable to single-shot echo planar

imaging (EPI), since the former method uses shot-by-shot RF modulation and the latter one suffers from high  $g$ -factors due to the hardware limitations. Hence, taking the concept of inclined readout [20, 132], the blipped wideband [138] and blipped-CAIPIRINHA [139] were proposed to make simultaneous multislice EPI and diffusion imaging feasible with reasonable  $g$ -factors. The significant advantages are that the temporal resolution could be increased for fMRI and the acquisition time could be much reduced for DSI or Q-ball imaging.

MB and CAIPIRINHA, generally in charge of the slice direction acceleration, could incorporate with the conventional parallel imaging techniques to fully achieve 2D acceleration in a better performance. Since all the techniques are based on the reduced  $k$ -space sampling for acceleration, the residual artifacts should be carefully dealt with.

**3.2. Dynamic Acceleration.** The dynamic MRI introduces temporal information into the acquisition, so it provides an additional dimension for acceleration. Only the signals of certain regions were varied with time in dynamic imaging; for example, contrast-enhanced angiography shows the signal intensity change in vessels and the rest parts are almost static. Hence, there are lots of redundant acquired data during the examination, and it could be well manipulated to reduce the scan time for each time frame and to increase the temporal resolution. The first idea came to view sharing in  $k$ -space.

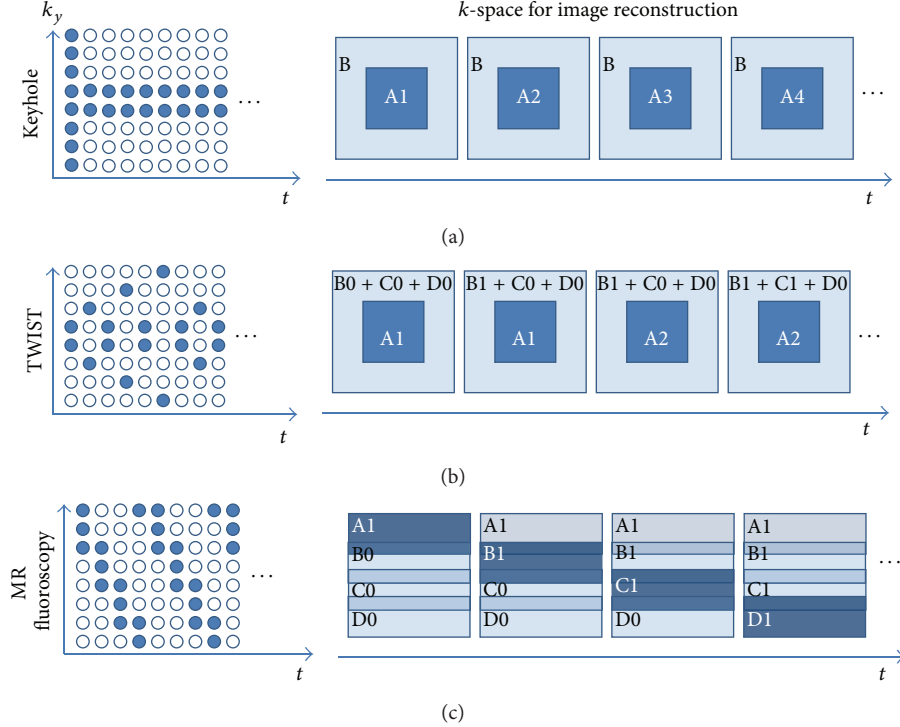


FIGURE 7: The sampling features in view-sharing technologies: Keyhole, TWIST, and MR fluoroscopy. (a) Keyhole acquired full  $k$ -space at the beginning or the end of the dynamic scan. Only central  $k$ -space (A1, A2, and so on, where the number indicated the times of update) was renewed at each time frame and the rest was kept the same for image reconstruction. (b) TWIST updated the central  $k$ -space information more frequently. The outer  $k$ -space was divided into several subregions, for example, three (B, C, and D) in this case, and only one of them was updated at each time frame interleaved by the renewal of the central  $k$ -space. (c) MR fluoroscopy updated the  $k$ -space sequentially and uniformly everywhere. Part of the information was acquired at each time frame and updated to  $k$ -space for dynamic image reconstruction.

**3.2.1. View Sharing.** Taking the advantages of the similarity of the adjacent time frames, several view sharing technologies were developed since the late 1980s, including MR fluoroscopy [140], Keyhole [141], BRISK [142], and TWIST [143, 144]. The major differences among the technologies are the manners on dynamical  $k$ -space data replacement and the data recovery.

MR fluoroscopy periodically updates the  $k$ -space data so that the refreshed rate of each part is the same. Because partial  $k$ -space is acquired at each time point, the data recovery should include the information from some previous adjacent time frames and the latest acquired one to obtain full  $k$ -space data and then convert to images. The technique is also called moving average or sliding window reconstruction. However, it is not efficient to update the  $k$ -space uniformly due to most of the useful information locating on central  $k$ -space. Hence, Keyhole pushes the idea into a limit, where the peripheral  $k$ -space data are only acquired once at the beginning or the end of the dynamic scan and the center is refreshed at every time frame. BRISK and TWIST are the compromise between the two extreme cases. They divide  $k$ -space into different zones, where the central one and the one of the peripherals are alternatively updated (Figure 7).

These techniques refill the missing  $k$ -space using the temporally closest data. The process is equal to the dynamic images interpolation, which would smooth the dynamic

response curves similar to applying low-pass filters. Hence, some high temporal frequency information would get lost, so that the acceleration rate and the view-sharing methods should be carefully chosen depending on different applications. However, they did not really take the advantages from the additional dimension, time, for acceleration, so more sophisticated approaches were developed.

**3.2.2. Unaliasing by Fourier-Encoding the Overlaps Using the Temporal Dimension (UNFOLD).** UNFOLD [113] was the very early technique taking the advantages of spatial and temporal information for acceleration. It converted the acquired  $k$ -space data with temporal information ( $k$ - $t$  space) into  $x$ - $f$  space to observe the dynamic patterns, so that we could more effectively exploit the  $x$ - $f$  space for higher acceleration rates (Figure 8(a)). The “ $x$ ” in  $x$ - $f$  space represents the image domain, not exactly the  $x$ -axis, and generally the undersampled  $k$ -space is along the phase-encoding direction, which is usually the  $y$ -axis. The concept of UNFOLD is similar to 2D CAIPIRINHA [21], where the images become less aliasing by modifying the sampling strategy (Figure 8(b) and Figure 3 in [21]). The major difference is the second acceleration dimension of 2D CAIPIRHNA along slice encoding direction and that of UNFOLD temporally. However, a prerequisite of UNFOLD technique is that

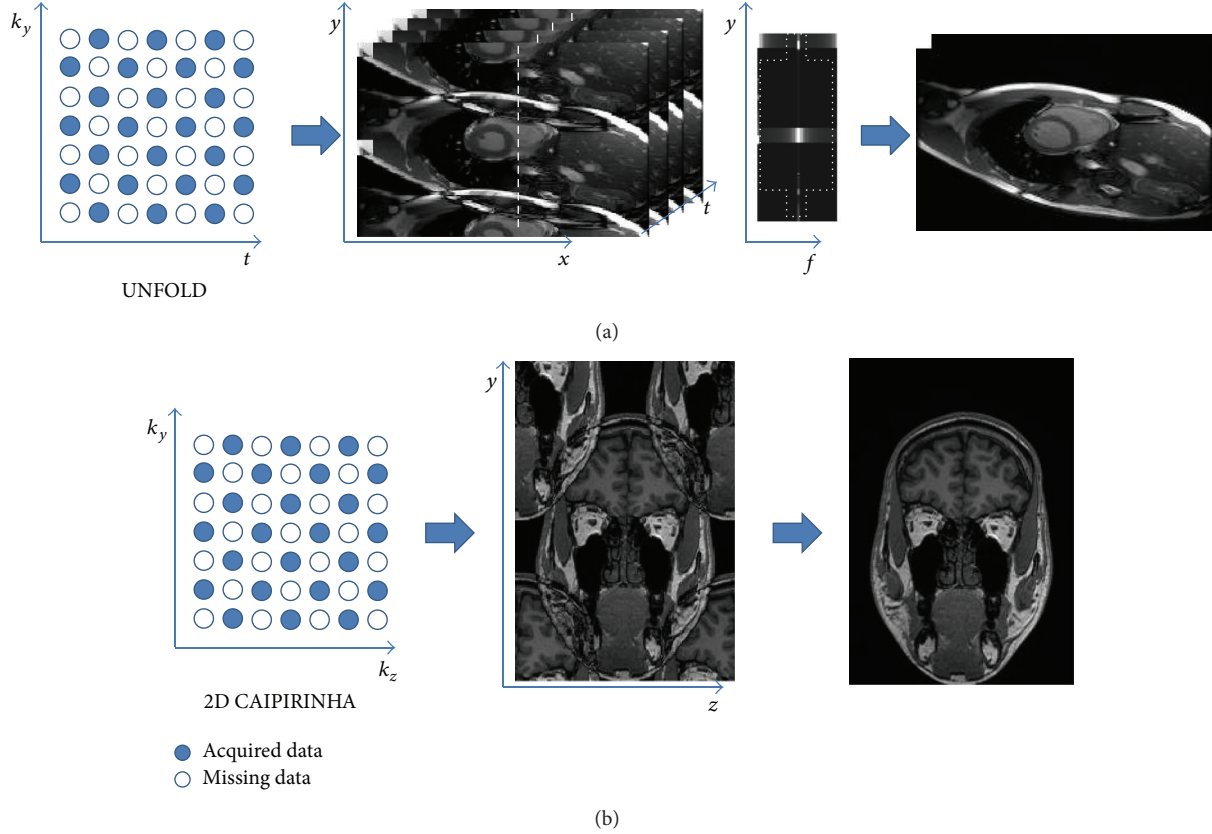


FIGURE 8: The similarity and difference between UNFOLD and 2D CAIPIRINHA. Both techniques used two-dimensional accelerations, where the second domain in UNFOLD is time and that in 2D CAIPIRINHA is the slice encoding direction ( $k_z$ ). (a) UNFOLD transformed the dynamic aliased images to the  $x$ - $f$  space, where the information was more concentrate. The  $x$ - $f$  aliasing patterns could be shifted by changing the sampling patterns. Hence, the space was suitable to reduce the aliasing patterns and reconstruct the images by applying appropriate filters (the dashed cross region). (b) 2D CAIPIRINHA also changed the sampling patterns to shift the aliased images, which could reduce the  $g$ -factor and improve the SNR in reconstruction. The performance would be better than that in conventional 2D parallel imaging techniques [21].

the aliased  $x$ - $f$  space should not overlap in major frequency components. Then the aliasing artifacts could be removed in  $x$ - $f$  space by applying appropriate filters to fully reconstruct the images.

The limitation of acceleration rate in UNFOLD depends on different applications. The larger the portion of dynamic region within an FOV, the less the acceleration rate achieve. Hence, the acquisition time of fMRI could be more efficiently reduced than that of cardiac imaging.

**3.2.3.  $k$ - $t$  Family.** Depending on the concept from UNFOLD technique,  $k$ - $t$  BLAST and  $k$ - $t$  SENSE [145] were developed to enhance the robustness of the achievable acceleration by acquiring the central part of  $k$ -space at the beginning as the training data before the undersampled dynamic  $k$ -space acquisition. Hence, the whole acquisition is divided into two parts: the training scan, providing the low spatial resolution images without aliasing artifacts, and the undersampled scan, containing the full spatial and temporal information but with fold-over artifacts.  $k$ - $t$  BLAST and  $k$ - $t$  SENSE use the training data as prior information to understand how to resolve the aliasing patterns and to obtain the fully-reconstructed

dynamic images.  $k$ - $t$  SENSE, combining the parallel imaging technology, was an extension of  $k$ - $t$  BLAST, and both technologies reconstruct the images in  $x$ - $f$  space (Figure 9). Because  $k$ - $t$  methods introduce temporal information to increase the degree of freedom, their performance, especially in noise reduction of the reconstructed images could be much better than the traditional parallel imaging at high acceleration factors.

$k$ - $t$  GRAPPA [146, 147] reconstruct the data directly in  $k$ - $t$  space without transforming to  $x$ - $f$  space. ACS is acquired to determine the weightings for  $k$ -space reconstruction as GRAPPA does.  $k$ - $t^2$  GRAPPA [148] is an extension of the series and scatters the central  $k$ -space acquisition into different time frames. Hence, the reconstruction should firstly use  $k$ - $t$  GRAPPA to refill the undersampled central  $k$ -space and then to restore the full  $k$ -space data.  $k$ - $t$  PCA [103] is another kind of extension, which reconstructed the images using principal components (PC), instead of temporal frequency. Thus, it uses  $x$ -PC space for data reconstruction. Taking the advantages of mathematical properties of principal component analysis (PCA),  $k$ - $t$  PCA could even reduce the artifacts for higher acceleration rates.

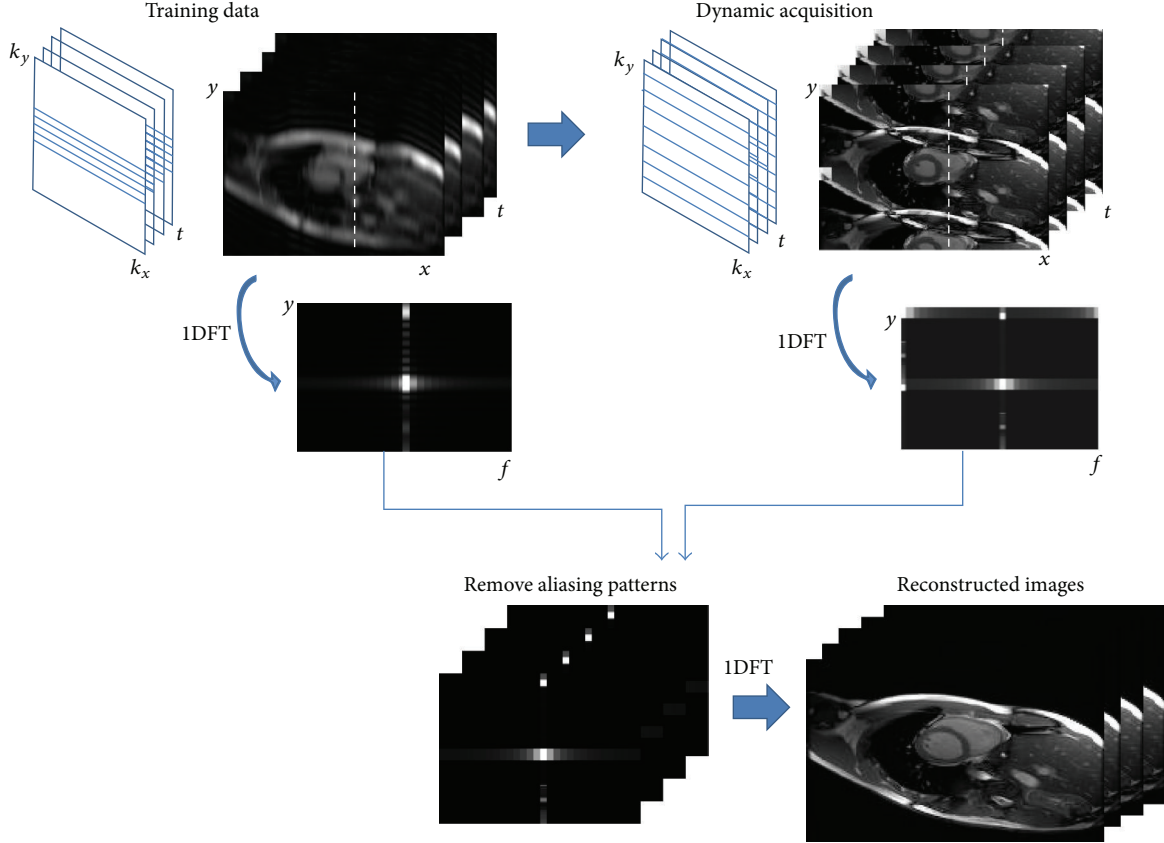


FIGURE 9:  $k\text{-}t$  BLAST for dynamic imaging acceleration. The data acquisition is divided into two parts, training data (low resolution images) and dynamic acquisition (undersampled  $k$ -space images). The  $x\text{-}f$  space of the training data is used to preliminarily understand the features of the dynamic scan, and then the undersampled data could be involved for image reconstruction without applying any determinate filters. An alternative method was to embed the central  $k$ -line acquisition in every time frame and the data were split into two parts as the description above when doing image reconstruction.

**3.3. Compressed Sensing (CS).** CS [62] was first proposed in the field of information theory and is applied to MRI with the sampling rate beyond the Nyquist criterion. The sampling number could be much reduced in CS, as a result, the acquisition time becomes much shorter. There are three basic requirements for the CS approach, including the sparsity in a known transform domain, the incoherence of the undersampled artifacts and the nonlinear reconstruction.

Most of the MR images are not sparse from image point of view except angiography. However, sparsity is the most fundamental requirement to represent whether the data are compressible or not. Many different kinds of images are sparse in discrete cosine transform (DCT) and wavelet transform, which are the cores of image or video compression technologies. Medical images share the same property of sparsity, so that the DCT and the wavelet transform are both good for brain and angiogram which were capable to use only 5% to 10% largest transform coefficients for reconstruction [149]. Conventional undersampled  $k$ -space was coherent, that is, the sampled  $k$ -space was skipped periodically and the reconstructed images resulted in regular aliasing patterns. On the other hand, the incoherent undersampled  $k$ -space

would lead to the noise-like artifacts, so the dealiasing problems could be converted to a denoise problem. The two aliasing patterns show significant differences in Figure 1 of [150]. Since the sampling strategy has destroyed the linear transformation relations between two domains ( $k$ -space and image), some nonlinear reconstruction methods should be applied to iteratively approach the solutions, such as conjugate gradient method [151].

The undersamples along frequency encoding direction could not actually reduce the scan time in MRI and it was not feasible to achieve the fully randomized sampled  $k$ -space. Several encoding schemes, such as radial and spiral [110, 152, 153], could approach the variable-density sampling, which results in more incoherent aliasing patterns. For morphological or static images, 2D imaging acquisition is not preferred because the randomly undersampled dimension is limited. It is more attractive on three-dimensional imaging or dynamic images, because there are two nonfrequency encoding planes ( $k_y\text{-}k_z$  or  $k_y\text{-}t$ ), which would achieve random undersampling more easily. However, one of the features of  $k$ -space should be taken into consideration when doing randomized undersampling: the energy of  $k$ -space is concentrated in

the central region. Hence, the central  $k$ -space should be less undersampled than peripheral regions to keep the image quality and to accelerate the data acquisition more efficiently.

CS has been demonstrated in various applications with the combination of parallel imaging techniques in static images [149, 154, 155]. Furthermore, there were also technologies developed with the combination of the concepts from  $k$ - $t$  BLAST and incoherent sampling, such as  $k$ - $t$  SPARSE-SENSE [156, 157] and  $k$ - $t$  FOCUS [158], and dynamic MRI using CS was applied to cardiac imaging [159, 160] and fMRI [161, 162]. However, the computational time is still too long for daily clinical use. Thus, the improvement in algorithms and computer hardware, which shorten the postprocessing time, would bring CS more feasible.

**3.4. Summary.** We would like to summarize the MR acceleration technologies so that it would be easier to distinguish the differences and understand their feasibilities.

- (i) Parallel imaging uses the multiple-channel surface-arrayed coils to reduce the  $k$ -space sampling. The reconstruction methods are divided into GRAPPA and SENSE two families, which are commonly used in clinical routines.
- (ii) Multislice excitation, the extension of parallel imaging, could be divided into frequency modulation (MB) and phase modulation (CAIPIRINHA) for the acceleration along the slice direction with better performance.
- (iii) Temporal domain is involved in dynamic acceleration methods, such as UNFOLD and  $k$ - $t$  BLAST. UNFOLD applies an appropriate filter to remove the aliasing patterns, where  $k$ - $t$  BLAST does it via the low-resolution training data at the beginning of the dynamic acquisition.
- (iv) Compressed sensing MRI brings the acquisition beyond the Nyquist criterion limitation both in static and dynamic images.
- (v) All the technologies above are compatible to parallel imaging techniques.

With the appropriate combination of these techniques, we could foresee the huge leap in MR acceleration in the near future.

## 4. Conclusion

CT dose consideration and MR acquisition could be viewed as the two obstacles during their development. We have seen many techniques developed to solve the problems, to broaden their applications, and to push the diagnostic clinical imaging into molecular imaging level. Besides, their intrinsic superiorities are kept to measure the physiological parameters, such as blood flow, blood volume, and  $T_1/T_2$  parameters or diffusion imaging specified by MRI. The information has been investigated for oncology imaging, cancer treatment followup, neurodegenerative diseases, and so on. Due to the growing knowledge of the human multiple “-omes,” such as

genome, proteome, and metabolome, more information is included to analyze the correlation between the -omic data and the clinical imaging. It potentially does great benefits to the early detection, staging, and treatment response of the diseases. As the personal information is involved in the clinical procedures, it comes closer to realize the personalized medicine. The development strongly depends on the conjunction between various fields, including diagnostic imaging, nanotechnologies, and -omics database analysis.

## Conflict of Interests

The authors declare that there is no conflict of interests regarding the publication of this paper.

## References

- [1] N. G. Costouros, D. Lorang, Y. Zhang et al., “Microarray gene expression analysis of murine tumor heterogeneity defined by dynamic contrast-enhanced MRI,” *Molecular Imaging*, vol. 1, no. 3, pp. 301–308, 2002.
- [2] S. Guccione, Y.-S. Yang, G. Shi, D. Y. Lee, K. C. P. Li, and M. D. Bednarski, “Functional genomics guided with MR imaging: mouse tumor model study,” *Radiology*, vol. 228, no. 2, pp. 560–568, 2003.
- [3] Y.-S. Yang, S. Guccione, and M. D. Bednarski, “Comparing genomic and histologic correlations to radiographic changes in tumors: a murine SCC VII model study,” *Academic Radiology*, vol. 10, no. 10, pp. 1165–1175, 2003.
- [4] S. K. Hobbs, G. Shi, R. Homer, G. Harsh, S. W. Atlas, and M. D. Bednarski, “Magnetic resonance image-guided proteomics of human glioblastoma multiforme,” *Journal of Magnetic Resonance Imaging*, vol. 18, no. 5, pp. 530–536, 2003.
- [5] M. D. Kuo, J. Gollub, C. B. Sirlin, C. Ooi, and X. Chen, “Radiogenomic analysis to identify imaging phenotypes associated with drug response gene expression programs in hepatocellular carcinoma,” *Journal of Vascular and Interventional Radiology*, vol. 18, no. 7, pp. 821–830, 2007.
- [6] E. Segal, C. B. Sirlin, C. Ooi et al., “Decoding global gene expression programs in liver cancer by noninvasive imaging,” *Nature Biotechnology*, vol. 25, no. 6, pp. 675–680, 2007.
- [7] M. Diehn, C. Nardini, D. S. Wang et al., “Identification of non-invasive imaging surrogates for brain tumor gene-expression modules,” *Proceedings of the National Academy of Sciences of the United States of America*, vol. 105, no. 13, pp. 5213–5218, 2008.
- [8] E. Segal, M. Shapira, A. Regev et al., “Module networks: identifying regulatory modules and their condition-specific regulators from gene expression data,” *Nature Genetics*, vol. 34, no. 2, pp. 166–176, 2003.
- [9] N. J. Serkova and M. S. Brown, “Quantitative analysis in magnetic resonance spectroscopy: from metabolic profiling to *in vivo* biomarkers,” *Bioanalysis*, vol. 4, no. 3, pp. 321–341, 2012.
- [10] S. Tiziani, Y. Kang, R. Harjanto et al., “Metabolomics of the tumor microenvironment in pediatric acute lymphoblastic leukemia,” *PLoS ONE*, vol. 8, no. 12, Article ID e82859, 2013.
- [11] G. Hassan-Smith, G. R. Wallace, M. R. Douglas, and A. J. Sinclair, “The role of metabolomics in neurological disease,” *Journal of Neuroimmunology*, vol. 248, no. 1-2, pp. 48–52, 2012.
- [12] E.-M. Spur, E. A. Decelle, and L. L. Cheng, “Metabolomic imaging of prostate cancer with magnetic resonance spectroscopy

- and mass spectrometry,” *European Journal of Nuclear Medicine and Molecular Imaging*, vol. 40, supplement 1, pp. 60–71, 2013.
- [13] R. Popovtzer, A. Agrawal, N. A. Kotov et al., “Targeted gold nanoparticles enable molecular CT imaging of cancer,” *Nano Letters*, vol. 8, no. 12, pp. 4593–4596, 2008.
- [14] T. Reuveni, M. Motiei, Z. Romman, A. Popovtzer, and R. Popovtzer, “Targeted gold nanoparticles enable molecular CT imaging of cancer: an in vivo study,” *International Journal of Nanomedicine*, vol. 6, pp. 2859–2864, 2011.
- [15] O. Rabin, J. M. Perez, J. Grimm, G. Wojtkiewicz, and R. Weissleder, “An X-ray computed tomography imaging agent based on long-circulating bismuth sulphide nanoparticles,” *Nature Materials*, vol. 5, no. 2, pp. 118–122, 2006.
- [16] B. Cohen, K. Ziv, V. Plaks et al., “MRI detection of transcriptional regulation of gene expression in transgenic mice,” *Nature Medicine*, vol. 13, no. 4, pp. 498–503, 2007.
- [17] A. A. Gilad, M. T. McMahon, P. Walczak et al., “Artificial reporter gene providing MRI contrast based on proton exchange,” *Nature Biotechnology*, vol. 25, no. 2, pp. 217–219, 2007.
- [18] C. H. Liu, S. Huang, J. Cui et al., “MR contrast probes that trace gene transcripts for cerebral ischemia in live animals,” *FASEB Journal*, vol. 21, no. 11, pp. 3004–3015, 2007.
- [19] A. Y. Louie, M. M. Hüber, E. T. Ahrens et al., “In vivo visualization of gene expression using magnetic resonance imaging,” *Nature Biotechnology*, vol. 18, no. 3, pp. 321–325, 2000.
- [20] J. B. Weaver, “Simultaneous multislice acquisition of MR images,” *Magnetic Resonance in Medicine*, vol. 8, no. 3, pp. 275–284, 1988.
- [21] F. A. Breuer, M. Blaimer, M. F. Mueller et al., “Controlled aliasing in volumetric parallel imaging (2D CAIPIRINHA),” *Magnetic Resonance in Medicine*, vol. 55, no. 3, pp. 549–556, 2006.
- [22] S. A. Graham, D. J. Moseley, J. H. Siewersden, and D. A. Jaffray, “Compensators for dose and scatter management in cone-beam computed tomography,” *Medical Physics*, vol. 34, no. 7, pp. 2691–2703, 2007.
- [23] T. L. Toth, “Dose reduction opportunities for CT scanners,” *Pediatric Radiology*, vol. 32, no. 4, pp. 261–267, 2002.
- [24] C. H. McCollough, A. N. Primak, O. Saba et al., “Dose performance of a 64-channel dual-source CT scanner,” *Radiology*, vol. 243, no. 3, pp. 775–784, 2007.
- [25] S. S. Hsieh and N. J. Pelc, “The feasibility of a piecewise-linear dynamic bowtie filter,” *Medical Physics*, vol. 40, no. 3, Article ID 031910, 2013.
- [26] T. P. Szczykutowicz and C. A. Mistretta, “Design of a digital beam attenuation system for computed tomography: part I. System design and simulation framework,” *Medical Physics*, vol. 40, no. 2, Article ID 021905, 2013.
- [27] K. Perisinakis, A. E. Papadakis, and J. Damilakis, “The effect of X-ray beam quality and geometry on radiation utilization efficiency in multidetector CT imaging,” *Medical Physics*, vol. 36, no. 4, pp. 1258–1266, 2009.
- [28] A. Tzedakis, J. Damilakis, K. Perisinakis, J. Stratidakis, and N. Gourtsoyiannis, “The effect of z overscanning on patient effective dose from multidetector helical computed tomography examinations,” *Medical Physics*, vol. 32, no. 6, pp. 1621–1629, 2005.
- [29] A. Tzedakis, J. Damilakis, K. Perisinakis, A. Karantanas, S. Karabekios, and N. Gourtsoyiannis, “Influence of z overscanning on normalized effective doses calculated for pediatric patients undergoing multidetector CT examinations,” *Medical Physics*, vol. 34, no. 4, pp. 1163–1175, 2007.
- [30] J. A. Christner, V. A. Zavaletta, C. D. Eusemann, A. I. Walz-Flannigan, and C. H. McCollough, “Dose reduction in helical CT: dynamically adjustable z-axis X-ray beam collimation,” *American Journal of Roentgenology*, vol. 194, no. 1, pp. W49–W55, 2010.
- [31] P. D. Deak, O. Langner, M. Lell, and W. A. Kalender, “Effects of adaptive section collimation on patient radiation dose in multisegment spiral CT,” *Radiology*, vol. 252, no. 1, pp. 140–147, 2009.
- [32] P. M. Shikhaliev, T. Xu, and S. Molloj, “Photon counting computed tomography: concept and initial results,” *Medical Physics*, vol. 32, no. 2, pp. 427–436, 2005.
- [33] X. Wang, A. Zamyatin, and D. Shi, “Dose reduction potential with photon counting computed tomography,” in *Medical Imaging: Physics of Medical Imaging*, N. J. Pelc, R. M. Nishikawa, and B. R. Whiting, Eds., vol. 8313 of *Proceedings of SPIE*, International Society for Optics and Photonics, February 2012.
- [34] L. F. N. D. Carramate, F. Nachtrab, M. Firsching et al., “Energy resolving CT systems using Medipix2 and MHSP detectors,” *Journal of Instrumentation*, vol. 8, no. 03, Article ID C03022, 2013.
- [35] J. Giersch, D. Niederlöhner, and G. Anton, “The influence of energy weighting on X-ray imaging quality,” *Nuclear Instruments and Methods in Physics Research A*, vol. 531, no. 1–2, pp. 68–74, 2004.
- [36] K. S. Kalluri, M. Mahd, and S. J. Glick, “Investigation of energy weighting using an energy discriminating photon counting detector for breast CT,” *Medical Physics*, vol. 40, no. 8, Article ID 081923, 2013.
- [37] L. Wielopolski and R. P. Gardner, “Prediction of the pulse-height spectral distortion caused by the peak pile-up effect,” *Nuclear Instruments and Methods*, vol. 133, no. 2, pp. 303–309, 1976.
- [38] X. Wang, D. Meier, S. Mikkelsen et al., “MicroCT with energy-resolved photon-counting detectors,” *Physics in Medicine and Biology*, vol. 56, no. 9, pp. 2791–2816, 2011.
- [39] A. Mohammadi, M. Baba, M. Nakhostin, H. Ohuchi, and M. Abe, “Compton spectroscopy for rotation-mode computed tomography,” *Journal of X-Ray Science and Technology*, vol. 20, no. 2, pp. 131–140, 2012.
- [40] J. Bennett, A. Opie, Q. Xu et al., “Hybrid spectral micro-CT: system design, implementation & preliminary results,” *IEEE Transactions on Bio-Medical Engineering*, vol. 61, no. 2, pp. 246–253, 2014.
- [41] W. A. Kalender, H. Wolf, and C. Suess, “Dose reduction in CT by anatomically adapted tube current modulation. II. Phantom measurements,” *Medical Physics*, vol. 26, no. 11, pp. 2248–2253, 1999.
- [42] J. R. Haaga, F. Miraldi, and W. MacIntyre, “The effect of mAs variation upon computed tomography image quality as evaluated by in vivo and in vitro studies,” *Radiology*, vol. 138, no. 2, pp. 449–454, 1981.
- [43] M. K. Kalra, M. M. Maher, T. L. Toth et al., “Techniques and applications of automatic tube current modulation for CT,” *Radiology*, vol. 233, no. 3, pp. 649–657, 2004.
- [44] H. Greeß, H. Wolf, U. Baum, W. A. Kalender, and W. Bautz, “Dose reduction in computed tomography by means of modulation of tube current according to anything: first clinical results,” *RoFo*, vol. 170, no. 3, pp. 246–250, 1999.

- [45] M. Sderberg and M. Gunnarsson, "Automatic exposure control in computed tomography an evaluation of systems from different manufacturers," *Acta Radiologica*, vol. 51, no. 6, pp. 625–634, 2010.
- [46] W. Huda, E. M. Scalzetti, and G. Levin, "Technique factors and image quality as functions of patient weight at abdominal CT," *Radiology*, vol. 217, no. 2, pp. 430–435, 2000.
- [47] B. B. Ertl-Wagner, R.-T. Hoffmann, R. Bruning et al., "Multi-detector row CT angiography of the brain at various kilovoltage settings," *Radiology*, vol. 231, no. 2, pp. 528–535, 2004.
- [48] Y. Funama, K. Awai, Y. Nakayama et al., "Radiation dose reduction without degradation of low-contrast detectability at abdominal multislice CT with a low-tube voltage technique: phantom study," *Radiology*, vol. 237, no. 3, pp. 905–910, 2005.
- [49] B. Wintersperger, T. Jakobs, P. Herzog et al., "Aorto-iliac multidetector-row CT angiography with low kV settings: improved vessel enhancement and simultaneous reduction of radiation dose," *European Radiology*, vol. 15, no. 2, pp. 334–341, 2005.
- [50] C. Schueler-Weidekamm, C. M. Schaefer-Prokop, M. Weber, C. J. Herold, and M. Prokop, "CT angiography of pulmonary arteries to detect pulmonary embolism: improvement of vascular enhancement with low kilovoltage settings," *Radiology*, vol. 241, no. 3, pp. 899–907, 2006.
- [51] A. Waaijer, M. Prokop, B. K. Velthuis, C. J. G. Bakker, G. A. P. De Kort, and M. S. Van Leeuwen, "Circle of Willis at CT angiography: dose reduction and image quality—reducing tube voltage and increasing tube current settings," *Radiology*, vol. 242, no. 3, pp. 832–839, 2007.
- [52] Y. Nakayama, K. Awai, Y. Funama et al., "Abdominal CT with low tube voltage: preliminary observations about radiation dose, contrast enhancement, image quality, and noise," *Radiology*, vol. 237, no. 3, pp. 945–951, 2005.
- [53] J. Nuyts, B. De Man, P. Dupont, M. Defrise, P. Suetens, and L. Mortelmans, "Iterative reconstruction for helical CT: a simulation study," *Physics in Medicine and Biology*, vol. 43, no. 4, pp. 729–737, 1998.
- [54] J.-B. Thibault, K. D. Sauer, C. A. Bouman, and J. Hsieh, "A three-dimensional statistical approach to improved image quality for multislice helical CT," *Medical Physics*, vol. 34, no. 11, pp. 4526–4544, 2007.
- [55] I. A. Elbakri and J. A. Fessler, "Statistical image reconstruction for polyenergetic X-ray computed tomography," *IEEE Transactions on Medical Imaging*, vol. 21, no. 2, pp. 89–99, 2002.
- [56] A. K. Hara, R. G. Paden, A. C. Silva, J. L. Kujak, H. J. Lawder, and W. Pavlicek, "Iterative reconstruction technique for reducing body radiation dose at CT: feasibility study," *American Journal of Roentgenology*, vol. 193, no. 3, pp. 764–771, 2009.
- [57] J. S. Kole and F. J. Beekman, "Evaluation of accelerated iterative X-ray CT image reconstruction using floating point graphics hardware," *Physics in Medicine and Biology*, vol. 51, no. 4, pp. 875–889, 2006.
- [58] F. Xu and K. Mueller, "Real-time 3D computed tomographic reconstruction using commodity graphics hardware," *Physics in Medicine and Biology*, vol. 52, no. 12, article 006, pp. 3405–3419, 2007.
- [59] G. C. Sharp, N. Kandasamy, H. Singh, and M. Folkert, "GPU-based streaming architectures for fast cone-beam CT image reconstruction and demons deformable registration," *Physics in Medicine and Biology*, vol. 52, no. 19, article 003, pp. 5771–5783, 2007.
- [60] H. Kudo, T. Suzuki, and E. A. Rashed, "Image reconstruction for sparse-view CT and interior CT—introduction to compressed sensing and differentiated backprojection," *Quantitative Imaging in Medicine and Surgery*, vol. 3, no. 3, pp. 147–161, 2013.
- [61] E. J. Candès, J. Romberg, and T. Tao, "Robust uncertainty principles: exact signal reconstruction from highly incomplete frequency information," *IEEE Transactions on Information Theory*, vol. 52, no. 2, pp. 489–509, 2006.
- [62] D. L. Donoho, "Compressed sensing," *IEEE Transactions on Information Theory*, vol. 52, no. 4, pp. 1289–1306, 2006.
- [63] G.-H. Chen, J. Tang, and S. Leng, "Prior Image Constrained Compressed Sensing (PICCS): a method to accurately reconstruct dynamic CT images from highly undersampled projection data sets," *Medical Physics*, vol. 35, no. 2, pp. 660–663, 2008.
- [64] E. Y. Sidky and X. Pan, "Image reconstruction in circular cone-beam computed tomography by constrained, total-variation minimization," *Physics in Medicine and Biology*, vol. 53, no. 17, pp. 4777–4807, 2008.
- [65] K. Choi, J. Wang, L. Zhu, T.-S. Suh, S. Boyd, and L. Xing, "Compressed sensing based cone-beam computed tomography reconstruction with a first-order method," *Medical Physics*, vol. 37, no. 9, pp. 5113–5125, 2010.
- [66] L. Ritschl, F. Bergner, C. Fleischmann, and M. Kachelriess, "Improved total variation-based CT image reconstruction applied to clinical data," *Physics in Medicine and Biology*, vol. 56, no. 6, pp. 1545–1561, 2011.
- [67] E. Y. Sidky, C.-M. Kao, and X. Pan, "Accurate image reconstruction from few-views and limited-angle data in divergent-beam CT," *Journal of X-Ray Science and Technology*, vol. 14, no. 2, pp. 119–139, 2006.
- [68] F. Noo, R. Clackdoyle, and J. D. Pack, "A two-step Hilbert transform method for 2D image reconstruction," *Physics in Medicine and Biology*, vol. 49, no. 17, pp. 3903–3923, 2004.
- [69] X. Pan, Y. Zou, and D. Xia, "Image reconstruction in peripheral and central regions-of-interest and data redundancy," *Medical Physics*, vol. 32, no. 3, pp. 673–684, 2005.
- [70] K. Ogawa, M. Nakajima, and S. Yuta, "A reconstruction algorithm from truncated projections," *IEEE Transactions on Medical Imaging*, vol. 3, no. 1, pp. 34–40, 1984.
- [71] B. Ohnesorge, T. Flohr, K. Schwarz, J. P. Heiken, and K. T. Bae, "Efficient correction for CT image artifacts caused by objects extending outside the scan field of view," *Medical Physics*, vol. 27, no. 1, pp. 39–46, 2000.
- [72] S. Kappler and S. Wirth, "Comparison Of dual-kVp and dual-layer CT in simulations and real CT system measurements," in *Proceedings of the IEEE Nuclear Science Symposium Conference Record (NSS/MIC '08)*, pp. 4828–4831, IEEE, October 2008.
- [73] L. Goshen, J. Sosna, R. Carmi, G. Kafri, I. Iancu, and A. Altman, "An iodine-calcium separation analysis and virtually non-contrasted image generation obtained with single source dual energy MDCT," in *Proceedings of the IEEE Nuclear Science Symposium Conference Record (NSS/MIC '08)*, pp. 3868–3870, IEEE, October 2008.
- [74] Y. Zou and M. D. Silver, "Analysis of fast kV-switching in dual energy CT using a pre-reconstruction decomposition technique," in *Medical Imaging: Physics of Medical Imaging*, vol. 6913 of *Proceedings of SPIE*, International Society for Optics and Photonics, February 2008.
- [75] T. R. C. Johnson, B. Krauss, M. Sedlmair et al., "Material differentiation by dual energy CT: initial experience," *European Radiology*, vol. 17, no. 6, pp. 1510–1517, 2007.

- [76] T. G. Flohr, H. Bruder, K. Stierstorfer, M. Petersilka, B. Schmidt, and C. H. McCollough, "Image reconstruction and image quality evaluation for a dual source CT scanner," *Medical Physics*, vol. 35, no. 12, pp. 5882–5897, 2008.
- [77] A. N. Primak, J. C. R. Giraldo, X. Liu, L. Yu, and C. H. McCollough, "Improved dual-energy material discrimination for dual-source CT by means of additional spectral filtration," *Medical Physics*, vol. 36, no. 4, pp. 1359–1369, 2009.
- [78] M. Karçalıncaba and A. Aktaş, "Dual-energy CT revisited with multidetector CT: review of principles and clinical applications," *Diagnostic and Interventional Radiology*, vol. 17, no. 3, pp. 181–194, 2011.
- [79] T. Kraśnicki, P. Podgóński, M. Guziński et al., "Novel clinical applications of dual energy computed tomography," *Advances in Clinical and Experimental Medicine*, vol. 21, no. 6, pp. 831–841, 2012.
- [80] T. Heye, R. C. Nelson, L. M. Ho, D. Marin, and D. T. Boll, "Dual-energy CT applications in the abdomen," *American Journal of Roentgenology*, vol. 199, supplement 5, pp. 64–70, 2012.
- [81] H. Scheffel, P. Stolzmann, T. Frauenfelder et al., "Dual-energy contrast-enhanced computed tomography for the detection of urinary stone disease," *Investigative Radiology*, vol. 42, no. 12, pp. 823–829, 2007.
- [82] N. Takahashi, R. P. Hartman, T. J. Vrtiska et al., "Dual-energy CT iodine-subtraction virtual unenhanced technique to detect urinary stones in an iodine-filled collecting system: a phantom study," *American Journal of Roentgenology*, vol. 190, no. 5, pp. 1169–1173, 2008.
- [83] G. Ascenti, A. Mileto, M. Gaeta, A. Blandino, S. Mazzotti, and E. Scribano, "Single-phase dual-energy CT urography in the evaluation of haematuria," *Clinical Radiology*, vol. 68, no. 2, pp. 87–94, 2013.
- [84] A. Graser, T. R. C. Johnson, E. M. Hecht et al., "Dual-energy CT in patients suspected of having renal masses: can virtual nonenhanced images replace true nonenhanced images?" *Radiology*, vol. 252, no. 2, pp. 433–440, 2009.
- [85] A. Graser, C. R. Becker, M. Staehler et al., "Single-phase dual-energy CT allows for characterization of renal masses as benign or malignant," *Investigative Radiology*, vol. 45, no. 7, pp. 399–405, 2010.
- [86] S. H. Lee, J. Hur, Y. J. Kim, H.-J. Lee, Y. J. Hong, and B. W. Choi, "Additional value of dual-energy CT to differentiate between benign and malignant mediastinal tumors: an initial experience," *European Journal of Radiology*, vol. 82, no. 11, pp. 2043–2049, 2013.
- [87] G. Schmid-Bindert, T. Henzler, T. Q. Chu et al., "Functional imaging of lung cancer using dual energy CT: how does iodine related attenuation correlate with standardized uptake value of 18FDG-PET-CT?" *European Radiology*, vol. 22, no. 1, pp. 93–103, 2012.
- [88] M. Meyer, P. Hohenberger, P. Apfaltner et al., "CT-based response assessment of advanced gastrointestinal stromal tumor: dual energy CT provides a more predictive imaging biomarker of clinical benefit than RECIST or Choi criteria," *European Journal of Radiology*, vol. 82, no. 6, pp. 923–928, 2013.
- [89] K. A. Miles and M. R. Griffiths, "Perfusion CT: a worthwhile enhancement?" *British Journal of Radiology*, vol. 76, no. 904, pp. 220–231, 2003.
- [90] A. R. Kambadakone and D. V. Sahani, "Body perfusion CT: technique, clinical applications, and advances," *Radiologic Clinics of North America*, vol. 47, no. 1, pp. 161–178, 2009.
- [91] C.-J. Sun, C. Li, H.-B. Lv et al., "Comparing CT perfusion with oxygen partial pressure in a rabbit VX2 soft-tissue tumor model," *Journal of Radiation Research*, vol. 55, no. 1, pp. 183–190, 2014.
- [92] G.-L. Ma, R.-J. Bai, H.-J. Jiang et al., "Early changes of hepatic hemodynamics measured by functional CT perfusion in a rabbit model of liver tumor," *Hepatobiliary & Pancreatic Diseases International*, vol. 11, no. 4, pp. 407–411, 2012.
- [93] R. Jain, "Perfusion CT imaging of brain tumors: an overview," *American Journal of Neuroradiology*, vol. 32, no. 9, pp. 1570–1577, 2011.
- [94] D. Arandjic, F. Bonutti, E. Biasizzo et al., "Radiation doses in cerebral perfusion computed tomography: patient and phantom study," *Radiation Protection Dosimetry*, vol. 154, no. 4, pp. 459–464, 2013.
- [95] N. Negi, T. Yoshikawa, Y. Ohno et al., "Hepatic CT perfusion measurements: a feasibility study for radiation dose reduction using new image reconstruction method," *European Journal of Radiology*, vol. 81, no. 11, pp. 3048–3054, 2012.
- [96] R. Krissak, C. A. Mistretta, T. Henzler et al., "Noise reduction and image quality improvement of low dose and ultra low dose brain perfusion CT by HYPR-LR processing," *PLoS ONE*, vol. 6, no. 2, Article ID e17098, 2011.
- [97] M. Supanich, Y. Tao, B. Nett et al., "Radiation dose reduction in time-resolved CT angiography using highly constrained back projection reconstruction," *Physics in Medicine and Biology*, vol. 54, no. 14, pp. 4575–4593, 2009.
- [98] L. He, B. Orten, S. Do et al., "A spatio-temporal deconvolution method to improve perfusion CT quantification," *IEEE Transactions on Medical Imaging*, vol. 29, no. 5, pp. 1182–1191, 2010.
- [99] H. Yu, S. Zhao, E. A. Hoffman, and G. Wang, "Ultra-low dose lung CT perfusion regularized by a previous scan," *Academic Radiology*, vol. 16, no. 3, pp. 363–373, 2009.
- [100] J. J. S. Shankar, C. Lum, and M. Sharma, "Whole-brain perfusion imaging with 320-MDCT scanner: reducing radiation dose by increasing sampling interval," *American Journal of Roentgenology*, vol. 195, no. 5, pp. 1183–1186, 2010.
- [101] A. Tognolini, R. Schor-Bardach, O. S. Piankh, C. J. Wilcox, V. Raptopoulos, and S. N. Goldberg, "Body tumor CT perfusion protocols: optimization of acquisition scan parameters in a rat tumor model," *Radiology*, vol. 251, no. 3, pp. 712–720, 2009.
- [102] P. C. Lauterbur, "Image formation by induced local interactions: examples employing nuclear magnetic resonance," *Nature*, vol. 242, no. 5394, pp. 190–191, 1973.
- [103] H. Pedersen, S. Kozerke, S. Ringgaard, K. Nehrke, and Y. K. Won, "K-t PCA: temporally constrained k-t BLAST reconstruction using principal component analysis," *Magnetic Resonance in Medicine*, vol. 62, no. 3, pp. 706–716, 2009.
- [104] L. Ge, A. Kino, M. Griswold, C. Mistretta, J. C. Carr, and D. Li, "Myocardial perfusion MRI with sliding-window conjugate-gradient HYPR," *Magnetic Resonance in Medicine*, vol. 62, no. 4, pp. 835–839, 2009.
- [105] B. Jung, M. Honal, J. Hennig, and M. Markl, "k-t-space accelerated myocardial perfusion," *Journal of Magnetic Resonance Imaging*, vol. 28, no. 5, pp. 1080–1085, 2008.
- [106] P. Kellman, J. A. Derbyshire, K. O. Agyeman, E. R. McVeigh, and A. E. Arai, "Extended coverage first-pass perfusion imaging using slice-interleaved TSENSE," *Magnetic Resonance in Medicine*, vol. 51, no. 1, pp. 200–204, 2004.
- [107] J.-S. Hsu, S.-Y. Tsai, M.-T. Wu, H.-W. Chung, and Y.-R. Lin, "Fast dynamic contrast-enhanced lung MR imaging using k-t BLAST:

- a spatiotemporal perspective," *Magnetic Resonance in Medicine*, vol. 67, no. 3, pp. 786–792, 2012.
- [108] C. A. Mistretta, O. Wieben, J. Velikina et al., "Highly constrained backprojection for time-resolved MRI," *Magnetic Resonance in Medicine*, vol. 55, no. 1, pp. 30–40, 2006.
- [109] Y. Wu, N. Kim, F. R. Korosec et al., "3D time-resolved contrast-enhanced cerebrovascular MR angiography with subsecond frame update times using radial k-space trajectories and highly constrained projection reconstruction," *American Journal of Neuroradiology*, vol. 28, no. 10, pp. 2001–2004, 2007.
- [110] K. K. Vigen, D. C. Peters, T. M. Grist, W. F. Block, and C. A. Mistretta, "Undersampled projection-reconstruction imaging for time-resolved contrast-enhanced imaging," *Magnetic Resonance in Medicine*, vol. 43, no. 2, pp. 170–176, 2000.
- [111] F. R. Korosec, R. Frayne, T. M. Grist, and C. A. Mistretta, "Time-resolved contrast-enhanced 3D MR angiography," *Magnetic Resonance in Medicine*, vol. 36, no. 3, pp. 345–351, 1996.
- [112] J. F. Utting, S. Kozerke, R. Schnitker, and T. Niendorf, "Comparison of k-t SENSE/k-t BLAST with conventional SENSE applied to BOLD fMRI," *Journal of Magnetic Resonance Imaging*, vol. 32, no. 1, pp. 235–241, 2010.
- [113] B. Madore, G. H. Glover, and N. J. Pelc, "Unaliasing by fourier-encoding the overlaps using the temporal dimension (UNFOLD), applied to cardiac imaging and fMRI," *Magnetic Resonance in Medicine*, vol. 42, no. 5, pp. 813–828, 1999.
- [114] D. C. Peters, D. B. Ennis, and E. R. McVeigh, "High-resolution MRI of cardiac function with projection reconstruction and steady-state free precession," *Magnetic Resonance in Medicine*, vol. 48, no. 1, pp. 82–88, 2002.
- [115] B. Jung, P. Ullmann, M. Honal, S. Bauer, J. Hennig, and M. Markl, "Parallel MRI with extended and averaged GRAPPA kernels (PEAK-GRAPPA): optimized spatiotemporal dynamic imaging," *Journal of Magnetic Resonance Imaging*, vol. 28, no. 5, pp. 1226–1232, 2008.
- [116] P. Kellman, F. H. Epstein, and E. R. McVeigh, "Adaptive sensitivity encoding incorporating temporal filtering (TSENSE)," *Magnetic Resonance in Medicine*, vol. 45, no. 5, pp. 846–852, 2001.
- [117] J. Tsao, S. Kozerke, P. Boesiger, and K. P. Pruessmann, "Optimizing spatiotemporal sampling for k-t BLAST and k-t SENSE: application to high-resolution real-time cardiac steady-state free precession," *Magnetic Resonance in Medicine*, vol. 53, no. 6, pp. 1372–1382, 2005.
- [118] M. A. Griswold, P. M. Jakob, R. M. Heidemann et al., "Generalized Autocalibrating Partially Parallel Acquisitions (GRAPPA)," *Magnetic Resonance in Medicine*, vol. 47, no. 6, pp. 1202–1210, 2002.
- [119] D. K. Sodickson and W. J. Manning, "Simultaneous Acquisition of Spatial Harmonics (SMASH): fast imaging with radiofrequency coil arrays," *Magnetic Resonance in Medicine*, vol. 38, no. 4, pp. 591–603, 1997.
- [120] P. M. Jakob, M. A. Griswold, R. R. Edelman, and D. K. Sodickson, "AUTO-SMASH: a self-calibrating technique for SMASH imaging," *Magnetic Resonance Materials in Physics, Biology and Medicine*, vol. 7, no. 1, pp. 42–54, 1998.
- [121] R. Heidemann and M. Griswold, "VD-AUTO-SMASH imaging," *Magnetic Resonance in Medicine*, vol. 45, no. 6, pp. 1066–1074, 2000.
- [122] P. J. Beatty, A. C. Brau, and S. Chang, "A method for auto-calibrating 2-D accelerated volumetric parallel imaging with clinically practical reconstruction times," in *Proceedings of the International Society for Magnetic Resonance (ISMRM '07)*, vol. 15, p. 1749, Berlin, Germany, 2007.
- [123] M. Blaimer, F. A. Breuer, M. Mueller et al., "2D-GRAPPA-operator for faster 3D parallel MRI," *Magnetic Resonance in Medicine*, vol. 56, no. 6, pp. 1359–1364, 2006.
- [124] K. Pruessmann, M. Weiger, M. Scheidegger, and P. Boesiger, "SENSE: sensitivity encoding for fast MRI," *Magnetic Resonance in Medicine*, vol. 42, pp. 952–962, 1999.
- [125] K. Ocegueda and A. O. Rodriguez, "Slotted surface coil with reduced g-factor for SENSE imaging," in *Proceedings of the 28th Annual International Conference of the IEEE Engineering in Medicine and Biology Society (EMBS '06)*, vol. 1, pp. 1904–1906, September 2006.
- [126] L. T. Muftuler, G. Chen, and O. Nalcioglu, "An inverse method to design RF coil arrays optimized for SENSE imaging," *Physics in Medicine and Biology*, vol. 51, no. 24, article 012, pp. 6457–6469, 2006.
- [127] B. Liu, K. King, M. Steckner, J. Xie, J. Sheng, and L. Ying, "Regularized sensitivity encoding (SENSE) reconstruction using bregman iterations," *Magnetic Resonance in Medicine*, vol. 61, no. 1, pp. 145–152, 2009.
- [128] D. Liang, H. Wang, and L. Ying, "SENSE reconstruction with nonlocal TV regularization," in *Proceedings of the Annual International Conference of the IEEE Engineering in Medicine and Biology Society (EMBC '09)*, pp. 1032–1035, 2009.
- [129] F.-H. Lin, K. K. Kwong, J. W. Belliveau, and L. L. Wald, "Parallel imaging reconstruction using automatic regularization," *Magnetic Resonance in Medicine*, vol. 51, no. 3, pp. 559–567, 2004.
- [130] A. A. Samsonov, "On optimality of parallel MRI reconstruction in k-space," *Magnetic Resonance in Medicine*, vol. 59, no. 1, pp. 156–164, 2008.
- [131] S. O. Schönberg, O. Dietrich, and M. F. Reiser, *Parallel Imaging in Clinical MR Applications*, Springer, 2007.
- [132] M. N. J. Paley, K. J. Lee, J. M. Wild, P. D. Griffiths, and E. H. Whitby, "Simultaneous parallel inclined readout image technique," *Magnetic Resonance Imaging*, vol. 24, no. 5, pp. 557–562, 2006.
- [133] F. A. Breuer, M. Blaimer, R. M. Heidemann, M. F. Mueller, M. A. Griswold, and P. M. Jakob, "Controlled aliasing in parallel imaging results in higher acceleration (CAIPIRINHA) for multi-slice imaging," *Magnetic Resonance in Medicine*, vol. 53, no. 3, pp. 684–691, 2005.
- [134] D. Stäb, C. O. Ritter, F. A. Breuer, A. M. Weng, D. Hahn, and H. Köstler, "CAIPIRINHA accelerated SSFP imaging," *Magnetic Resonance in Medicine*, vol. 65, no. 1, pp. 157–164, 2011.
- [135] S. R. Yutzy, N. Seiberlich, J. L. Duerk, and M. A. Griswold, "Improvements in multislice parallel imaging using radial CAIPIRINHA," *Magnetic Resonance in Medicine*, vol. 65, no. 6, pp. 1630–1637, 2011.
- [136] H. J. Michaely, J. N. Morelli, J. Budjan et al., "CAIPIRINHA-Dixon-TWIST (CDT)-volume-interpolated breath-hold examination (VIBE): a new technique for fast time-resolved dynamic 3-dimensional imaging of the abdomen with high spatial resolution," *Investigative Radiology*, vol. 48, no. 8, pp. 590–597, 2013.
- [137] M. H. Yu, J. M. Lee, J.-H. Yoon, B. Kiefer, J. K. Han, and B.-I. Choi, "Clinical application of controlled aliasing in parallel imaging results in a higher acceleration (CAIPIRINHA)-volumetric interpolated breathhold (VIBE) sequence for gadoteric acid-enhanced liver MR imaging," *Journal of Magnetic Resonance Imaging*, vol. 38, no. 5, pp. 1020–1026, 2013.

- [138] R. Nunes, J. Hajnal, X. Golay, and D. Larkman, "Simultaneous slice excitation and reconstruction for single shot EPI," in *Proceedings of the International Society for Magnetic Resonance in Medicine (ISMRM '06)*, vol. 14, p. 293, 2006.
- [139] K. Setsompop, B. A. Gagoski, J. R. Polimeni, T. Witzel, V. J. Wedeen, and L. L. Wald, "Blipped-controlled aliasing in parallel imaging for simultaneous multislice echo planar imaging with reduced g-factor penalty," *Magnetic Resonance in Medicine*, vol. 67, no. 5, pp. 1210–1224, 2012.
- [140] S. J. Riederer, T. Tasciyan, F. Farzaneh, J. N. Lee, R. C. Wright, and R. J. Herfkens, "MR fluoroscopy: technical feasibility," *Magnetic Resonance in Medicine*, vol. 8, no. 1, pp. 1–15, 1988.
- [141] J. J. van Vaals, M. E. Brummer, W. T. Dixon et al., "Keyhole" method for accelerating imaging of contrast agent uptake," *Journal of Magnetic Resonance Imaging*, vol. 3, no. 4, pp. 671–675, 1993.
- [142] M. Doyle, E. G. Walsh, G. G. Blackwell, and G. M. Pohost, "Block regional interpolation scheme for k-space (BRISK): a rapid cardiac imaging technique," *Magnetic Resonance in Medicine*, vol. 33, no. 2, pp. 163–170, 1995.
- [143] T. Song, A. F. Laine, Q. Chen et al., "Optimal k-space sampling for dynamic contrast-enhanced MRI with an application to MR renography," *Magnetic Resonance in Medicine*, vol. 61, no. 5, pp. 1242–1248, 2009.
- [144] R. P. Lim, M. Shapiro, E. Y. Wang et al., "3D time-resolved MR angiography (MRA) of the carotid arteries with time-resolved imaging with stochastic trajectories: comparison with 3D contrast-enhanced bolus-chase MRA and 3D time-of-flight MRA," *American Journal of Neuroradiology*, vol. 29, no. 10, pp. 1847–1854, 2008.
- [145] J. Tsao, P. Boesiger, and K. P. Pruessmann, "k-t BLAST and k-t SENSE: dynamic MRI with high frame rate exploiting spatiotemporal correlations," *Magnetic Resonance in Medicine*, vol. 50, no. 5, pp. 1031–1042, 2003.
- [146] F. Huang, J. Akao, S. Vijayakumar, G. R. Duensing, and M. Limkeman, "K-t GRAPPA: a k-space implementation for dynamic MRI with high reduction factor," *Magnetic Resonance in Medicine*, vol. 54, no. 5, pp. 1172–1184, 2005.
- [147] S. Schnell, M. Markl, P. Entezari et al., "k-t GRAPPA accelerated four-dimensional flow MRI in the aorta: effect on scan time, image quality, and quantification of flow and wall shear stress," *Magnetic Resonance in Medicine*, 2013.
- [148] P. Lai, F. Huang, A. C. Larson, and D. Li, "Fast four-dimensional coronary MR angiography with k-t GRAPPA," *Journal of Magnetic Resonance Imaging*, vol. 27, no. 3, pp. 659–665, 2008.
- [149] M. Lustig, D. Donoho, and J. M. Pauly, "Sparse MRI: the application of compressed sensing for rapid MR imaging," *Magnetic Resonance in Medicine*, vol. 58, no. 6, pp. 1182–1195, 2007.
- [150] U. Gamper, P. Boesiger, and S. Kozerke, "Compressed sensing in dynamic MRI," *Magnetic Resonance in Medicine*, vol. 59, no. 2, pp. 365–373, 2008.
- [151] M. S. Hansen, C. Baltes, J. Tsao, S. Kozerke, K. P. Pruessmann, and H. Eggers, "k-t BLAST reconstruction from non-Cartesian k-t space sampling," *Magnetic Resonance in Medicine*, vol. 55, no. 1, pp. 85–91, 2006.
- [152] C. M. Tsai and D. G. Nishimura, "Reduced aliasing artifacts using variable-density k-space sampling trajectories," *Magnetic Resonance in Medicine*, vol. 43, no. 3, pp. 452–458, 2000.
- [153] K. Scheffler and J. Hennig, "Reduced circular field-of-view imaging," *Magnetic Resonance in Medicine*, vol. 40, no. 3, pp. 474–480, 1998.
- [154] M. Doneva, P. Börnert, H. Eggers, A. Mertins, J. Pauly, and M. Lustig, "Compressed sensing for chemical shift-based water-fat separation," *Magnetic Resonance in Medicine*, vol. 64, no. 6, pp. 1749–1759, 2010.
- [155] C. N. Wiens, C. M. McCurdy, J. D. Willig-Onwuachi, and C. A. McKenzie, "R<sub>2</sub><sup>\*</sup>-corrected water-fat imaging using compressed sensing and parallel imaging," *Magnetic Resonance in Medicine*, 2013.
- [156] R. Otazo, D. Kim, L. Axel, and D. K. Sodickson, "Combination of compressed sensing and parallel imaging for highly accelerated first-pass cardiac perfusion MRI," *Magnetic Resonance in Medicine*, vol. 64, no. 3, pp. 767–776, 2010.
- [157] D. Kim, H. A. Dyvorne, R. Otazo, L. Feng, D. K. Sodickson, and V. S. Lee, "Accelerated phase-contrast cine MRI using k-t SPARSE-SENSE," *Magnetic Resonance in Medicine*, vol. 67, no. 4, pp. 1054–1064, 2012.
- [158] H. Jung, K. Sung, K. S. Nayak, E. Y. Kim, and J. C. Ye, "K-t FOCUSS: a general compressed sensing framework for high resolution dynamic MRI," *Magnetic Resonance in Medicine*, vol. 61, no. 1, pp. 103–116, 2009.
- [159] M. Akçakaya, T. A. Basha, R. H. Chan, W. J. Manning, and R. Nezafat, "Accelerated isotropic sub-millimeter whole-heart coronary MRI: compressed sensing versus parallel imaging," *Magnetic Resonance in Medicine*, 2013.
- [160] A. Hsiao, M. Lustig, M. T. Alley, M. J. Murphy, and S. S. Vasanawala, "Evaluation of valvular insufficiency and shunts with parallel-imaging compressed-sensing 4D phase-contrast MR imaging with stereoscopic 3D velocity-fusion volume-rendered visualization," *Radiology*, vol. 265, no. 1, pp. 87–95, 2012.
- [161] H. Nguyen and G. Glover, "A modified generalized series approach: application to sparsely sampled fMRI," *IEEE Transactions on Biomedical Engineering*, vol. 60, no. 10, pp. 2867–2877, 2013.
- [162] D. J. Holland, C. Liu, X. Song et al., "Compressed sensing reconstruction improves sensitivity of variable density spiral fMRI," *Magnetic Resonance in Medicine*, vol. 70, no. 6, pp. 1634–1643, 2013.

## Review Article

# Current Opportunities and Challenges of Magnetic Resonance Spectroscopy, Positron Emission Tomography, and Mass Spectrometry Imaging for Mapping Cancer Metabolism *In Vivo*

Gigin Lin<sup>1,2,3</sup> and Yuen-Li Chung<sup>4</sup>

<sup>1</sup> Department of Radiology, Chang Gung Memorial Hospital at Linkou, Chang Gung University, 5 Fuhsing Street, Guishan, Taoyuan 333, Taiwan

<sup>2</sup> Molecular Imaging Center, Chang Gung Memorial Hospital at Linkou, Chang Gung University, 5 Fuhsing Street, Guishan, Taoyuan 333, Taiwan

<sup>3</sup> Metabolomics Core Laboratory, Chang Gung Memorial Hospital at Linkou, Chang Gung University, 5 Fuhsing Street, Guishan, Taoyuan 333, Taiwan

<sup>4</sup> The Institute of Cancer Research and Royal Marsden Hospital, CRUK Cancer Imaging Centre, Downs Road, Sutton, Surrey SM2 5PT, UK

Correspondence should be addressed to Yuen-Li Chung; [yuen-li.chung@icr.ac.uk](mailto:yuen-li.chung@icr.ac.uk)

Received 19 October 2013; Revised 6 January 2014; Accepted 19 January 2014; Published 3 March 2014

Academic Editor: Tzu-Chen Yen

Copyright © 2014 G. Lin and Y.-L. Chung. This is an open access article distributed under the Creative Commons Attribution License, which permits unrestricted use, distribution, and reproduction in any medium, provided the original work is properly cited.

Cancer is known to have unique metabolic features such as Warburg effect. Current cancer therapy has moved forward from cytotoxic treatment to personalized, targeted therapies, with some that could lead to specific metabolic changes, potentially monitored by imaging methods. In this paper we addressed the important aspects to study cancer metabolism by using image techniques, focusing on opportunities and challenges of magnetic resonance spectroscopy (MRS), dynamic nuclear polarization (DNP)-MRS, positron emission tomography (PET), and mass spectrometry imaging (MSI) for mapping cancer metabolism. Finally, we highlighted the future possibilities of an integrated *in vivo* PET/MR imaging systems, together with an *in situ* MSI tissue analytical platform, may become the ultimate technologies for unraveling and understanding the molecular complexities in some aspects of cancer metabolism. Such comprehensive imaging investigations might provide information on pharmacometabolomics, biomarker discovery, and disease diagnosis, prognosis, and treatment response monitoring for clinical medicine.

## 1. Introduction

Cancer is known to have unique metabolic features [1]. Knowledge of cancer metabolism can be applied not only for early detection and diagnosis of cancer, but also in the evaluation of tumor response to medical interventions and therapies [2]. The first characterized phenotype observed in cancer cells is the Warburg effect [3], which describes a shift from energy generation through oxidative phosphorylation to energy generation through anaerobic glycolysis, even under normal oxygen concentrations. Anaerobic glycolysis produces only two ATPs per glucose and is less efficient than oxidative phosphorylation [4, 5]. Cancer cells require high-energy

demand to support cell growth and proliferation; therefore cancer cells have increased glucose uptake, glycolytic activity, and lactate production and decreased mitochondrial activity, low bioenergetic status, and aberrant phospholipid metabolism [6, 7]. Several important oncogenes involved in the development and progression of common human cancers have also been found to regulate glycolysis. For example, unregulated activity of the serine/threonine kinase Akt has been shown to increase glucose uptake of tumor cells as well as increase resistance to apoptosis [8–10]. The oncogene *c-myc*, a transcription factor, controls and activates numerous glycolytic genes (e.g., hexokinase 2, enolase, and lactate dehydrogenase A) [11, 12]. Oncogenic *ras* is an important protein

that controls signaling pathways for cell growth, regulation, and malignancy transformation [13] and it has been seen to increase the concentration of fructose-2,6,-bisphosphate (F2, 6BP), which is an allosteric activator of phosphofructokinase, and it catalyzes the phosphorylation of fructose-6-phosphate to fructose-1,6-bisphosphate [14]. Recent advances have established further links between cancer metabolism and genetic alterations in *p53* [15], AMPK [16], PI3K [17, 18] and HIF [19].

There are growing interests in developing therapies that target important signaling pathways (e.g. PI3K [18] and MAPK [20]) and transcription factors (e.g. HIF-1 [21]) and inhibit upregulated enzymes (e.g. pyruvate dehydrogenase kinase (PDK) [22] and choline kinase [23]) and metabolite transporters (e.g. glucose transporter (Glut1) [24] and monocarboxylate transporter-1 (MCT-1) [25]). Those targeted therapies might alter cancer metabolism, and the changes in endogenous metabolites in cancer cells might be detected even before changes in tumor sizes [26–28]. Imaging methods are needed to detect early metabolic changes in cancer following treatment and these imaging readouts could be useful for monitoring the response to therapies [29, 30].

Tumor heterogeneity and its adaptations to microenvironment are important factors that could affect the effectiveness of cancer treatment; hence, the ability to image and spatially map the heterogeneity of metabolism within a tumor will be very useful for planning the treatment regime. Intratumoral heterogeneity and branched evolution are recently revealed in multiple spatially separated samples obtained from primary renal carcinomas and associated metastatic sites by using genome sequencing [31]. In addition, the metabolic heterogeneity is not only attributed to genetic alteration but is also an adaptation to hypoxic tumor microenvironment. Glycolysis confers a significant growth advantage by producing the required metabolites for cancer growth [27, 32–34], as lactate can be used by oxygenated cancer cells as oxidative fuel [35], in order to spare the glucose for the more anoxic cells in the center of the tumor [36]. This cooperation between hypoxic and normoxic tumor cells optimizes energy production and allows cells to adapt efficiently to their environmental oxygen conditions [37, 38].

Conventionally, nuclear magnetic resonance (NMR) spectroscopy [67] and mass spectrometry (MS) [68] can be used separately or in combination to provide overlapping yet complementary data to evaluate cancer [69–72]. MS have high sensitivity but the samples required prior separations using gas- or lipid-chromatography. NMR has a lower sensitivity than MS but it can measure all the detectable molecules in the sample simultaneously without the need to prior separation, cancelling out the quantification errors within the method [69]. Although analyses of biopsies with many metabolites correlated with disease aggressiveness [73], the conventional metabolomic experiments using a single biopsy of small tumor or extracting metabolites from relatively large tissue areas do not provide the spatial information of the metabolites and multiple biopsies or biopsy of normal tissue counterpart; for comparison is not feasible in routine clinical practice. Hence, noninvasive imaging would be a useful solution for spatial mapping of metabolites. The

potential imaging techniques reviewed in this paper include, but are not limited to, magnetic resonance spectroscopy (MRS), dynamic nuclear polarization (DNP) MRS, positron emission tomography (PET), and mass spectrometry imaging (MSI) for tissue characterization. Table 1 summarizes the advantages, disadvantages, and clinical applications of each imaging technique.

## 2. Magnetic Resonance Spectroscopy (MRS)

Magnetic resonance spectroscopy (MRS) is a technique that can be used in preclinical and clinical settings to study cancer metabolism [74]. It is based on nuclei such as <sup>1</sup>H, <sup>31</sup>P and, <sup>13</sup>C that possess the property of magnetic spin. When they are placed in a magnetic field, these nuclei become aligned or opposed to the external magnetic field. Many of the nuclei are flipped into the other magnetic state when a radiofrequency pulse is applied, and the differences in the populations between these two magnetic energy states are detected as a radio wave as the system returns to equilibrium. The strength of this local field depends on the electronic environment around the nucleus. Different chemical structures possess different electronic environments and lead to nuclei resonating at slightly different frequencies. These frequencies are termed as chemical shifts, which are expressed as the dimensionless units, parts per million (ppm), in the spectrum and represent the metabolites of the measured sample [75]. Additional magnetic field gradients cause nuclei at different locations to precess at different speeds, which allows spatial information to be recovered using Fourier analysis of the measured signal [75]. By spatially encoding chemical shift information, one can generate MRS imaging by obtaining signals at different chemical shifts. This can be achieved by frequency selective radiofrequency pulses, as in stimulated echo acquisition mode (STEAM) [76] and point-resolved spectroscopy (PRESS) [77] in proton (<sup>1</sup>H)-MRS, or by excitation and subsequent subtraction of unwanted signals, as in image selective *in vivo* spectroscopy (ISIS) technique [78] in phosphorus (<sup>31</sup>P)-MRS. In addition, multivoxel spectroscopy, such as chemical shift imaging (CSI) [79], can collect spectroscopic data from multiple adjacent voxels in a single measurement.

The clinical use of spectroscopy as an adjunct to MRI has expanded dramatically over the past decades because of technical advances in hardware and pulse sequence design that have improved the spatial and temporal resolution of spectral data. Nowadays most clinical MR scanners have routine sequences for <sup>1</sup>H-MRS measurements, providing a wide range of metabolic and functional information integrated with complementary MRI localization. Metabolites commonly detected in clinical <sup>1</sup>H-MRS include N-acetyl-aspartate (NAA) in the normal brain tissue [39] and citrate in the normal prostate [40], and their levels decrease once being replaced by tumor. MRS detection of total choline signal has been used to diagnose and monitor breast [41], brain [42], and prostate cancers [44] and for monitoring the response to anticancer therapy [23, 72, 80]. In addition,

TABLE 1: Comparison of major imaging techniques for studying cancer metabolism.

Imaging techniques	Advantages	Disadvantages	Clinical applications	References
Magnetic resonance spectroscopy (MRS)	(i) Widely used medical imaging technique (ii) Ability to assess multiple metabolites in one measurement (iii) No radiation concern	(i) It has relatively long acquisition time (ii) Data processing is not routine in the clinic (iii) Lack of familiarity with clinicians	Brain, head and neck, prostate, breast, and cervix	[39–46]
Dynamic nuclear polarization- (DNP-) MRS	(i) Signal enhancements of over 10,000-fold of magnitude for stable isotope carbon-13 ( $^{13}\text{C}$ ) enriched compounds (ii) Simultaneous detection of multiple hyperpolarized molecules allowed several metabolic pathways to be probed at the same time (iii) No radiation concern (iv) Short acquisition time (v) Real-time observation of not only the uptake of the targeted molecule but also its flux to produce downstream metabolic products	Hyperpolarized $^{13}\text{C}$ -labelled substrates have very short half-life (in tens of seconds)	Prostate	[47]
Positron emission tomography (PET)	(i) Widely used in clinical applications (ii) High sensitivity	(i) Not all tumors show a significant increase in metabolic activity on FDG-PET imaging (ii) Difficult to evaluate malignant lesions in tissues that physiologically take up FDG (such as the central nervous system) or excrete FDG (such as the kidneys and bladder) or differentiate between inflammation and cancer (iii) Radiation concern (iv) It measures perfusion and accumulation of a tracer and does not differentiate between metabolites containing the radionuclide or tracer per se	Oral cancer, lymphoma, melanoma, lung cancer, esophageal cancer, and colorectal cancer Cervical Ovarian Pancreas Prostate	[48–57]
Mass spectrometry imaging (MSI)	(i) Highly sensitive (ii) It can be used to investigate both identified and unidentified molecules in spatial localized areas without any need for labeling or contrasting agents	Analytical technique of tissue section, not noninvasive imaging	Brain, oral, lung, breast, gastric, pancreatic, renal, ovarian, and prostate cancer	[58–66]

*in vivo*  $^1\text{H}$ -MRS also detects signals from lipid metabolism-related compounds, such as the methylene ( $-\text{CH}_2-$ ) signal at 1.3 ppm and the methyl ( $\text{CH}_3$ ) signal at 0.9 ppm [81], which originate from the fatty acyl chains of the cytoplasmic mobile lipids and not from the membrane lipids [82]. Significantly higher levels of lipid have been detected in high-grade human gliomas when compared to low-grade gliomas [81], and these changes are associated with apoptosis, necrosis, or lipid droplet formation [83–85].

$^{31}\text{P}$ -MRS could provide information on tumor bioenergetics and metabolites such as nucleoside triphosphates (NTPs), phosphocreatine (PCr), and inorganic phosphate (Pi). The production of high-energy phosphates such as NTP and PCr depends on the availability of glucose and oxygen (which are delivered to the tumors through blood vessels),

and is determined by diffusion distances and local oxygen consumption rates. Therefore, in addition to blood flow parameters measured by DCE-MRI or perfusion CT,  $^{31}\text{P}$ -MRS provides an opportunity to monitor downstream biochemical reactions following reduced blood flow in hypoxic regions [85] and is useful in detecting changes in tumor reoxygenation during radiation therapy [86] as well as altered tissue pH level (measured by the Pi chemical shift changes) [87].  $^{31}\text{P}$ -MRS also measures phospholipid metabolites, such as phosphomonoester and phosphodiester in tumor, which in turn could inform on membrane turnover and tumor response following therapies [23, 72, 81].

MRS can also directly measure the pharmacokinetics of drugs that present at relatively high concentrations in the tumor. Most *in vivo* studies on MR pharmacokinetic

measurements of tumors employ fluorinated drugs, such as [5-<sup>19</sup>F]-fluorouracil (5-FU) and its prodrug, as detected by <sup>19</sup>F MRS [88, 89], because <sup>19</sup>F MRS provides relatively high sensitivity combined with low background signal. Successful image-guided delivery of a prodrug enzyme, bacterial cytosine deaminase (bCD), which converts nontoxic [5-<sup>19</sup>F]-fluorocytosine (5-FC) to 5-FU, was recently reported in preclinical studies [90].

Relative to conventional MRI, MRS has lower sensitivities and requires much longer acquisition times and more complex data processing, and with clinicians unfamiliar with the technique, these factors continue to limit the application of MRS in the clinical setting. Currently, there are methodologies that optimize the combined signals from multielement coil arrays to improve detection of low concentration metabolites in MRS [91], in order to improve its sensitivity and spectral resolution. In addition, the availability of higher field strength MR systems and novel techniques such as dynamic nuclear polarization hyperpolarization (DNP) can reduce some of these limitations.

### 3. DNP-MRS

DNP is a novel imaging technique which uses specialized instrumentation to provide signal enhancements of over 10,000-folds of magnitude for stable isotope carbon-13 (<sup>13</sup>C) enriched compounds [92]. Simultaneous detection of multiple hyperpolarized molecules allow several metabolic pathways to be probed at the same time [93, 94], and this enhanced <sup>13</sup>C signal allows the distribution of hyperpolarized <sup>13</sup>C-labeled molecules within the tumor tissue to be visualized [95]. [1-<sup>13</sup>C]Pyruvate has been the most widely studied substrate to date because of its central role in cellular metabolism. [1-<sup>13</sup>C]Pyruvate also has relatively longer *T*<sub>1</sub> relaxation time and rapid transport into the cells for subsequent metabolism [96]. Hyperpolarized [1-<sup>13</sup>C]pyruvate has been used to study the real-time flux of pyruvate to lactate noninvasively following anticancer therapies in xenograft models [97–101]. The first clinical trial of DNP-MRS has recently demonstrated the use of hyperpolarized [1-<sup>13</sup>C]pyruvate to examine prostate cancer metabolism in human [47] (Figure 1), and it paves the way to rapid translation of this exciting technology to clinical research and perhaps clinical practice [96]. Previously, the data analysis to obtain the apparent rate of pyruvate to lactate exchanges following the [1-<sup>13</sup>C]pyruvate DNP-MRS experiment is quite complex, as it requires the fitting of the data to a mathematical model [102]. A much simpler method to analyze this type of data has been developed recently [103], which will improve the ease of use of this methodology in studying cancer metabolism. In addition to pyruvate, extracellular pH has been measured in lymphoma xenografts by using hyperpolarized H<sup>13</sup>CO<sub>3</sub><sup>-</sup> and pH images were obtained by measuring the H<sup>13</sup>CO<sub>3</sub><sup>-</sup>/<sup>13</sup>CO<sub>2</sub> ratio in each imaging voxel [104]. [1, 4-<sup>13</sup>C<sub>2</sub>]Fumarate is potentially a useful agent for detecting treatment response in tumors because the production of labeled malate was shown to be an indicator of necrotic cell death [105].

### 4. Positron Emission Tomography (PET)

Positron emission tomography (PET) is a nuclear medical imaging technique that produces three-dimensional imaging data of functional processes in the body. The system detects pairs of gamma rays emitted indirectly by positron-emitting radionuclide tracers, to provide functional or metabolic information in PET imaging [107]. When combined with X-ray computed tomography (CT), PET/CT imaging can provide both molecular information and anatomic localization. <sup>18</sup>F-fluorodeoxyglucose (FDG) PET is by far the most successfully used imaging technique to study glucose uptake in tumors *in vivo*. After intravenous injection, <sup>18</sup>F-FDG is transported across the cell membrane by glucose transporters and metabolized to <sup>18</sup>F-FDG-6-phosphate by hexokinase [108]. In contrast to the complex metabolic fate of glucose-6-phosphate from glucose, <sup>18</sup>F-FDG-6-phosphate cannot be further metabolized in the glycolytic pathway because the fluorine atom at the C<sub>2</sub> position prevents <sup>18</sup>F-FDG-6-phosphate from downstream catabolism. This leads to steady accumulation of <sup>18</sup>F-FDG-6-phosphate in metabolically active cells such as cancer [109].

Over the past decade, <sup>18</sup>F-FDG PET/CT has become a routine clinical test for staging and restaging of a variety of malignant tumors, including head and neck cancer, lymphoma, colorectal, cervical cancer (Figure 2, [56]), and many other solid organ cancers [48], with a sensitivity of about or above 90% [110]. There is considerable evidence that the reduction of <sup>18</sup>F-FDG uptake is caused by a loss of viable tumor cells following chemo- and radiotherapy [111]. However, the close relationship between various oncogenic signaling pathways and tumor glucose metabolism suggests that the drugs targeting these signal transduction pathways may have a more direct effect on cellular glucose metabolism. For example, decreased <sup>18</sup>F-FDG uptakes were found in patients with gastrointestinal stromal tumors (GIST) within hours following treatment with the c-Kit inhibitor imatinib [50, 51]. Rapid reduction in <sup>18</sup>F-FDG uptakes was also observed in patients with non-small cell lung cancer treated with EGFR kinase inhibitor gefitinib [52].

Although <sup>18</sup>F-FDG is widely used in clinical applications, not all tumor types show a significant increase in metabolic activity on <sup>18</sup>F-FDG PET imaging, for example, in prostate, neuroendocrine, and hepatic tumors [48]. Furthermore, it is difficult to evaluate malignant lesions in organs that normally take up (such as the central nervous system) or excrete FDG (such as the kidneys, urinary bladder, and prostate) or to differentiate between inflammation and cancer. Therefore, other PET tracers in addition to FDG have been developed for oncological studies [30], either for clinical use or at different stages of clinical evaluation. These compounds include <sup>11</sup>C-acetate (a precursor of membrane fatty acids) in prostate cancer [112], <sup>11</sup>C-methionine (a precursor of S-adenosylmethionine, which is required for polyamine synthesis) in brain tumor [113], <sup>18</sup>F-choline (a substrate of choline kinase in choline metabolism) in prostate cancer [114], and <sup>18</sup>F-3'-fluoro-3'-deoxy-L-thymidine (<sup>18</sup>F-FLT) (a substrate of thymidine kinase [TK-2] in DNA synthesis

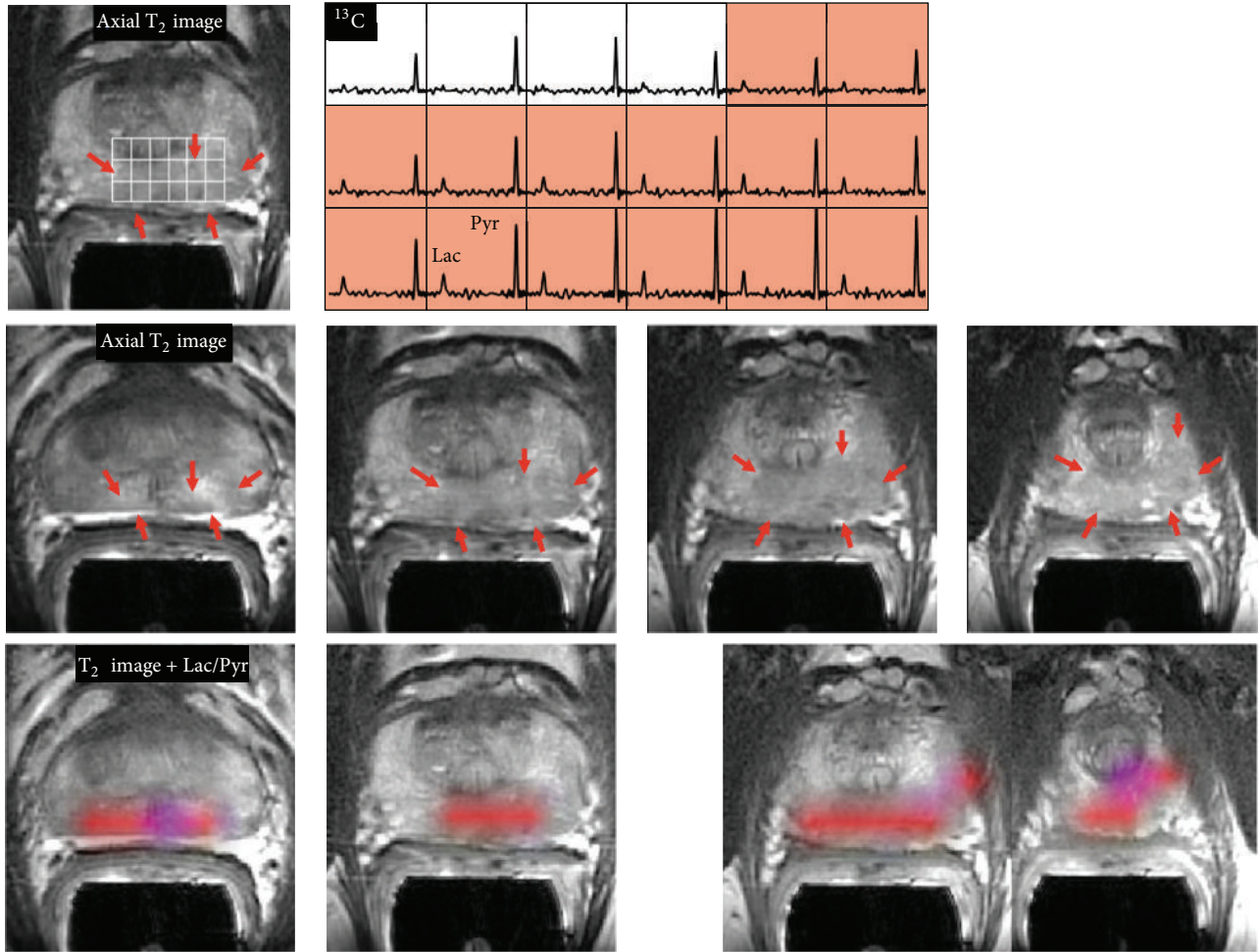


FIGURE 1: 3D  $[1-^{13}\text{C}]$ Pyruvate dynamic nuclear hyperpolarization magnetic resonance spectroscopy (DNP-MRS) imaging in a patient with prostate cancer. The upper panel shows an axial T2-weighted images and corresponding spectral array with the area of putative tumor highlighted by pink shading. A region of tumor was observed on the T2-weighted images (red arrows). A region of relatively high hyperpolarized  $[1-^{13}\text{C}]$ lactate was observed in the same location as the abnormalities that had been observed on the multiparametric 1H staging exam. The lower panels show axial T2 images with and without metabolite overlays for different axial slices from the same patient. The colored regions in these overlays have a ratio of  $[1-^{13}\text{C}]$ lactate/ $[1-^{13}\text{C}]$ pyruvate  $\geq 0.2$ . These demonstrated a large volume of bilateral cancer. Reprinted with permission from [106]. Copyright 2013 American Association for the Advancement of Science.

and a specific marker of cell proliferation) [115]. Efforts are also made to improve detection and measurement of low level metabolized  $^{18}\text{F}$  tracer from the  $^{18}\text{F}$ -labeled pyrimidine nucleoside analogues [116].

**4.1. Comparison of PET and DNP-MRS.** An advantage of DNP-MRS is that it does not have radiation concern that is commonly associated with PET. Although both PET and DNP-MRS can measure the uptake of labeled substrates in real-time, another key advantage of DNP-MRS is that both the injected substrate and its metabolic products can be detected and followed in real-time, allowing the observation of not only the uptake of the targeted molecule but also its downstream metabolic products [96]. In contrast, PET measures perfusion and accumulation of a tracer, but does not

differentiate between metabolites containing the radionuclide or tracer per se.

The most notable limitation of DNP-MRS imaging is the very short half-life (in tens of seconds) of the hyperpolarized  $^{13}\text{C}$ -substrates, which is affected by the substrates'  $T_1$  value and the field strength of the MR scanner (lower field strength MR scanner improves the half-life of the hyperpolarized substrates) [96]. The hyperpolarized state decreases to its equilibrium value with a time constant according to the spin lattice relaxation time  $T_1$ .  $T_1$  relaxation times are dependent on the nucleus but are also sensitive to a host of other factors including the applied field, the location in a molecule, molecular structure and motion, and the chemical environment.

In general, PET is much more sensitive than DNP-MRS [117]. PET tracers can be detected in the nano- to picomolar

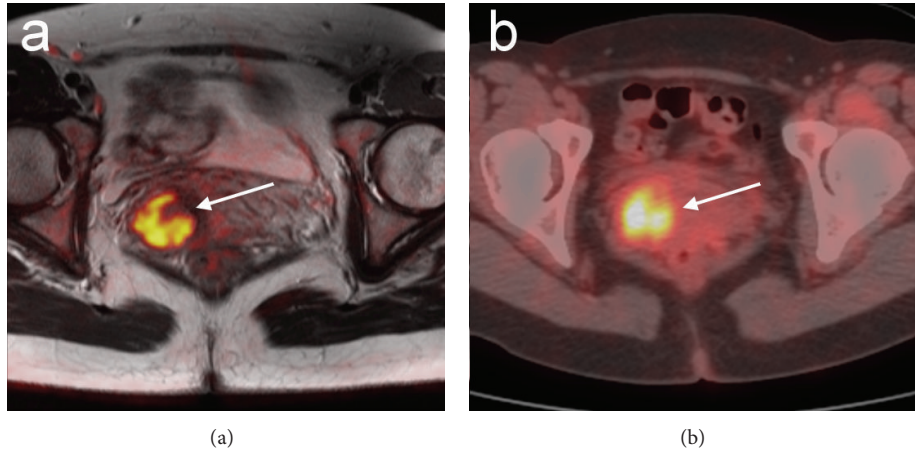


FIGURE 2: An example of PET/CT and MRI in the female pelvis. A 43-year-old female patient with a primary well-differentiated adenocarcinoma of the uterine cervix. Primary cervical tumor is highlighted (arrow) and well correlated in (a) diffusion-weighted MRI and (b) 18F-FDG PET/CT. Reprinted with permission from [56]. Copyright 2008 Springer-Verlag.

range [118]; whereas DNP-MRS sensitivity is still in the millimolar range. Therefore, DNP molecules are injected at concentrations that greatly exceed physiologic levels (e.g., 15–28 mmoles of pyruvate in mouse models [97, 119]), whereas PET-labeled molecules can be administered at concentrations that are unlikely to perturb normal metabolism. Although hyperpolarized [ $1-^{13}\text{C}$ ]pyruvate increases the sensitivity of MR imaging, signal-to-noise ratio constraints still exist for spatial and temporal resolution of  $^{13}\text{C}$  DNP-MRS, especially relative to PET, emphasizing the need for further development of MR methodology [96].

**4.2. Potential of Simultaneous PET/MRS.** The integrated PET/MRI system could offer potential in the management of cancer, with prostate, head/neck, and breast cancers among the primary indications for PET/MRI [120]. The benefit of integrating PET and MRI might not only result in improved sensitivity and spatial resolution, but also allow the specific sets of metabolic events to be examined at the same time [121]. In a preclinical murine glioma model, advancing tumor proliferation caused an increase in  $^{11}\text{C}$ -choline uptake as measured by PET, while gliosis and inflammation accounted for a high peritumoral total choline signal in MRS [122]. A decrease in  $^{18}\text{F}$ -FDG PET and changes in phosphomonoesters by  $^{31}\text{P}$ -MRS were associated with decreases in hexokinase II and Glut1 expression in HER2 expressing breast tumor xenografts and responding to trastuzumab treatment [123]. These studies exemplified that PET/MRS could be used to monitor treatment response and could provide unique information on drug biodistribution, targeting, and metabolism and serve as surrogate pharmacokinetics/pharmacodynamics (PK/PD) markers [124].

Although clinical evidence of simultaneous PET and MRS measurement is not available at present, previous reports based on the correlation of PET and MRS have demonstrated the potential usefulness of integrated PET/MRS. A significant positive correlation was found

between tumor total choline concentration by  $^1\text{H}$ -MRS and total lesion glycolysis measured by  $^{18}\text{F}$ -FDG PET before treatment in head and neck cancer patients [125]. For primary staging in prostate cancer patients,  $^1\text{H}$ -MRS was reported to improve the sensitivity of  $^{11}\text{C}$ -choline PET/CT in localizing tumor in the prostate gland and achieved up to 97% of overall accuracy [126]. Combined  $^1\text{H}$ -MRS and DCE-MRI have improved the sensitivity of  $^{18}\text{F}$ -choline PET/CT from 62% to 92% in identifying local prostate cancer recurrence, particularly in patients with low biochemical progression after surgical treatment [127]. For breast cancer patients with an invasive ductal carcinoma of 1.5–3 cm in size, the total choline level in tumors measured by  $^1\text{H}$ -MRS was highly correlated with the standardized  $^{18}\text{F}$ -FDG uptake value obtained by PET/CT, and these measurements were also supported by the histologic prognostic parameters (nuclear grade, estrogen receptor status, and triple-negative lesion status) [128]. The sensitivity and specificity of total choline level by  $^1\text{H}$ -MRS for detecting breast cancer were 83% and 85%, respectively, and both values could be as high as 92% after technical exclusions [129].

Whether the simultaneous collection of MRS data together with PET/MRI will improve diagnosis of brain tumor remained unclear. However, evidence shows that by using choline/creatinine ratio  $> 1.5$  as a threshold, the addition of  $^1\text{H}$ -MRS could marginally increase the sensitivity of contrast-enhanced MRI, from 86% to 100% ( $P = .79$ ), without altering the specificity (67%) [130]. In addition, by using cutoff points of NAA/Cho  $\leq 0.61$  on  $^1\text{H}$ -MRS and relative cerebral blood volume (rCBV)  $\geq 1.50$  (corresponding to diagnosis of the tumors), a sensitivity of 72% and specificity of 91% in differentiating tumors from nonneoplastic lesions have been achieved [131]. The distinction of MRS between recurrent tumor and radiation necrosis in brain tumor using the Cho/NAA ratio could be made with 85% sensitivity and 69% specificity [132].

Hepatocyte-specific (gadoxetic acid) enhanced MRI is a powerful diagnostic tool for hepatocellular carcinoma (HCC) [133], with sensitivity of about 81–90% for lesion size < 2 cm [134, 135]. For the detection of HCC, <sup>18</sup>F-FDG PET/CT has a sensitivity of only around 64%–68%, which can be improved by using <sup>11</sup>C-acetate [136] and <sup>18</sup>F-fluorocholine [137] tracers, with reported sensitivity rising to 84% and 88%, respectively. Direct comparison of diagnostic accuracy of <sup>11</sup>C-acetate or <sup>18</sup>F-fluorocholine PET/CT versus hepatocyte-specific MRI on liver tumors would be of great interest; this area of research is still under investigation. Menzel et al. recently reported a multimodal *in vivo* assessment of glucose metabolism in HCC tumors using hyperpolarized [ $1-^{13}\text{C}$ ]pyruvate DNP-MRS and <sup>18</sup>F-FDG PET [138]. The increased [ $1-^{13}\text{C}$ ]lactate signals in the tumor is correlated with corresponding enhanced 18F-FDG uptake. This study revealed that PET and <sup>13</sup>C DNP-MRS can be used to visualize increased glycolytic flux in malignant tissue. The combined <sup>13</sup>C DNP-MRS and PET readouts will allow the quantitative dissection of substrate metabolism, with respect to uptake and downstream metabolic pathways. Nonetheless, these first imaging data suggest the feasibility of <sup>13</sup>C MRSI for future clinical use [138].

Integrated PET/MRI measurements for neuroendocrine tumors are not yet available; but efforts have been made by using somatostatin receptor-specific tracer (<sup>68</sup>Ga-DOTATATE) to improve lesion detection by PET [139]. <sup>31</sup>P-MRS has been used to differentiate between responders and nonresponders to arterial embolization in neuroendocrine tumors, with responders that exhibit increased cell membrane renewal (higher phosphomonoester level) and energy consumption (lower NTP and higher Pi levels) [140]. For renal cell carcinoma, <sup>1</sup>H-MRS can significantly differentiate tumor from healthy renal parenchyma by comparing their lipid composition [141]. An *in vitro* [ $1-^{13}\text{C}$ ]pyruvate DNP-MRS study of RCC cells showed a significantly higher pyruvate-to-lactate flux than the normal renal tubule cells. These metastatic RCC cells were also found to have significantly higher monocarboxylate transporter 4 (MCT4) expression and corresponding higher lactate efflux than the nonmetastatic cells, which is essential for maintaining a high rate of glycolysis [142].

## 5. Mass Spectrometry Imaging (MSI)

Mass spectrometry imaging (MSI) is an analytical imaging technique for tissue section. It can provide a very high spatial resolution (typically 10 m) [143], but cannot provide the temporal information as the other noninvasive imaging techniques such as MRS (seconds) and PET (10 seconds to minutes). For spatial mapping, matrix-assisted laser desorption ionization-time of flight (MALDI-TOF) is the most widely used technique to analyze intact biological tissue sections in a two-dimensional fashion [143]. The matrix used in these studies is a small organic molecule with strong absorbance at the laser wavelength. They are applied

on the surface of the histological section and cocrystallized with the sample. A laser pulse is used to ionize the chemical compounds on the sample and charged molecules or molecule fragments are then generated. MSI is based on the measurements of the mass-to-charge ratios, which produces spectra to determine the metabolome of the sample. This technique enables the investigation and spatial localization of both identified and unidentified molecules without any need for labeling or contrasting agents, which further facilitates the discovery of new biomarkers and their validation [144]. The damage on the biomedical tissue sections induced by laser irradiation during MALDI-MSI is relatively modest and the histological and biochemical evaluations can be performed on the same tissue slice after the MSI measurements [145] (Figure 3). The combined use of imaging modalities, such as MSI and fluorescent microscopy and histology/immunohistochemistry (IHC) [146] allows metabolic and pathological evaluations of the tissue sections in a highly precise and reliable way. MALDI MSI-based studies have been used to elucidate molecular signatures from samples with different tumor types and grades, including brain [58], oral [59], lung [60], breast [61], gastric [62], pancreatic [63], renal [64], ovarian [65], and prostate cancers [66].

MALDI-MSI is useful for metabolic imaging, albeit the average scanning time might take hours for a single mass image, depending on sample size and resolution. The target for MSI studies limits to lipid molecules of endogenous metabolites because many kinds of matrix ion peaks are observed in the low-mass range ( $m/z < 700$ ), and the strong peaks that they generate interfere with the detection of the target low-molecular-weight compounds. This is because the  $m/z$  range of most lipid molecules was more than 700 and also lipids are abundant in tissues (e.g., more than 60% of the dry weight of brain tissue) and are easily ionized because of the presence of a polar head [147, 148]. MALDI-MSI was employed for imaging acylcarnitines, PC, lysophosphatidyl-choline (LPC), and sphingomyelin to differentiate viable and necrotic microenvironments of breast tumor xenografts [149]. Recent breakthrough on the use of 9-aminoacridine (9-AA) as a matrix for low-molecular-weight metabolite analysis and negative mode MALDI-MS has been used to detect more than 30 metabolites (which included nucleotides, cofactors, phosphorylated sugars, amino acids, lipids, and carboxylic acids) in ischemia-reperfused rat brain tissue [150]. Hattori et al. have also reported spatiotemporal changes in energy charge, adenylates, and NADH during focal ischemia in a mouse MCAO model [151]. These findings highlight the potential applications of MSI metabolomic imaging technique to visualize spatiodynamics of some aspects of the tissue metabolome.

Although the present MALDI method is highly sensitive and well established on the MSI platform, some limitations need to be overcome before the broad range of endogenous metabolite imaging can be achieved. To date, this method can only apply to *ex vivo* tissue sections. It is generally known that, in MALDI, the detection of molecules is completely dependent on the matrix. In addition, the crystal size of the deposited matrix strongly affects both experimental

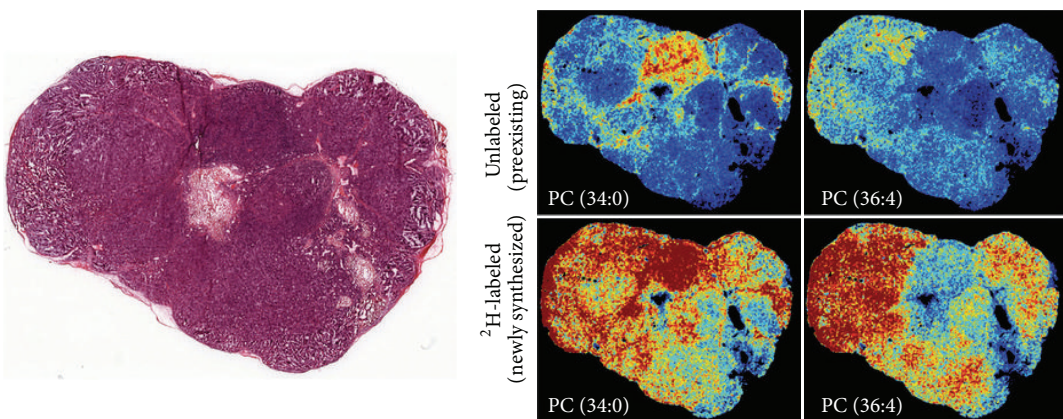


FIGURE 3: Correlation of histopathology and mass spectrometry imaging. Serial sections of the tumor are used for histopathology (left) correlation with MSI results (right). Deconvolution of spectra is performed to separate  ${}^2\text{H}$ -labeled and unlabeled lipids. Intensity images are generated to show the spatial distribution for both newly synthesized and preexisting lipids. Reprinted with permission from [106]. Copyright 2013 Nature Publishing Group, a division of Macmillan Publishers Limited.

reproducibility and spatial resolution in MALDI-MSI. To accelerate the use of MALDI-based metabolic imaging platform, substantial progress in matrix development and its application is required. For tissue imaging in metabolomics, nanostructure-initiator mass spectrometry (NIMS) has been investigated for spatial profiling of metabolites without the need for matrix and with reduced fragmentation [152, 153].

## 6. Concluding Remarks

The cancer metabolomics information provided by multimodality imaging techniques has revolutionized our ways of cancer treatment. Current oncologic therapy has moved forward from cytotoxic treatment to personalized therapy, such as targeting specific signal pathways or oncogene or metabolic enzymes. This would lead to altering metabolic signatures in tumor tissue, which could be monitored by using MRS or PET imaging. The nonradiation nature of MRS renders its ease of transitioning from bench to bedside. Metabolic information provided by multivoxel MRS measurements combined with the anatomical information provided by MRI can significantly improve the assessment of cancer location and extent and cancer aggressiveness. Biomarkers discovered by MRS can lead to development of new PET tracers. With the development of highly specific molecular probes, DNP-MRS and/or PET will play a major and integral role in the diagnosis, prognosis, and monitoring of treatment response in cancer and other diseases. In combination with classical histological/immunohistochemical methods, MSI analysis can provide new insights into the simultaneously occurring metabolic processes in tissue section that could not be obtained otherwise.

In the future, a combination of *in vivo* noninvasive imaging techniques (MRI anatomic imaging and functional imaging including MRS and PET) in integrated MR/PET scanners and *ex vivo* MSI validation with other tissue analytical platforms, may become the ultimate technology for unraveling and understanding some of the molecular complexities

of cancer metabolism. The potential of a comprehensive study on tumor metabolism has recently been demonstrated in a glioma model, by using  ${}^{11}\text{C}$ -choline PET and choline on  ${}^1\text{H}$ -MRS for *in vivo* imaging tumors, and tissue MSI for *ex vivo* validation [122]. Such combination might fulfill the function for pharmacometabolomics, biomarker discovery, disease diagnosis and prognosis, and monitoring treatment response. The development of integrated bioinformatics tools would help to handle the spatial, temporal, and multiparametric data from cancer metabolic imaging.

## Conflict of Interests

The authors declare that there is no conflict of interests regarding the publication of this paper.

## Acknowledgments

We acknowledge the support received from Chang Gung Medical Foundation (Taiwan) Grants CMRPG370444 and CMRPG3B1921, also the Cancer Research UK and EPSRC Cancer Imaging Centre in association with the MRC and Department of Health (England) Grant C1060/A10334.

## References

- [1] D. Hanahan and R. A. Weinberg, "Hallmarks of cancer: the next generation," *Cell*, vol. 144, no. 5, pp. 646–674, 2011.
- [2] R. Kaddurah-Daouk, B. S. Kristal, and R. M. Weinshilboum, "Metabolomics: a global biochemical approach to drug response and disease," *Annual Review of Pharmacology and Toxicology*, vol. 48, pp. 653–683, 2008.
- [3] O. Warburg, "On the origin of cancer cells," *Science*, vol. 123, no. 3191, pp. 309–314, 1956.
- [4] R. A. Gatenby and R. J. Gillies, "A microenvironmental model of carcinogenesis," *Nature Reviews Cancer*, vol. 8, no. 1, pp. 56–61, 2008.

- [5] P. R. Rich, "The molecular machinery of Keilin's respiratory chain," *Biochemical Society Transactions*, vol. 31, no. 6, pp. 1095–1105, 2003.
- [6] J. L. Griffin and R. A. Kauppinen, "Tumour metabolomics in animal models of human cancer," *Journal of Proteome Research*, vol. 6, no. 2, pp. 498–505, 2007.
- [7] L. C. Costello and R. B. Franklin, "Why do tumour cells glycolyse?: from glycolysis through citrate to lipogenesis," *Molecular and Cellular Biochemistry*, vol. 280, no. 1-2, pp. 1–8, 2005.
- [8] R. L. Elstrom, D. E. Bauer, M. Buzzai et al., "Akt stimulates aerobic glycolysis in cancer cells," *Cancer Research*, vol. 64, no. 11, pp. 3892–3899, 2004.
- [9] D. R. Plas and C. B. Thompson, "Akt-dependent transformation: there is more to growth than just surviving," *Oncogene*, vol. 24, no. 50, pp. 7435–7442, 2005.
- [10] T. Porstmann, C. R. Santos, B. Griffiths et al., "SREBP activity is regulated by mTORC1 and contributes to Akt-dependent cell growth," *Cell Metabolism*, vol. 8, no. 3, pp. 224–236, 2008.
- [11] J.-W. Kim and C. V. Dang, "Cancer's molecular sweet tooth and the warburg effect," *Cancer Research*, vol. 66, no. 18, pp. 8927–8930, 2006.
- [12] H. Shim, C. Dolde, B. C. Lewis et al., "c-Myc transactivation of LDH-A: implications for tumor metabolism and growth," *Proceedings of the National Academy of Sciences of the United States of America*, vol. 94, no. 13, pp. 6658–6663, 1997.
- [13] J. Downward, "Targeting RAS signalling pathways in cancer therapy," *Nature Reviews Cancer*, vol. 3, no. 1, pp. 11–22, 2003.
- [14] S. Telang, A. Yalcin, A. L. Clem et al., "Ras transformation requires metabolic control by 6-phosphofructo-2-kinase," *Oncogene*, vol. 25, no. 55, pp. 7225–7234, 2006.
- [15] K. H. Vousden and K. M. Ryan, "P53 and metabolism," *Nature Reviews Cancer*, vol. 9, no. 10, pp. 691–700, 2009.
- [16] D. B. Shackelford and R. J. Shaw, "The LKB1-AMPK pathway: metabolism and growth control in tumour suppression," *Nature Reviews Cancer*, vol. 9, no. 8, pp. 563–575, 2009.
- [17] K.-K. Wong, J. A. Engelman, and L. C. Cantley, "Targeting the PI3K signaling pathway in cancer," *Current Opinion in Genetics and Development*, vol. 20, no. 1, pp. 87–90, 2010.
- [18] N. M. S. Al-Saffar, L. E. Jackson, F. I. Raynaud et al., "The phosphoinositide 3-kinase inhibitor PI-103 downregulates choline kinase  $\alpha$  leading to phosphocholine and total choline decrease detected by magnetic resonance spectroscopy," *Cancer Research*, vol. 70, no. 13, pp. 5507–5517, 2010.
- [19] N. C. Denko, "Hypoxia, HIF1 and glucose metabolism in the solid tumour," *Nature Reviews Cancer*, vol. 8, no. 9, pp. 705–713, 2008.
- [20] M. Beloueche-Babari, L. E. Jackson, N. M. S. Al-Saffar, P. Workman, M. O. Leach, and S. M. Ronen, "Magnetic resonance spectroscopy monitoring of mitogen-activated protein kinase signaling inhibition," *Cancer Research*, vol. 65, no. 8, pp. 3356–3363, 2005.
- [21] B. F. Jordan, K. Black, I. F. Robey, M. Runquist, G. Powis, and R. J. Gillies, "Metabolite changes in HT-29 xenograft tumors following HIF-1 $\alpha$  inhibition with PX-478 as studied by MR spectroscopy in vivo and ex vivo," *NMR in Biomedicine*, vol. 18, no. 7, pp. 430–439, 2005.
- [22] J.-W. Kim, I. Tchernyshyov, G. L. Semenza, and C. V. Dang, "HIF-1-mediated expression of pyruvate dehydrogenase kinase: a metabolic switch required for cellular adaptation to hypoxia," *Cell Metabolism*, vol. 3, no. 3, pp. 177–185, 2006.
- [23] N. M. S. Al-Saffar, H. Troy, A. R. de Molina et al., "Noninvasive magnetic resonance spectroscopic pharmacodynamic markers of the choline kinase inhibitor MN58b in human carcinoma models," *Cancer Research*, vol. 66, no. 1, pp. 427–434, 2006.
- [24] A. Evans, V. Bates, H. Troy et al., "Glut-1 as a therapeutic target: increased chemoresistance and HIF-1-independent link with cell turnover is revealed through COMPARE analysis and metabolomic studies," *Cancer Chemotherapy and Pharmacology*, vol. 61, no. 3, pp. 377–393, 2008.
- [25] P. Sonveaux, T. Copetti, C. J. de Saedeleer et al., "Targeting the lactate transporter MCT1 in endothelial cells inhibits lactate-induced HIF-1 activation and tumor angiogenesis," *PLoS ONE*, vol. 7, no. 3, Article ID e33418, 2012.
- [26] R. L. Yauch and J. Settleman, "Recent advances in pathway-targeted cancer drug therapies emerging from cancer genome analysis," *Current Opinion in Genetics and Development*, vol. 22, no. 1, pp. 45–49, 2012.
- [27] M. G. Vander Heiden, "Targeting cancer metabolism: a therapeutic window opens," *Nature Reviews Drug Discovery*, vol. 10, no. 9, pp. 671–684, 2011.
- [28] D. A. Tennant, R. V. Durán, and E. Gottlieb, "Targeting metabolic transformation for cancer therapy," *Nature Reviews Cancer*, vol. 10, no. 4, pp. 267–277, 2010.
- [29] J. Evelhoch, M. Garwood, D. Vigneron et al., "Expanding the use of magnetic resonance in the assessment of tumor response to therapy: workshop report," *Cancer Research*, vol. 65, no. 16, pp. 7041–7044, 2005.
- [30] P. Workman, E. O. Aboagye, Y.-L. Chung et al., "Minimally invasive Pharmacokinetic and Pharmacodynamic Technologies in hypothesis-testing clinical trials of innovative therapies," *Journal of the National Cancer Institute*, vol. 98, no. 9, pp. 580–598, 2006.
- [31] M. Gerlinger, A. J. Rowan, S. Horswell et al., "Intratumor heterogeneity and branched evolution revealed by multiregion sequencing," *The New England Journal of Medicine*, vol. 366, no. 10, pp. 883–892, 2012.
- [32] T. N. Seyfried and L. M. Shelton, "Cancer as a metabolic disease," *Nutrition and Metabolism*, vol. 7, article 7, 2010.
- [33] R. A. Gatenby and R. J. Gillies, "Why do cancers have high aerobic glycolysis?" *Nature Reviews Cancer*, vol. 4, no. 11, pp. 891–899, 2004.
- [34] M. Israël and L. Schwartz, "The metabolic advantage of tumor cells," *Molecular Cancer*, vol. 10, article 70, 2011.
- [35] O. Feron, "Pyruvate into lactate and back: from the Warburg effect to symbiotic energy fuel exchange in cancer cells," *Radiotherapy and Oncology*, vol. 92, no. 3, pp. 329–333, 2009.
- [36] P. Icard and H. Lincet, "A global view of the biochemical pathways involved in the regulation of the metabolism of cancer cells," *Biochimica et Biophysica Acta*, vol. 1826, no. 2, pp. 423–433, 2012.
- [37] G. L. Semenza, "Tumor metabolism: cancer cells give and take lactate," *The Journal of Clinical Investigation*, vol. 118, no. 12, pp. 3835–3837, 2008.
- [38] P. Sonveaux, F. Végran, T. Schroeder et al., "Targeting lactate-fueled respiration selectively kills hypoxic tumor cells in mice," *The Journal of Clinical Investigation*, vol. 118, no. 12, pp. 3930–3942, 2008.
- [39] J. L. Griffin and R. A. Kauppinen, "A metabolomics perspective of human brain tumours," *The FEBS Journal*, vol. 274, no. 5, pp. 1132–1139, 2007.

- [40] M. G. Swanson, A. S. Zektzer, Z. L. Tabatabai et al., "Quantitative analysis of prostate metabolites using <sup>1</sup>H HR-MAS spectroscopy," *Magnetic Resonance in Medicine*, vol. 55, no. 6, pp. 1257–1264, 2006.
- [41] L. Bartella and W. Huang, "Proton (<sup>1</sup>H) MR spectroscopy of the breast," *Radiographics*, vol. 27, supplement 1, pp. S241–S252, 2007.
- [42] C. Dowling, A. W. Bollen, S. M. Noworolski et al., "Preoperative proton MR spectroscopic imaging of brain tumors: correlation with histopathologic analysis of resection specimens," *American Journal of Neuroradiology*, vol. 22, no. 4, pp. 604–612, 2001.
- [43] S. K. Mukherji, S. Schiro, M. Castillo, L. Kwock, K. E. Muller, and W. Blackstock, "Proton MR spectroscopy of squamous cell carcinoma of the extracranial head and neck: in vitro and in vivo studies," *American Journal of Neuroradiology*, vol. 18, no. 6, pp. 1057–1072, 1997.
- [44] M. Seitz, A. Shukla-Dave, A. Bjartell et al., "Functional magnetic resonance imaging in prostate cancer," *European Urology*, vol. 55, no. 4, pp. 801–814, 2009.
- [45] P. Alusta, I. Im, B. A. Pearce et al., "Improving proton MR spectroscopy of brain tissue for noninvasive diagnostics," *Journal of Magnetic Resonance Imaging*, vol. 32, no. 4, pp. 818–829, 2010.
- [46] M. M. Mahon, I. J. Cox, R. Dina et al., "<sup>1</sup>H Magnetic resonance spectroscopy of preinvasive and invasive cervical cancer: in vivo-ex vivo profiles and effect of tumor load," *Journal of Magnetic Resonance Imaging*, vol. 19, no. 3, pp. 356–364, 2004.
- [47] S. J. Nelson, J. Kurhanewicz, D. B. Vigneron et al., "Metabolic imaging of patients with prostate cancer using hyperpolarized [<sup>1</sup>–<sup>13</sup>C]pyruvate," *Science Translational Medicine*, vol. 5, no. 198, Article ID 198ra08, 2013.
- [48] A. Zhu, D. Lee, and H. Shim, "Metabolic positron emission tomography imaging in cancer detection and therapy response," *Seminars in Oncology*, vol. 38, no. 1, pp. 55–69, 2011.
- [49] S.-H. Ng, T.-C. Yen, C.-T. Liao et al., "<sup>18</sup>F-FDG PET and CT/MRI in oral cavity squamous cell carcinoma: a prospective study of 124 patients with histologic correlation," *Journal of Nuclear Medicine*, vol. 46, no. 7, pp. 1136–1143, 2005.
- [50] A. D. van den Abbeele and R. D. Badawi, "Use of positron emission tomography in oncology and its potential role to assess response to imatinib mesylate therapy in gastrointestinal stromal tumors (GISTs)," *European Journal of Cancer*, vol. 38, supplement 5, pp. S60–65, 2002.
- [51] S. Stroobants, J. Goeminne, M. Seegers et al., "18FDG-Positron emission tomography for the early prediction of response in advanced soft tissue sarcoma treated with imatinib mesylate (Glivec)," *European Journal of Cancer*, vol. 39, no. 14, pp. 2012–2020, 2003.
- [52] N. Sunaga, N. Oriuchi, K. Kaira et al., "Usefulness of FDG-PET for early prediction of the response to gefitinib in non-small cell lung cancer," *Lung Cancer*, vol. 59, no. 2, pp. 203–210, 2008.
- [53] B. Simcock, D. Neesham, M. Quinn, E. Drummond, A. Milner, and R. J. Hicks, "The impact of PET/CT in the management of recurrent ovarian cancer," *Gynecologic Oncology*, vol. 103, no. 1, pp. 271–276, 2006.
- [54] B. K. P. Goh, "Positron emission tomography/computed tomography influences on the management of resectable pancreatic cancer and its cost-effectiveness," *Annals of Surgery*, vol. 243, no. 5, pp. 709–710, 2006.
- [55] H. Schöder, K. Herrmann, M. Gönen et al., "2-[<sup>18</sup>F]fluoro-2-deoxyglucose positron emission tomography for the detection of disease in patients with prostate-specific antigen relapse after radical prostatectomy," *Clinical Cancer Research*, vol. 11, no. 13, pp. 4761–4769, 2005.
- [56] K.-C. Ho, G. Lin, J.-J. Wang, C.-H. Lai, C.-J. Chang, and T.-C. Yen, "Correlation of apparent diffusion coefficients measured by 3T diffusion-weighted MRI and SUV from FDG PET/CT in primary cervical cancer," *European Journal of Nuclear Medicine and Molecular Imaging*, vol. 36, no. 2, pp. 200–208, 2009.
- [57] T.-C. Yen, L.-C. See, T.-C. Chang et al., "Defining the priority of using <sup>18</sup>F-FDG PET for recurrent cervical cancer," *Journal of Nuclear Medicine*, vol. 45, no. 10, pp. 1632–1639, 2004.
- [58] S. A. Schwartz, R. J. Weil, R. C. Thompson et al., "Proteomic-based prognosis of brain tumor patients using direct-tissue matrix-assisted laser desorption ionization mass spectrometry," *Cancer Research*, vol. 65, no. 17, pp. 7674–7681, 2005.
- [59] S. A. Patel, A. Barnes, N. Loftus et al., "Imaging mass spectrometry using chemical inkjet printing reveals differential protein expression in human oral squamous cell carcinoma," *The Analyst*, vol. 134, no. 2, pp. 301–307, 2009.
- [60] M. R. Groseclose, P. P. Mission, P. Chaurand, and R. M. Caprioli, "High-throughput proteomic analysis of formalin-fixed paraffin-embedded tissue microarrays using MALDI imaging mass spectrometry," *Proteomics*, vol. 8, no. 18, pp. 3715–3724, 2008.
- [61] S. Rauser, C. Marquardt, B. Balluff et al., "Classification of HER2 receptor status in breast cancer tissues by MALDI imaging mass spectrometry," *Journal of Proteome Research*, vol. 9, no. 4, pp. 1854–1863, 2010.
- [62] Y. Morita, K. Ikegami, N. Goto-Inoue et al., "Imaging mass spectrometry of gastric carcinoma in formalin-fixed paraffin-embedded tissue microarray," *Cancer Science*, vol. 101, no. 1, pp. 267–273, 2010.
- [63] M.-C. Djidja, E. Claude, M. F. Snel et al., "MALDI-ion mobility separation-mass spectrometry imaging of glucose-regulated protein 78 kDa (Grp78) in human formalin-fixed, paraffin-embedded pancreatic adenocarcinoma tissue sections," *Journal of Proteome Research*, vol. 8, no. 10, pp. 4876–4884, 2009.
- [64] S. R. Oppenheimer, D. Mi, M. E. Sanders, and R. M. Caprioli, "Molecular analysis of tumor margins by MALDI mass spectrometry in renal carcinoma," *Journal of Proteome Research*, vol. 9, no. 5, pp. 2182–2190, 2010.
- [65] R. Lemaire, S. A. Menguellet, J. Stauber et al., "Specific MALDI imaging and profiling for biomarker hunting and validation: fragment of the 11S proteasome activator complex, reg alpha fragment, is a new potential ovary cancer biomarker," *Journal of Proteome Research*, vol. 6, no. 11, pp. 4127–4134, 2007.
- [66] L. H. Cazares, D. Troyer, S. Mendrinos et al., "Imaging mass spectrometry of a specific fragment of mitogen-activated protein kinase/extracellular signal-regulated kinase kinase kinase 2 discriminates cancer from uninvolved prostate tissue," *Clinical Cancer Research*, vol. 15, no. 17, pp. 5541–5551, 2009.
- [67] J. K. Nicholson, J. C. Lindon, and E. Holmes, "Metabonomics: understanding the metabolic responses of living systems to pathophysiological stimuli via multivariate statistical analysis of biological NMR spectroscopic data," *Xenobiotica*, vol. 29, no. 11, pp. 1181–1189, 1999.
- [68] O. Fiehn, J. Kopka, P. Dörmann, T. Altmann, R. N. Trethewey, and L. Willmitzer, "Metabolite profiling for plant functional genomics," *Nature Biotechnology*, vol. 18, no. 11, pp. 1157–1161, 2000.
- [69] W. B. Dunn, D. I. Broadhurst, H. J. Atherton, R. Goodacre, and J. L. Griffin, "Systems level studies of mammalian metabolomes:

- the roles of mass spectrometry and nuclear magnetic resonance spectroscopy,” *Chemical Society Reviews*, vol. 40, no. 1, pp. 387–426, 2011.
- [70] E. M. Lenz and I. D. Wilson, “Analytical strategies in metabolomics,” *Journal of Proteome Research*, vol. 6, no. 2, pp. 443–458, 2007.
- [71] N. Psychogios, D. D. Hau, J. Peng et al., “The human serum metabolome,” *PLoS ONE*, vol. 6, no. 2, Article ID e16957, 2011.
- [72] J. R. Griffiths and Y. L. Chung, “Metabolomic studies on cancer and on anticancer drugs by NMR ex vivo,” in *Encyclopedia of Magnetic Resonance*, R. K. Harris and R. E. Wasylyshen, Eds., John Wiley & Sons, Chichester, UK, 2011.
- [73] M. V. Brown, J. E. McDunn, P. R. Gunst et al., “Cancer detection and biopsy classification using concurrent histopathological and metabolomic analysis of core biopsies,” *Genome Medicine*, vol. 4, no. 4, article 33, 2012.
- [74] K. Glunde and Z. M. Bhujwalla, “Metabolic tumor imaging using magnetic resonance spectroscopy,” *Seminars in Oncology*, vol. 38, no. 1, pp. 26–41, 2011.
- [75] C. P. Slichter, *Principles of Magnetic Resonance*, Springer, New York, NY, USA, 3rd edition, 1990.
- [76] J. Frahm, H. Bruhn, M. L. Gygell, K. D. Merboldt, W. Hanicke, and R. Sauter, “Localized high-resolution proton NMR spectroscopy using stimulated echoes: initial applications to human brain *in vivo*,” *Magnetic Resonance in Medicine*, vol. 9, no. 1, pp. 79–93, 1989.
- [77] P. A. Bottomley, “Spatial localization in NMR spectroscopy *in vivo*,” *Annals of the New York Academy of Sciences*, vol. 508, pp. 333–348, 1987.
- [78] R. J. Ordidge, R. M. Bowley, and G. McHale, “A general approach to selection of multiple cubic volume elements using the ISIS technique,” *Magnetic Resonance in Medicine*, vol. 8, no. 3, pp. 323–331, 1988.
- [79] T. R. Brown, B. M. Kincaid, and K. Ugurbil, “NMR chemical shift imaging in three dimensions,” *Proceedings of the National Academy of Sciences of the United States of America*, vol. 79, no. 11 I, pp. 3523–3526, 1982.
- [80] K. Glunde, C. Jie, and Z. M. Bhujwalla, “Molecular causes of the aberrant choline phospholipid metabolism in breast cancer,” *Cancer Research*, vol. 64, no. 12, pp. 4270–4276, 2004.
- [81] R. J. Gillies and D. L. Morse, “*In vivo* magnetic resonance spectroscopy in cancer,” *Annual Review of Biomedical Engineering*, vol. 7, pp. 287–326, 2005.
- [82] J. M. Hakumäki, H. Poptani, A.-M. Sandmair, S. Ylä-Herttuala, and R. A. Kauppinen, “<sup>1</sup>H MRS detects polyunsaturated fatty acid accumulation during gene therapy of glioma: implications for the *in vivo* detection of apoptosis,” *Nature Medicine*, vol. 5, no. 11, pp. 1323–1327, 1999.
- [83] N. M. S. Al-Saffar, J. C. Titley, D. Robertson et al., “Apoptosis is associated with triacylglycerol accumulation in Jurkat T-cells,” *British Journal of Cancer*, vol. 86, no. 6, pp. 963–970, 2002.
- [84] J. E. Schmitz, M. I. Kettunen, D.-E. Hu, and K. M. Brindle, “<sup>1</sup>H MRS-visible lipids accumulate during apoptosis of lymphoma cells *in vitro* and *in vivo*,” *Magnetic Resonance in Medicine*, vol. 54, no. 1, pp. 43–50, 2005.
- [85] J. L. Griffin, K. K. Lehtimäki, P. K. Valonen et al., “Assignment of <sup>1</sup>H nuclear magnetic resonance visible polyunsaturated fatty acids in BT4C gliomas undergoing ganciclovir-thymidine kinase gene therapy-induced programmed cell death,” *Cancer Research*, vol. 63, no. 12, pp. 3195–3201, 2003.
- [86] P. G. Okunieff, J. A. Koutcher, L. Gerweck et al., “Tumor size dependent changes in a murine fibrosarcoma: use of *in vivo* <sup>31</sup>P NMR for non-invasive evaluation of tumor metabolic status,” *International Journal of Radiation Oncology Biology Physics*, vol. 12, no. 5, pp. 793–799, 1986.
- [87] G. M. Tozer and J. R. Griffiths, “The contribution made by cell death and oxygenation to <sup>31</sup>P MRS observations of tumour energy metabolism,” *NMR in Biomedicine*, vol. 5, no. 5, pp. 279–289, 1992.
- [88] W. Wolf, C. A. Presant, and V. Waluch, “<sup>19</sup>F-MRS studies of fluorinated drugs in humans,” *Advanced Drug Delivery Reviews*, vol. 41, no. 1, pp. 55–74, 2000.
- [89] Y.-L. Chung, H. Troy, I. R. Judson et al., “Noninvasive measurements of capecitabine metabolism in bladder tumors over-expressing thymidine phosphorylase by fluorine-19 magnetic resonance spectroscopy,” *Clinical Cancer Research*, vol. 10, no. 11, pp. 3863–3870, 2004.
- [90] C. Li, M.-F. Penet, P. Winnard Jr., D. Artemov, and Z. M. Bhujwalla, “Image-guided enzyme/prodrug cancer therapy,” *Clinical Cancer Research*, vol. 14, no. 2, pp. 515–522, 2008.
- [91] E. L. Hall, M. C. Stephenson, D. Price, and P. G. Morris, “Methodology for improved detection of low concentration metabolites in MRS: optimised combination of signals from multi-element coil arrays,” *NeuroImage*, vol. 86, pp. 35–42, 2014.
- [92] J. H. Ardenkjær-Larsen, B. Fridlund, A. Gram et al., “Increase in signal-to-noise ratio of >10,000 times in liquid-state NMR,” *Proceedings of the National Academy of Sciences of the United States of America*, vol. 100, no. 18, pp. 10158–10163, 2003.
- [93] D. M. Wilson, K. R. Keshari, P. E. Z. Larson et al., “Multi-compound polarization by DNP allows simultaneous assessment of multiple enzymatic activities *in vivo*,” *Journal of Magnetic Resonance*, vol. 205, no. 1, pp. 141–147, 2010.
- [94] T. H. Witney, M. I. Kettunen, D.-E. Hu et al., “Detecting treatment response in a model of human breast adenocarcinoma using hyperpolarised [1-<sup>13</sup>C]pyruvate and [1,4-<sup>13</sup>C<sub>2</sub>]fumarate,” *British Journal of Cancer*, vol. 103, no. 9, pp. 1400–1406, 2010.
- [95] K. Golman, R. I. Zandt, M. Lerche, R. Pehrson, and J. H. Ardenkjær-Larsen, “Metabolic imaging by hyperpolarized <sup>13</sup>C magnetic resonance imaging for *in vivo* tumor diagnosis,” *Cancer Research*, vol. 66, no. 22, pp. 10855–10860, 2006.
- [96] J. Kurhanewicz, D. B. Vigneron, K. Brindle et al., “Analysis of cancer metabolism by imaging hyperpolarized nuclei: prospects for translation to clinical research,” *Neoplasia*, vol. 13, no. 2, pp. 81–97, 2011.
- [97] S. E. Day, M. I. Kettunen, F. A. Gallagher et al., “Detecting tumor response to treatment using hyperpolarized <sup>13</sup>C magnetic resonance imaging and spectroscopy,” *Nature Medicine*, vol. 13, no. 11, pp. 1382–1387, 2007.
- [98] A. P. Chen, W. Chu, Y. P. Gu, and C. H. Cunningham, “Probing early tumor response to radiation therapy using hyperpolarized [1-(1)(3)C]pyruvate in MDA-MB-231 xenografts,” *PLoS ONE*, vol. 8, no. 2, Article ID e56551, 2013.
- [99] I. Park, R. Bok, T. Ozawa et al., “Detection of early response to temozolomide treatment in brain tumors using hyperpolarized <sup>13</sup>C MR metabolic imaging,” *Journal of Magnetic Resonance Imaging*, vol. 33, no. 6, pp. 1284–1290, 2011.
- [100] C. S. Ward, H. S. Venkatesh, M. M. Chaumeil et al., “Noninvasive detection of target modulation following phosphatidylinositol 3-kinase inhibition using hyperpolarized <sup>13</sup>C magnetic resonance spectroscopy,” *Cancer Research*, vol. 70, no. 4, pp. 1296–1305, 2010.

- [101] K. Golman, L. E. Olsson, O. Axelsson, S. Måansson, M. Karlsson, and J. S. Petersson, "Molecular imaging using hyperpolarized  $^{13}\text{C}$ ," *The British Journal of Radiology*, vol. 76, no. 2, pp. S118–S127, 2003.
- [102] D. K. Hill, Y. Jamin, M. R. Orton et al., "(1)H NMR and hyperpolarized (1)(3)C NMR assays of pyruvate-lactate: a comparative study," *NMR in Biomedicine*, vol. 26, no. 10, pp. 1321–1325, 2013.
- [103] D. K. Hill, M. R. Orton, E. Mariotti et al., "Model free approach to kinetic analysis of real-time hyperpolarized  $^{13}\text{C}$  magnetic resonance spectroscopy data," *PLoS ONE*, vol. 8, no. 9, Article ID e71996, 2013.
- [104] F. A. Gallagher, M. I. Kettunen, S. E. Day et al., "Magnetic resonance imaging of pH in vivo using hyperpolarized  $^{13}\text{C}$ -labelled bicarbonate," *Nature*, vol. 453, no. 7197, pp. 940–943, 2008.
- [105] F. A. Gallagher, M. I. Kettunen, D.-E. Hu et al., "Production of hyperpolarized [1,4- $^{13}\text{C}2$ ]malate from [1,4- $^{13}\text{C}2$ ]fumarate is a marker of cell necrosis and treatment response in tumors," *Proceedings of the National Academy of Sciences of the United States of America*, vol. 106, no. 47, pp. 19801–19806, 2009.
- [106] S. J. Nelson, J. Kurhanewicz, D. B. Vigneron et al., "Metabolic imaging of patients with prostate cancer using hyperpolarized [1-(1)(3)C]pyruvate," *Science Translational Medicine*, vol. 5, no. 198, Article ID 198ra08, 2013.
- [107] V. Kapoor, B. M. McCook, and F. S. Torok, "An introduction to PET-CT imaging," *Radiographics*, vol. 24, no. 2, pp. 523–543, 2004.
- [108] M. L. Macheda, S. Rogers, and J. D. Best, "Molecular and cellular regulation of glucose transporter (GLUT) proteins in cancer," *Journal of Cellular Physiology*, vol. 202, no. 3, pp. 654–662, 2005.
- [109] S. Maschauer, O. Prante, M. Hoffmann, J. T. Deichen, and T. Kuwert, "Characterization of  $^{18}\text{F}$ -FDG uptake in human endothelial cells in vitro," *Journal of Nuclear Medicine*, vol. 45, no. 3, pp. 455–460, 2004.
- [110] K. A. Wood, P. J. Hoskin, and M. I. Saunders, "Positron emission tomography in oncology: a review," *Clinical Oncology*, vol. 19, no. 4, pp. 237–255, 2007.
- [111] C. Plathow and W. A. Weber, "Tumor cell metabolism imaging," *Journal of Nuclear Medicine*, vol. 49, supplement 2, pp. 43S–63S, 2008.
- [112] I. Grassi, C. Nanni, V. Allegri et al., "The clinical use of PET with (11)C-acetate," *American Journal of Nuclear Medicine and Molecular Imaging*, vol. 2, no. 1, pp. 33–47, 2012.
- [113] A. W. Glaudemans, R. H. Enting, M. A. Heesters et al., "Value of  $^{11}\text{C}$ -methionine PET in imaging brain tumours and metastases," *European Journal of Nuclear Medicine and Molecular Imaging*, vol. 40, no. 4, pp. 615–635, 2013.
- [114] D. Hausmann, L. K. Bittencourt, U. I. Attenberger et al., "Diagnostic accuracy of  $^{18}\text{F}$  choline PET/CT using time-of-flight reconstruction algorithm in prostate cancer patients with biochemical recurrence," *Clinical Nuclear Medicine*, 2013.
- [115] D. Soloview, D. Lewis, D. Honess, and E. Aboagye, "[ $^{18}\text{F}$ ]FLT: an imaging biomarker of tumour proliferation for assessment of tumour response to treatment," *European Journal of Cancer*, vol. 48, no. 4, pp. 416–424, 2012.
- [116] V. Paolillo, H. H. Yeh, U. Mukhopadhyay, J. G. Gelovani, and M. M. Alauddin, "Improved detection and measurement of low levels of [ $^{18}\text{F}$ ]fluoride metabolized from [ $^{18}\text{F}$ ]-labeled pyrimidine nucleoside analogues in biological samples," *Nuclear Medicine and Biology*, vol. 38, no. 8, pp. 1129–1134, 2011.
- [117] F. A. Gallagher, S. E. Bohndiek, M. I. Kettunen, D. Y. Lewis, D. Soloview, and K. M. Brindle, "Hyperpolarized  $^{13}\text{C}$  MRI and PET: in vivo tumor biochemistry," *Journal of Nuclear Medicine*, vol. 52, no. 9, pp. 1333–1336, 2011.
- [118] J. Culver, W. Akers, and S. Achilefu, "Multimodality molecular imaging with combined optical and SPECT/PET modalities," *Journal of Nuclear Medicine*, vol. 49, no. 2, pp. 169–172, 2008.
- [119] M. J. Albers, R. Bok, A. P. Chen et al., "Hyperpolarized  $^{13}\text{C}$  lactate, pyruvate, and alanine: noninvasive biomarkers for prostate cancer detection and grading," *Cancer Research*, vol. 68, no. 20, pp. 8607–8615, 2008.
- [120] C. Buchbender, T. A. Heusner, T. C. Lauenstein, A. Bockisch, and G. Antoch, "Oncologic PET/MRI, part 1: tumors of the brain, head and neck, chest, abdomen, and pelvis," *Journal of Nuclear Medicine*, vol. 53, no. 6, pp. 928–938, 2012.
- [121] S. E. Bohndiek and K. M. Brindle, "Imaging and 'omic methods for the molecular diagnosis of cancer," *Expert Review of Molecular Diagnostics*, vol. 10, no. 4, pp. 417–434, 2010.
- [122] H. F. Wehrle, J. Schwab, K. Hasenbach et al., "Multimodal elucidation of choline metabolism in a murine glioma model using magnetic resonance spectroscopy and  $^{11}\text{C}$ -choline positron emission tomography," *Cancer Research*, vol. 73, no. 5, pp. 1470–1480, 2013.
- [123] T. A. Smith, M. V. Appleyard, S. Sharp, I. N. Fleming, K. Murray, and A. M. Thompson, "Response to trastuzumab by HER2 expressing breast tumour xenografts is accompanied by decreased Hexokinase II, glut1 and [ $^{18}\text{F}$ ]-FDG incorporation and changes in 31P-NMR-detectable phosphomonoesters," *Cancer Chemotherapy and Pharmacology*, vol. 71, no. 2, pp. 473–480, 2013.
- [124] W. Wolf, "The unique potential for noninvasive imaging in modernizing drug development and in transforming therapeutics: PET/MRI/MRS," *Pharmaceutical Research*, vol. 28, no. 3, pp. 490–493, 2011.
- [125] J. F. A. Jansen, H. Schöder, N. Y. Lee et al., "Tumor metabolism and perfusion in head and neck squamous cell carcinoma: pretreatment multimodality imaging with  $^{1\text{H}}$  magnetic resonance spectroscopy, dynamic contrast-enhanced MRI, and [ $^{18}\text{F}$ ]FDG-PET," *International Journal of Radiation Oncology Biology Physics*, vol. 82, no. 1, pp. 299–307, 2012.
- [126] C. Testa, R. Schiavina, R. Lodi et al., "Prostate cancer: sextant localization with MR imaging, MR spectroscopy, and  $^{11}\text{C}$ -choline PET/CT," *Radiology*, vol. 244, no. 3, pp. 797–806, 2007.
- [127] V. Panebianco, A. Sciarra, D. Lisi et al., "Prostate cancer:  $^{1\text{H}}$ MRS-DCEMR at 3 T versus [( $^{18}\text{F}$ )choline PET/CT in the detection of local prostate cancer recurrence in men with biochemical progression after radical retropubic prostatectomy (RRP)," *European Journal of Radiology*, vol. 81, no. 4, pp. 700–708, 2012.
- [128] M. Tozaki and K. Hoshi, " $^1\text{H}$  MR spectroscopy of invasive ductal carcinoma: correlations with FDG PET and histologic prognostic factors," *American Journal of Roentgenology*, vol. 194, no. 5, pp. 1384–1390, 2010.
- [129] R. Katz-Bruell, P. T. Lavin, and R. E. Lenkinski, "Clinical utility of proton magnetic resonance spectroscopy in characterizing breast lesions," *Journal of the National Cancer Institute*, vol. 94, no. 16, pp. 1197–1203, 2002.
- [130] A. Kumiko, I. Reiichi, N. Yuki et al., "Usefulness of Cho/Cr ratio in proton MR spectroscopy for differentiating residual/recurrent glioma from non-neoplastic lesions," *Nippon Acta Radiologica*, vol. 64, no. 3, pp. 121–126, 2004.

- [131] R. Hourani, L. J. Brant, T. Rizk, J. D. Weingart, P. B. Barker, and A. Horská, "Can proton MR spectroscopic and perfusion imaging differentiate between neoplastic and nonneoplastic brain lesions in adults?" *American Journal of Neuroradiology*, vol. 29, no. 2, pp. 366–372, 2008.
- [132] E. A. Smith, R. C. Carlos, L. R. Junck, C. I. Tsien, A. Elias, and P. C. Sundgren, "Developing a clinical decision model: MR spectroscopy to differentiate between recurrent tumor and radiation change in patients with new contrast-enhancing lesions," *American Journal of Roentgenology*, vol. 192, no. 2, pp. W45–W52, 2009.
- [133] S. A. Sung, M.-J. Kim, S. L. Joon, H.-S. Hong, E. C. Yong, and J.-Y. Choi, "Added value of gadoxetic acid-enhanced hepatobiliary phase MR imaging in the diagnosis of hepatocellular carcinoma," *Radiology*, vol. 255, no. 2, pp. 459–466, 2010.
- [134] J. Hwang, S. H. Kim, M. W. Lee, and J. Y. Lee, "Small, ( $\leq 2$  cm) hepatocellular carcinoma in patients with chronic liver disease: comparison of gadoxetic acid-enhanced 3.0 T MRI and multiphasic 64-multirow detector CT," *The British Journal of Radiology*, vol. 85, no. 1015, pp. e314–e322, 2012.
- [135] M. J. Park, Y. K. Kim, M. W. Lee et al., "Small hepatocellular carcinomas: improved sensitivity by combining gadoxetic acid-enhanced and diffusion-weighted MR imaging patterns," *Radiology*, vol. 264, no. 3, pp. 761–770, 2012.
- [136] J.-W. Park, H. K. Ji, K. K. Seok et al., "A prospective evaluation of  $^{18}\text{F}$ -FDG and  $^{11}\text{C}$ -acetate PET/CT for detection of primary and metastatic hepatocellular carcinoma," *Journal of Nuclear Medicine*, vol. 49, no. 12, pp. 1912–1921, 2008.
- [137] J.-N. Talbot, L. Fartoux, S. Balogova et al., "Detection of hepatocellular carcinoma with PET/CT: a prospective comparison of  $^{18}\text{F}$ -fluorocholine and  $^{18}\text{F}$ -FDG in patients with cirrhosis or chronic liver disease," *Journal of Nuclear Medicine*, vol. 51, no. 11, pp. 1699–1706, 2010.
- [138] M. I. Menzel, E. V. Farrell, M. A. Janich et al., "Multimodal assessment of in vivo metabolism with hyperpolarized [ $^{1-13}\text{C}$ ]MR spectroscopy and  $^{18}\text{F}$ -FDG PET imaging in hepatocellular carcinoma tumor-bearing rats," *Journal of Nuclear Medicine*, vol. 54, no. 7, pp. 1113–1119, 2013.
- [139] R. Srirajaskanthan, I. Kayani, A. M. Quigley, J. Soh, M. E. Caplin, and J. Bomanji, "The role of  $^{68}\text{Ga}$ -DOTATATE PET in patients with neuroendocrine tumors and negative or equivocal findings on  $^{111}\text{In}$ -DTPA-octreotide scintigraphy," *Journal of Nuclear Medicine*, vol. 51, no. 6, pp. 875–882, 2010.
- [140] M. Ljungberg, G. Westberg, B. Vikhoff-Baaz et al., "31P MR spectroscopy to evaluate the efficacy of hepatic artery embolization in the treatment of neuroendocrine liver metastases," *Acta Radiologica*, vol. 53, no. 10, pp. 1118–1126, 2012.
- [141] F. Sullentrop, J. Hahn, and D. Moka, "In vitro and in vivo ( $^1\text{H}$ )-MR spectroscopic examination of the renal cell carcinoma," *International Journal of Biomedical Science*, vol. 8, no. 2, pp. 94–108, 2012.
- [142] K. R. Keshari, R. Sriram, B. L. Koelsch et al., "Hyperpolarized  $^{13}\text{C}$ -pyruvate magnetic resonance reveals rapid lactate export in metastatic renal cell carcinomas," *Cancer Research*, vol. 73, no. 2, pp. 529–538, 2013.
- [143] D. S. Cornett, J. A. Mobley, E. C. Dias et al., "A novel histology-directed strategy for MALDI-MS tissue profiling that improves throughput and cellular specificity in human breast cancer," *Molecular and Cellular Proteomics*, vol. 5, no. 10, pp. 1975–1983, 2006.
- [144] S. Nimesh, S. Mohottalage, R. Vincent, and P. Kumarathasan, "Current status and future perspectives of mass spectrometry imaging," *International Journal of Molecular Sciences*, vol. 14, no. 6, pp. 11277–11301, 2013.
- [145] D. Miura, Y. Fujimura, and H. Wariishi, "In situ metabolomic mass spectrometry imaging: recent advances and difficulties," *Journal of Proteomics*, vol. 75, no. 16, pp. 5052–5060, 2012.
- [146] A. C. Crecelius, D. S. Cornett, R. M. Caprioli, B. Williams, B. M. Dawant, and B. Bodenheimer, "Three-dimensional visualization of protein expression in mouse brain structures using imaging mass spectrometry," *Journal of the American Society for Mass Spectrometry*, vol. 16, no. 7, pp. 1093–1099, 2005.
- [147] T. Harada, A. Yuba-Kubo, Y. Sugiura et al., "Visualization of volatile substances in different organelles with an atmospheric-pressure mass microscope," *Analytical Chemistry*, vol. 81, no. 21, pp. 9153–9157, 2009.
- [148] G. Sun, K. Yang, Z. Zhao, S. Guan, X. Han, and R. W. Gross, "Matrix-assisted laser desorption/ionization time-of-flight mass spectrometric analysis of cellular glycerophospholipids enabled by multiplexed solvent dependent analyte-matrix interactions," *Analytical Chemistry*, vol. 80, no. 19, pp. 7576–7585, 2008.
- [149] K. Chughtai, L. Jiang, T. R. Greenwood, K. Glunde, and R. M. Heeren, "Mass spectrometry images acylcarnitines, phosphatidylcholines, and sphingomyelin in MDA-MB-231 breast tumor models," *Journal of Lipid Research*, vol. 54, no. 2, pp. 333–344, 2013.
- [150] D. Miura, Y. Fujimura, M. Yamato et al., "Ultrahighly sensitive in situ metabolomic imaging for visualizing spatiotemporal metabolic behaviors," *Analytical Chemistry*, vol. 82, no. 23, pp. 9789–9796, 2010.
- [151] K. Hattori, M. Kajimura, T. Hishiki et al., "Paradoxical ATP elevation in ischemic penumbra revealed by quantitative imaging mass spectrometry," *Antioxidants and Redox Signaling*, vol. 13, no. 8, pp. 1157–1167, 2010.
- [152] R. Calavia, F. E. Annanouch, X. Correig, and O. Yanes, "Nanostucture Initiator Mass Spectrometry for tissue imaging in metabolomics: future prospects and perspectives," *Journal of Proteomics*, vol. 75, no. 16, pp. 5061–5068, 2012.
- [153] T. R. Northen, O. Yanes, M. T. Northen et al., "Clathrate nanostructures for mass spectrometry," *Nature*, vol. 449, no. 7165, pp. 1033–1036, 2007.